Title

Fault Zone Heterogeneity and Frictional Strength Variability During the Earthquake Cycle Along the Nicoya Peninsula Megathrust, Costa Rica

Author

Chaves, Esteban Josue

Publication Date

2018

UNIVERSITY OF CALIFORNIA
SANTA CRUZ

FAULT ZONE HETEROGENEITY AND FRICTIONAL STRENGTH VARIABILITY DURING THE EARTHQUAKE CYCLE ALONG THE NICOYA PENINSULA MEGATHRUST, COSTA RICA

A dissertation submitted in partial satisfaction
of the requirements for the degree of

DOCTOR OF PHILOSOPHY

In

EARTH SCIENCES

by

Esteban J. Chaves

September 2018

The dissertation of Esteban J. Chaves
is approved:

Professor Susan Y. Schwartz, chair

Professor Thorne Lay

Professor Emily Brodsky

Lori Kletzer
Vice Provost and Dean of Graduate Studies

TABLE OF CONTENTS

LIST OF FIGURES

LIST OF TABLES

ABSTRACT

Fault zone heterogeneity and frictional strength variability during the earthquake cycle along the Nicoya peninsula megathrust, Costa Rica

Esteban J. Chaves

Earthquake stress drop, strong ground shaking, recurrence interval and the rupture characteristics of large and great earthquakes are controlled by fault strength and the frictional properties of the plate interface. Monitoring the fault strength and its variability during the earthquake cycle is critical for earthquake hazard assessment. Subduction zones in particular, generate the largest and potentially more catastrophic earthquakes around the world. The rapid convergence (85-90 mm/yr) of the Cocos plate underneath the Caribbean plate along the Nicoya Peninsula, the northwestern margin of the Costa Rica subduction zone has generated M7+ earthquakes every 50 years (1853, 1900, 1950), with the last one of these events, a moment magnitude (Mw) 7.6 earthquake, occurring on 5 September 2012. Because of the advantageous location of the Nicoya Peninsula, extending seaward, over the seismogenic zone, a very dense seismic and geodetic network has recorded with incredible detail the megathrust activity throughout the last decade. Geodetic observations prior to the occurrence of the M7.6, 2012 earthquake, identified regions of strain accumulation that delineated the rupture area of this event. Regions of the plate interface up-dip and down-dip of

this patch accommodate relative plate motions aseismically, hosting numerous Slow Slip events (SSEs) that have been well recorded since 2007, suggesting a partition of the plate interface into regions of frictionally stable and unstable or conditionally stable sliding behavior. This dissertation focuses on the study of fault zone heterogeneity and the frictional strength variability along the plate interface and upper plate of the Nicoya Peninsula subduction zone margin and its plausible relationship with the previously documented seismic and aseismic frictional slip behaviors.

The use of long-term cross-correlation of ambient seismic noise has become widely adopted at several seismological observatories for a) studying the susceptibility to crustal velocity variations along volcanic areas and the Earth's subsurface due to transient events like volcanic eruptions, shallow earthquakes, landslides, etc., and b) seismic imaging. The use of random wave fields (coda waves or ambient seismic noise) for seismic imaging has proved to overcome certain limitations so far presented by the traditional tomography methods. This dissertation extends the use of the long-term cross-correlation of ambient noise vibrations to monitor variations in elastic properties and fault heterogeneity located along the overriding plate; before, during and after the 5 September, 2012 M7.6, Nicoya Peninsula megathrust earthquake. This large event was followed by thousands of aftershocks spatially localized in four clusters distributed along strike, as well as some geodetically detected post-seismic slip.

Earthquake focal mechanisms for nearly 300 of the Nicoya earthquake aftershocks were estimated using regional full waveform moment tensor inversions and P wave first motion polarities. The finite fault model of this large event generated by Liu *et al*., [2015] was used to compute the Coulomb static stress change imposed by the main shock on the nodal planes of the aftershock sequence in order to make a first evaluation of the static versus dynamic earthquake triggering hypotheses.

In addition, a total of 5 repeating earthquake families, earthquakes with nearly identical waveforms and thought to represent the rupture of the same fault asperity at a relatively constant repeat interval due to continuous loading by surrounding aseismic slip, were recognized using waveform matching techniques from 2007 through 2016. These earthquake families locate along the up-dip margin of the fault that ruptured during 5 September 2012, Mw 7.6 Nicoya megathrust. Due to the repeating nature of these events they do sense the temporal changes in the physical properties of the medium, including variations in the frictional strength of the plate interface. This dissertation extends the use of repeating earthquakes to derive stress drop or fault yield strength before and after the occurrence of the Nicoya peninsula earthquake.

ACKNOWLEDGEMENTS

The text of this dissertation includes reprints of the following previously published material. The co-authors listed in these publications directed and supervised the research which forms the basis for the dissertation.

Chapter 1: Chaves. J. E. and S. Y. Schwartz (2016) Monitoring transient changes within overpressured regions of subduction zones using ambient seismic noise. *Sci. Adv., 2*. doi: 10.1126/sciadv.1501289.

Chapter 2: Chaves, E., Duboeuf, L., Schwartz, S., Lay, T. and Kintner, J. Aftershocks of the 2012 Mw 7.6 Nicoya, Costa Rica, Earthquake and Mechanics of the Plate Interface Aftershocks of the 2012 Mw 7.6 Nicoya, Costa Rica, Earthquake and Mechanics of the Plate Interface. Bulletin of the Seismological Society of America **107,** 1227–1239 (2017).

I would like to acknowledge the support and assistance from numerous people and organizations, without whom this PhD dissertation would not have been possible. Getting a PhD is a whole endeavor that not only prepares us as scientists. It does make of us a better person; more dedicated, sensible, analytical and independent. As a foreign student, the experiences I was part of during the last five years are invaluable, among them, I had the opportunity to be part of one of the best seismology schools in the U.S. and meet very interesting and brilliant scientists. I am an Antarctic expeditioner and have been traveling the world sharing my own research. This all would not be possible without the incredible support and guidance of my academic advisor: Dr. Susan Schwartz. Thank you very much Susan, for being the incredible person you are and for giving me the opportunity to be your student, I am really honored. Without your encouragement and advice I would not have achieved all the great work and high profile scientific research that we have done. Thank you for your support and understanding when I was going through difficult situations in life.

I would also like to thank my committee members Dr. Thorne Lay and Dr. Emily Brodsky for their guidance and patience during the course of my PhD. I am very thankful with Thorne Lay for introducing me to the fascinating world of “forensic seismology and nuclear explosions”.

Many thanks to my fellow students and postdocs in the seismology lab and to the E&PS department office staff for all their encouragement and support over the years. A very special thank you to Ed Boring, the best IT manager on planet Earth, for being such a nice person and for all the meaningful conversations we had about Python programming.

This dissertation would not be possible without the support from the next institutions:

- Volcanological and Seismological Observatory of Costa Rica (OVSICORI).
- Universidad Nacional de Costa Rica (UNA)
- Ministerio de Ciencia, Tecnología y Telecomunicaciones de Costa Rica (MICITT).
- Consejo Nacional para Investigaciones Científicas y Tecnológicas de Costa Rica (CONICIT).
- UNAVCO and the COCOnet Project.

Finally, I would like to extend a very special thank you to my friends Marino Protti, Javier Pacheco and Victor Gonzales from OVSICORI-UNA for encouraging me to pursue graduate school. Thank you all for the long conversations about seismology, current and future projects in Costa Rica, and for sharing with me your personal experiences during graduate school.

CHAPTER 1- MONITORING TRANSIENT CHANGES WITHIN OVERPRESSURED REGIONS OF SUBDUCTION ZONES USING AMBIENT SEISMIC NOISE

Abstract. In subduction zones, elevated pore fluid pressure, generally linked to metamorphic dehydration reactions, has a profound influence on the mechanical behavior of the plate interface and forearc crust through its control on effective stress. We use seismic noise–based monitoring to characterize seismic velocity variations following the 2012 Nicoya Peninsula, Costa Rica earthquake [Mw (moment magnitude) 7.6] that we attribute to the presence of pressurized pore fluids. Our study reveals a strong velocity reduction (~0.6%) in a region where previous work identified high forearc pore fluid pressure. The depth of this velocity reduction is constrained to be below 5 km and therefore not the result of near-surface damage due to strong ground motions; rather, we posit that it is caused by fracturing of the fluid-pressurized weakened crust due to dynamic stresses. Although pressurized fluids have been implicated in causing coseismic velocity reductions beneath the Japanese volcanic arc, this is the first report of a similar phenomenon in a subduction zone setting. It demonstrates the potential to identify pressurized fluids in subduction zones using temporal variations of seismic velocity inferred from ambient seismic noise correlations.

1.1 INTRODUCTION

With the development of large seismic networks, a constantly increasing amount of data open up new opportunities for seismologist to study both the physics of earthquake sources and the Earth's structure itself. For instance, advancements in seismic tomography have provided the opportunity to image with great detail the structures through which elastic seismic waves travel. However, the success of traditional tomography depends, among other factors, upon high quality seismic catalogs, which are not always available or present certain limitations. Earthquake catalogs may be subject to bias due to misreading or time-picking procedure errors of the body wave arrivals, and errors in travel time measurements may eventually contaminate seismic images. Moreover, earthquakes are transient events, their distribution is not spatially homogeneous and in the absence of a good azimuthal instrumental coverage, seismicity might be poorly distributed in space and time.

The problem of imaging in strongly diffractive media is also a challenge for other research areas, like acoustics, optics and mesoscopic physics. Recent laboratory experiments with ultrasonic and thermal noise have demonstrated that it is possible to study the mechanical or elastic properties of the medium retrieving coherent signals (Green's functions) from the correlation of diffusive wave fields. Similarly, seismologists have recognized that coda waves (composed predominantly of surface waves) are the result of scattering from small-scale heterogeneities in the lithosphere and so, they do contain the information about the current status of the elastic properties (e.g. seismic velocities) of the medium. The extraction of deterministic information of the Earth’s crust using the correlation of the long-term diffusive seismic wave field (coda waves or ambient seismic noise) has proved to overcome the limitations presented in traditional seismic tomography methods, extending its use beyond imaging to real time monitoring of transient natural processes (volcanic eruptions, crustal earthquakes, landslides, etc.) and industry-related activities (explosions, fluid injection or extraction in oil and geothermal fields).

Processes accompanying earthquakes can produce changes in the mechanical properties and therefore seismic velocities of the surrounding crustal material. Dynamic and static stress changes, fluid migration, fault zone damage and healing, and nonlinear response of near surface material to strong ground motion have all been implicated in causing changes to measured seismic velocities following earthquakes (Peng et al., 2006; Cheng and Wang, 2010; Nakata and Snider, 2011). These time dependent velocity changes have been detected from measurement of time lags within repeating earthquake sequences (Poupinet *et al.*, 1984) or from cross correlation of continuous ambient seismic noise recordings (Zacarelli *et al.*, 2011). While temporal variations in seismic velocity accompanying earthquakes have revealed information about the mechanical behavior of the shallow surface and near fault zone environment, susceptibility of a region to co-seismic velocity change has recently been used to characterize crustal rheology farther from the earthquake source. In particular, ambient noise cross-correlations showed that the strongest velocity reductions associated with the 2011 Tohoku earthquake occurred under the volcanic arc, rather than in the epicentral region (Brenguier *et al*., 2014).

The velocity reduction was attributed to dynamic stress associated with seismic waves fracturing fluid pressurized weakened crust. We use a similar method to document seismic velocity reductions in the forearc crust of the Nicoya Peninsula following the 2012, Mw 7.6, underthrusting earthquake. Correspondingly, we ascribe this to an increase in fracture density in high pore fluid pressure weakened crust due to dynamic stresses. Our observations extend the use of seismic velocity change susceptibility to identify pressurized fluids to subduction zones. The presence of such fluids is important in controlling plate boundary behavior and magma genesis; however, their distribution is poorly constrained by existing methods.

1.2 TECTONIC SETTING

Costa Rica is part of the Central American volcanic front formed by subduction of the oceanic Cocos plate beneath the continental Caribbean plate along the Middle American Trench (MAT) at a rate of ~85-90 mm/yr (DeMets *et al*., 2010). This rapid convergence rate has generated magnitude 7+ earthquakes in 1853, 1900, 1950 and 2012 along the Nicoya Peninsula, the northwestern margin of the Costa Rica subduction zone. Due to the advantageous location of the Nicoya Peninsula, extending seaward over the seismogenic zone, regional broadband seismic and continuous GPS stations provide unusually good coverage of megathrust activity since the last decade (Figure. 1.1). Several studies have shown that the seismogenic zone below the Nicoya Peninsula is characterized by strong lateral variations in thermal structure, composition, pore fluids and earthquake behavior due to differences in the genesis of the subducting lithosphere; while the northwestern part was generated at the East Pacific Rise (EPR), the southeastern crust was formed at the Cocos-Nazca spreading center (CNS). The position of the boundary EPR-CNS is well defined by magnetic anomalies and high resolution bathymetry data (Barckhausen *et al*., 2001). It extends ~80 km from the morphological rough-smooth boundary in the older part of the Cocos plate until its orthogonal convergence with the MAT off the central part of the Peninsula (Figure. 1.1).

Besides hosting large earthquakes every 50 years, seismic tremor activity and slow-slip events (SSEs) have been observed every ~ 2 years or less at transitions between seismic and aseismic slip areas. Geodetic observations prior to the occurrence of the M7.6, 2012 earthquake, identified regions of strain accumulation that delineated the rupture area of this event. Regions of the plate interface up-dip and down-dip of this patch accommodate relative plate motions aseismically, hosting much of the SSEs that have been well recorded since 2007, suggesting a partition of the plate interface into regions of frictionally stable and unstable or conditionally stable sliding behavior. Due to the particular conditions of the subduction zone along the Nicoya Peninsula: regular intermediate and large magnitude earthquakes, accessibility and an increasing amount of seismic and geodetic data, studying this particular area provides a great opportunity to better characterize the seismic cycle and thus, improve seismic hazard assessments, building codes and policies.

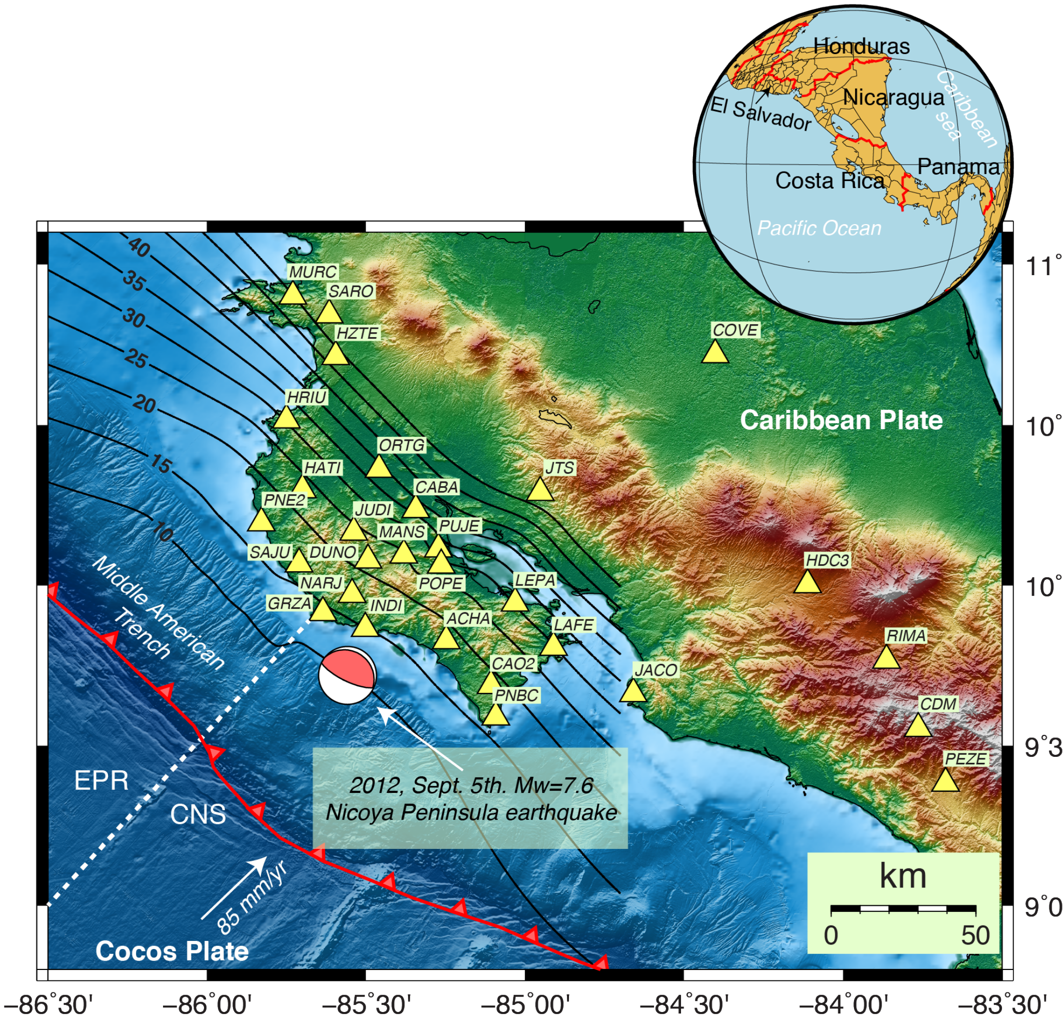

Figure 1.1 Tectonic setting and the Nicoya Seismic Cycle Observatory. The map shows the spatial distribution of the Nicoya Seismic Cycle Observatory and OVSICORI-UNA seismic stations used in this study. Contour lines (Deshon *et al.*, 2006) indicate the depth to the top of the subducted slab. The dotted line represents the East Pacific Rise (EPR)-Cocos Nazca Spreading center (CNS) boundary (Barckhausen et al., 2001). The location and focal mechanism of the 2012, M_W =7.6 Nicoya Peninsula earthquake are also indicated.

1.3. METHODS

1.3.1 CROSS-CORRELATION OF AMBIENT SEISMIC NOISE

Crustal seismic velocity variations can be measured by the long-term (e.g. months or years of data) cross-correlation of ambient seismic noise. A growing number of theoretical and experimental efforts have shown that the coherence of diffuse wave fields (e.g. coda waves or ambient seismic noise) can be used to retrieve direct seismic waves (Green's functions, GFs) between two points on the Earth's surface. This reconstruction is related to the principles of equipartition and time reversal, and therefore, directly linked to the mechanical properties of the medium.

1.3.2. RECONSTRUCTION OF GREEN'S FUNCTIONS FROM THE CROSS-CORRELATION OF CODA WAVES

Consider two receivers that are separated a distance R, as shown in figure 1.2. The receivers are placed in a medium where the propagation velocity c, is assumed to be constant and the scatters (or discontinuities) S radiate scalar waves $S_s(t)$. The wave field at the receivers can be written as a superposition of the waves radiated by the scatters:

$$p_{1,2} = \sum_{s} S(t - {}^{r_{1,2}}/_{c})/r_{1,2} \qquad (1.1)$$

In passive seismology, the correlation of the seismic waves recorded at the receivers over a time window of length T is given by:

$$C(\tau) = \int_0^T p_2(t+\tau)p_1(t)dt \tag{1.2}$$

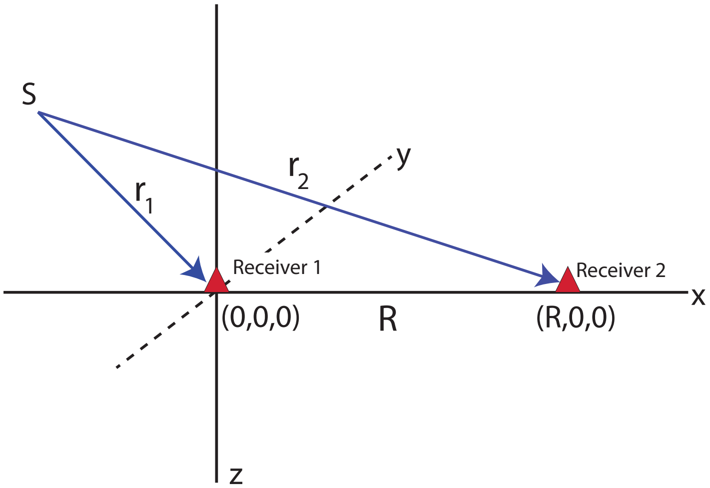

Figure 1.2. Definition of geometric variables for scatter waves

Inserting equation (1.1) into equation (1.2) gives a double sum over all scatters:

$$C(\tau) = \sum_{s,s'} \int_0^T S_s(t)S_{s'}(t + \frac{r_1 - r_2}{c} + \tau)\ dt/r_1r_2 \tag{1.3}$$

Let the autocorrelation of the signal $S_s(t)$ be denoted by:

$$C_s(\tau) = \int_0^T S_s(t)S_s\,(t+\tau)\ dt \tag{1.4}$$

The double sum in equation (1.3) can be split into a sum over diagonal terms $\sum_{s=s'}$ ... and a sum over cross terms $\sum_{s\neq s'}$ ... in a random, isotropic medium, and assuming the long-term cross-correlation of ambient seismic noise, the cross terms can be neglected, physically they represent destructive interference of waves emitted from scatters located away from the receiver lines. Ignoring the cross terms and combining (1.3) and (1.4):

$$C(\tau) = \sum\nolimits_{s} C_s\left(\frac{r_1 - r_2}{c} + \tau\right)/r_1 r_2 \tag{1.5}$$

Applying a Fourier transform to equation (1.5):

$$C(\omega) = \sum_{s} |S(\omega)|^2 \, \frac{e^{iw(r_2 - r_2)/c}}{r_1 r_2} \tag{1.6}$$

When variations in power spectrum are uncorrelated with the phase:

$$C(\omega) = \frac{1}{N}\sum_{s} |S(\omega)|^2 \sum_{s} \frac{e^{i\omega(r_1 - r_2)/c}}{r_1 r_2} \tag{1.7}$$

If there are many scatters per wavelength the sum over scatters can be replaced by a volume integral with *n* defined as the number of scatters per unit volume:

$$C(\omega) = \frac{1}{N}\sum_{s} |S(\omega)|^2 \int \frac{e^{i\omega(r_1 - r_2)/c}}{r_1 r_2} \, n \, dxdydz \tag{1.8}$$

Assuming a stationary phase approximation $y = z = 0$, and assuming the only contribution comes from the receiver line (constructive interference):

$$C(\omega) = \frac{8\pi^2}{N}\sum_{s} |S(\omega)|^2 \left(\frac{c}{i\omega}\right)\left[\left(\frac{-e^{ikR}}{4\pi R}\right)\int_{-\infty}^{0} n \, dx - \left(\frac{e^{-ikR}}{4\pi R}\right)\int_{R}^{\infty} n \, dx\right] \tag{1.9}$$

In the above equation, the term $\left(\frac{-e^{ikR}}{4\pi R}\right)$ corresponds with the Green's function that accounts for the waves that travel between the receivers; in other words, the causal Green's function that propagates from receiver 1 to receiver 2, and the second term $\left(\frac{e^{-ikR}}{4\pi R}\right)$ is the acausal Green's function that propagates from receiver 2 to receiver 1 (Figures. 1.3 and 1.4).

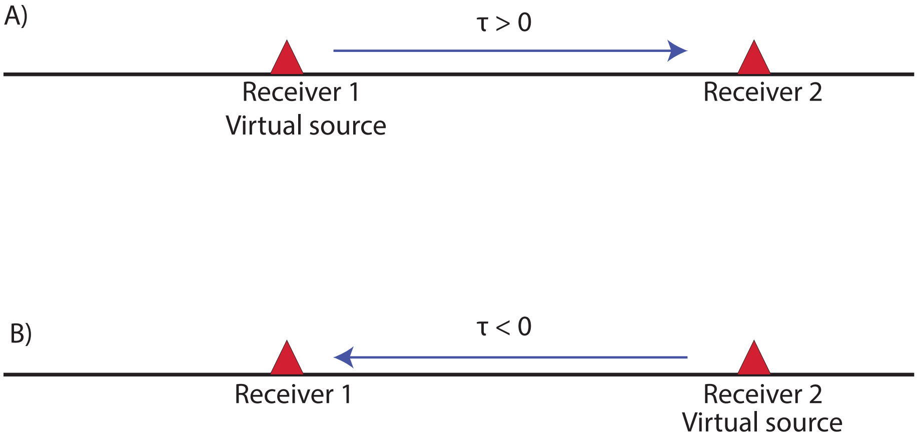

Figure 1.3. Causal and acausal Green's functions. Waves propagating between receivers. A) Causal Green's functions. B) Acausal Green's function.

1.3.3. APPLICATION TO THE NICOYA SEISMIC CYCLE OBSERVATORY (NSCO)

Here, we use the cross-correlation of ambient seismic noise (e.g Shapiro and Campillo, 2004; Campillo, 2006) (diffuse wave field composed of surface waves) to characterize crustal seismic velocity variations following the 5 September 2012 Nicoya Peninsula earthquake. We analyzed two years of continuous seismic records, between April 2012-April 2014, using all stations of a local broadband network that contained no significant data gaps during this period. We used MSNoise (www.msnoise.org) (Lecocq *et al.*, 2014) to compute daily vertical cross-correlation functions, or GFs (seismic response of the Earth's crust if an impulse is applied to each station) between all station pairs.

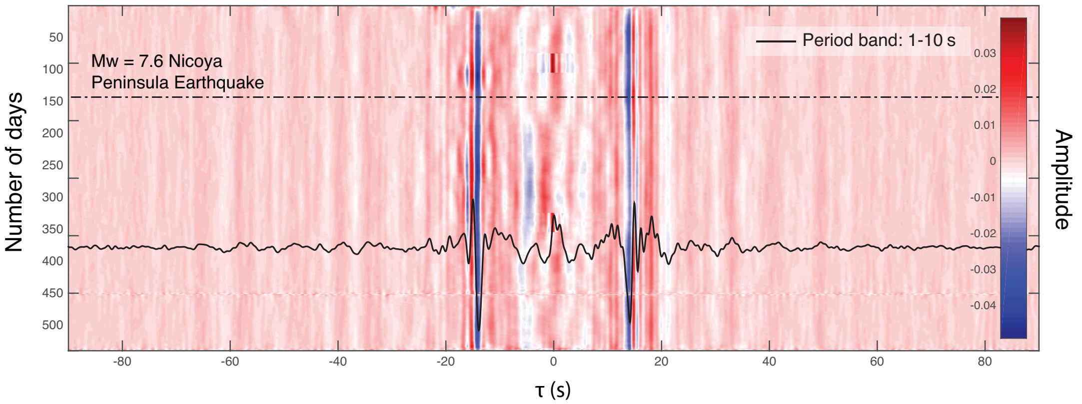

Figure 1.4. Cross correlation of ambient seismic noise. Daily GFs filtered between 1-10 s for the station pair INDI-SAJU. The black trace represents the reference Green's function (RGF). The dotted line indicates the time of the Nicoya Peninsula earthquake. Note the high symmetry between the causal and acausal signals.

The daily seismic records were demeaned, tapered and corrected for their instrument response. We applied a band pass filter of 8 to 0.01 Hz and down sampled from 100 Hz to 20 Hz as a pre-processing stage. In order to reduce the effects of earthquake signals, we applied one-bit normalization and spectral whitening in the period ranges of our analysis: 1-10 s, 1-3 s, 3-10 s, 5-10 s. The spectral normalization acts to enhance the band of ambient noise signal in the cross-correlations and reduce possible degradation caused by persistent monochromatic sources.

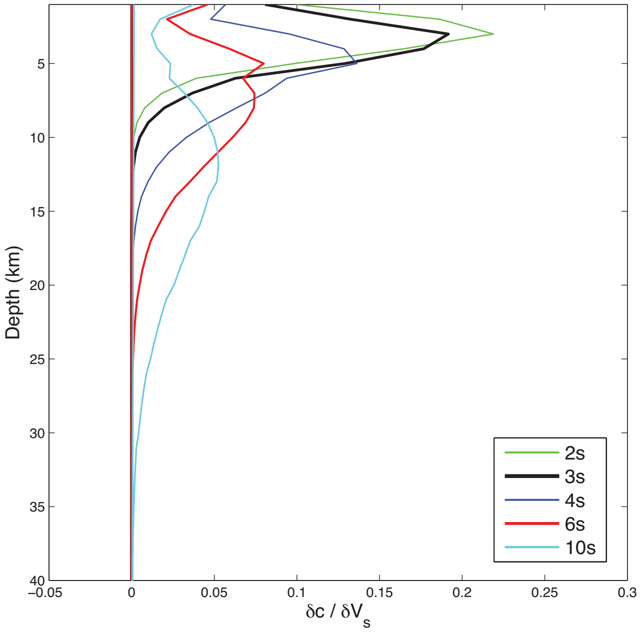

Figure 1.5. Rayleigh wave velocity sensitivity kernels.

We calculated daily cross-correlation functions for the ten station pairs in the period ranges listed above to retrieve Rayleigh waves. For these period ranges and a local 1-D velocity model (DeShon *et al.*, 2006), Rayleigh waves are sensitive to velocity variations occurring from the uppermost crust to 15 km depth (Figure. 1.5). We defined a reference Green's function (RGF) by stacking all daily GFs from before the earthquake to ensure that the RGF is representative of a background pre-main shock value while the daily GFs contain the information on the current state of the Earth's crust. To avoid mixing of pre-seismic and post-seismic signals, we removed the days containing the main shock and the largest aftershocks.

1.3.4. Crustal seismic velocity variations

To estimate the crustal velocity changes between all station pairs, we adopted the Moving Window Cross Spectral Analysis (MWCS) method (Clarke *et al.*, 2011). This method computes the time delay (∂t) between the RGF and 30-day GF stacks from the phase of their cross-spectrum. Our application of the MWCS uses a moving time window of 10 s with an overlap of 80 %. The 30-day GF stack window length was used in order to reduce the uncertainty of our seismic velocity measurements for the individual station pairs. To ensure that our measurements are independent of variations in noise sources, we measured travel time delays within the coda of the GFs, which are primarily composed of surfaces waves. Assuming an isotropic medium, propagation time varies proportionally to distance between station pairs, and the phase shift between the records varies linearly with time. Accordingly, the relative crustal velocity change

∂v can be measured from the slope of the time delay ∂t as a function of lag time: $\partial t/t = -\partial v/v$.

1.4 RESULTS AND DISCUSSION

Symmetric Green’s functions with little amplitude variation as a function of time (indicating relatively stationary noise sources with little seasonal variation) were obtained for most station pairs (Figure. 1.4). These were used to compute crustal velocity changes by measuring the time delay between the coda of the RGF and the 30 day stacks of the daily GFs. The GFs and their coda are composed of surface waves with sensitivity to velocity that depends on period (short periods are sensitive to shallow crustal structure and longer periods are sensitive to deeper structure) (Figure. 1.5). In order to differentiate velocity changes as a function of depth, we calculated time shifts relative to the corresponding RGF using different period bands: 1-10 s, 1-3 s, 3-10 s, and 5-10s.

Our results reveal frequency dependent coseismic velocity reductions that vary spatially. Analysis in the shortest period band (1-3 s) indicates that the largest velocity reductions of 0.4% occur between station pairs that lie adjacent to the area of maximum slip associated with the 2012 Nicoya earthquake (Figure. 1.6A). In this period range, the velocity reductions are constrained to the upper 5 km of the crust (Figure. 1.5). The precise timing of the velocity reduction onset is not well resolved due to the use of 30-day GF stacks to stabilize measurements of time shifts relative to the RGF for individual station pairs (Figure. 1.7A). However, the progressively earlier onset times obtained when using GF stacks of fewer days indicates that the velocity reduction occurs very shortly after the earthquake.

Based on the timing, location and shallow depth of the velocity reductions, we attribute them to near surface damage produced by strong ground shaking accompanying the 2012 Nicoya earthquake. Static stress changes following the earthquake are also a possible source of the coseismic velocity reduction. Dilatational volumetric strain changes are predicted at shallow depth in the region of the velocity reduction (Figure. A-1).

Dilatational strain would favor the opening of fractures and the reduction of seismic velocity following the earthquake. Our results indicate that less than 50% of this co-seismic velocity reduction was recovered a year after the main shock (Fig. 1.7A). Several studies using ambient noise-based monitoring have reported reductions in seismic velocities following large earthquakes (Brenguier *et al.*, 2008; Liu *et al.*, 2014); most of these reductions were relatively small (<0.4%), located at shallow depth (upper 2 km of the crust), and correlated with peak co-seismic slip and/or peak ground velocity. Nonlinear response of near surface material to strong ground motion was implicated in most of these studies. A similar magnitude and timing of velocity recovery to our results was obtained following many of these other earthquakes (Hobiger *et al.*, 2012).

Figure 1.6. Map of northern Costa Rica showing seismic velocity reductions following the Mw 7.6, 2012, Nicoya Peninsula, Costa Rica earthquake. The white dashed line marks the position where the origin of the subducting oceanic lithosphere changes from warmer Cocos Nazca Spreading center (CNS) to colder East Pacific Rise (EPR) (Barckhausen *et al*., 2001). **(A)** The focal mechanism (~21 km centroid depth) and area of concentrated slip for the main shock (dashed black contour (Yue *et al*., 2013)) are indicated. Black inverted triangles correspond to the broadband seismic stations used in this study. Triangles show the location of strong ground motion sensors from the Universidad de Costa Rica with their color indicating peak ground velocity (PGV). Colored lines indicate co-seismic velocity reductions obtained in the period band 1-3 s along the interstation path. **(B)** Colored lines indicate seismic velocity reductions obtained in the period band 3-10 s. Inverted triangles indicate the Vp/Vs values obtained for the forearc crust from receiver function analysis (Audet and Schwartz, 2013). Note there were no relative

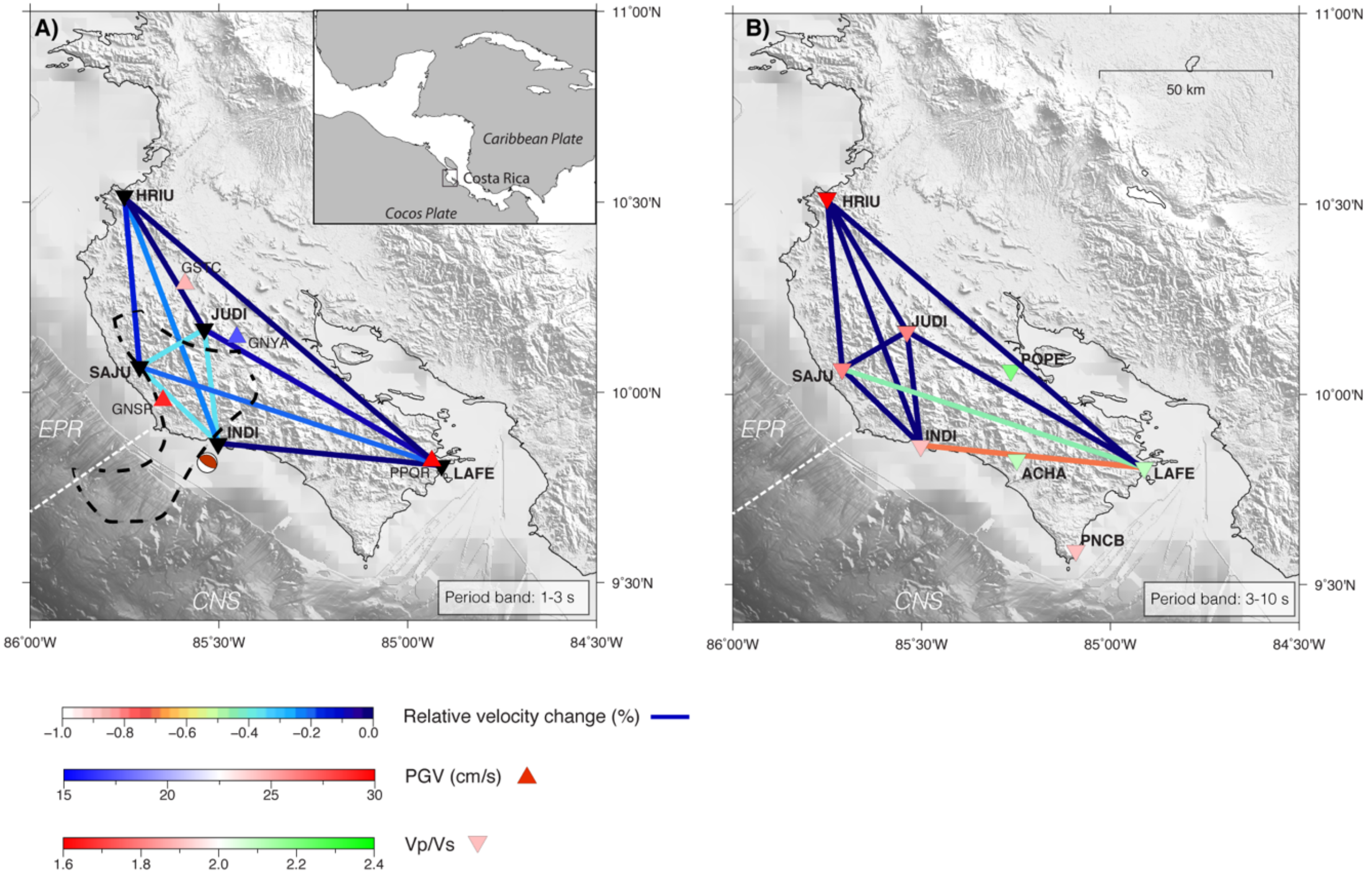
A)
HRIU
GSTC
JUDI
GNYA
SAJU
GNSR
INDI
PPOR
LAFE
EPR
CNS
Caribbean Plate
Costa Rica
Cocos Plate
Period band: 1-3 s
B)
50 km
HRIU
JUDI
POPE
SAJU
INDI
ACHA
LAFE
PNCB
EPR
CNS
Period band: 3-10 s
11°00'N
10°30'N
10°00'N
9°30'N
86°00'W
85°30'W
85°00'W
84°30'W
Relative velocity change (%)
−1.0
−0.8
−0.6
−0.4
−0.2
0.0
PGV (cm/s)
15
20
25
30
Vp/Vs
1.6
1.8
2.0
2.2
2.4

We find even stronger co-seismic velocity reductions (0.4- 0.6%) in the 3-10 s period band that also show spatial variability (Fig. 1.6B). Rayleigh waves in this frequency range are sensitive to velocity structure in the 5-15 km depth range (Fig. 1.5). Velocity reductions at longer period are only found in the southeastern portion of the Nicoya Peninsula, between stations located farther from the coseismic slip patch than those possessing the shorter period velocity reduction (Fig. 1.6). Analysis of these stations in the 5-10 s period band shows the same magnitude velocity reduction, while the 1-3 s period band indicates no velocity change (Fig. 1.8A), confirming that the velocity reduction occurs at depths below 5 km. This deeper (5-15 km) velocity reduction locates in the region where a previous receiver function study found extremely high, forearc V_p/V_s ratios that were interpreted as pore fluid overpressures. The vp/vs ratios determined at each station (Fig. 1.6B) reflect the average value for the entire forearc crust from the top of the subducting plate to the seismic station, a crustal section ranging between 16 km at the coast to about 30 km at the most inland station. Further support for the presence of fluids in the forearc in this region comes from results of an onshore-offshore magnetotelluric study conducted in 2007-2008 (Worzewski *et al*., 2011). This work imaged a low electrical resistivity anomaly (very conductive zone) at 12-15 km depth in the southeast portion of the Nicoya forearc that was interpreted as the presence of fluids derived from clay mineral dehydration reactions in the subducted crust.

We propose that the deep co-seismic velocity reduction results from over-pressured fluids reducing the effective stress and weakening the forearc crust, making it more susceptible to damage (increasing fracture density) from dynamic stresses. Of course static stress changes or post-seismic deformation following an earthquake may also be important in modifying seismic velocities at depth. Although it is unclear how crack opening and closure may operate under static stress (or strain) perturbations at depth, recent work reporting velocity changes associated with slow-slip events in Mexico (Rivet *et al.*, 2011; Rivet *et al.*, 2014) indicates that slow stress changes are capable of affecting elastic properties of the deep crust.

The negative volumetric strain (compression) in the southeastern portion of the Nicoya Peninsula at depths between 0-15 km, generated by the 2012 mainshock (Figure A-1), is inconsistent with the velocity reductions we observe.

To evaluate deformation related to afterslip as a possible source of the observed velocity reductions, we excluded from analysis the 70-day period following the earthquake that has previously been identified as the time constant associated with afterslip (Malservisi *et al.*, 2015). Results in the longest period bands (3-10 s and 5-10 s) still show a maximum reduction in velocity of ~0.5% with respect to the pre-main shock levels. This is comparable to results obtained using the entire post-seismic time period and indicates that deformation associated with afterslip is not a main contributor to the deep velocity reduction. Therefore, we favor the interpretation that dynamic stresses from seismic waves increased crack damage and decreased seismic velocities in areas that were already highly weakened from over pressured fluids.

Unlike the shallower velocity reductions that attain their peak value shortly following the main shock and recover only slightly in the following year (Fig. 1.6A), the onset of the deeper velocity reductions also closely follows the earthquake, but take several months to attain their peak value. They also appear to recover more than 50% of their velocity reduction in the year following the earthquake (Fig. 1.8A). This corroborates our conclusion that different processes are responsible for the deep and shallow velocity reductions. It also indicates that some permanent deformation is likely occurring in the near surface crust while a slow recovery process operates at depth. Our interpretation for the deeper velocity reductions under the Nicoya Peninsula is similar to a previous study implicating fluid pressurized crustal weakening from seismic waves as the cause of velocity reduction beneath the Japanese volcanic arc. Ours is the first observation of this mechanism operating in a subduction zone environment and demonstrates the potential to identify pressurized fluids in subduction zones using temporal variations of ambient seismic noise.

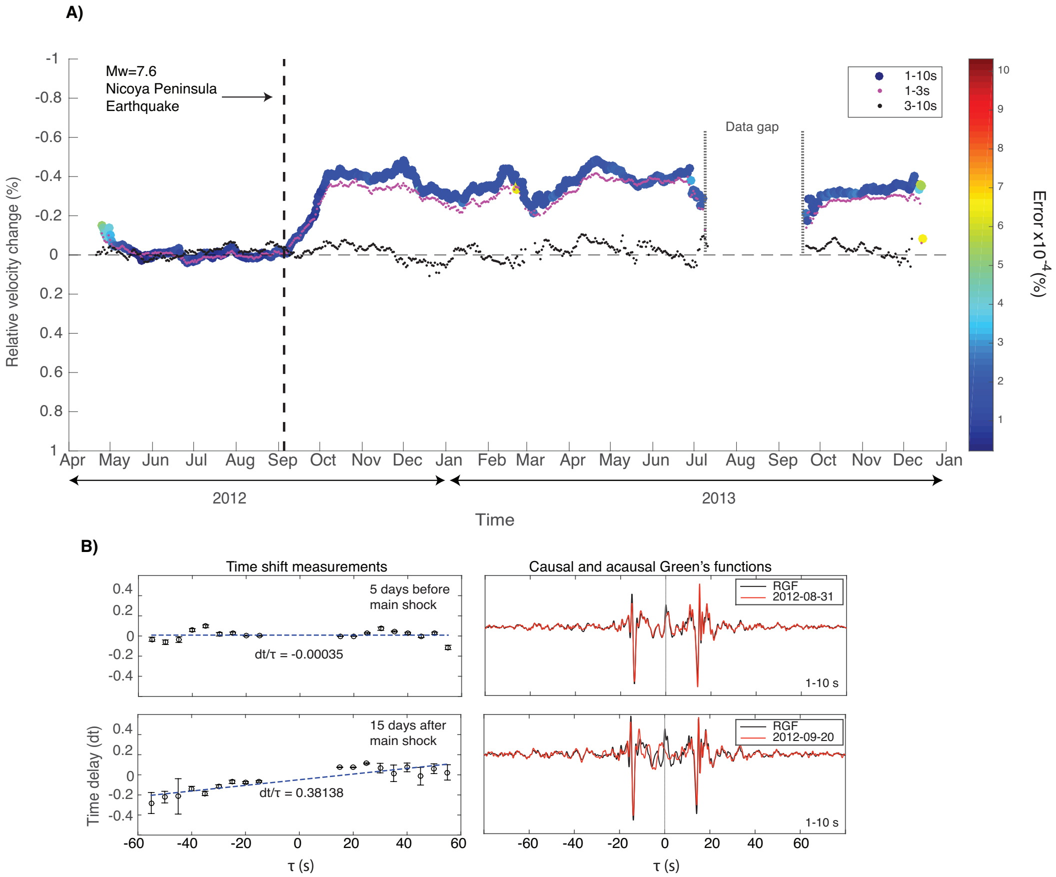

Figure 1.7. Green's Functions determined in the 1-10s period range. The figure shows the seismic velocity reductions, GFs and time delays associated with the 2012 Nicoya Peninsula earthquake for station pair INDI-SAJU in the 1-10 s, 1-3 s, and 3-10 s period bands. **(A)** The pre-seismic, co-seismic and post-seismic velocity variations between April 2012 and October 2013. The dashed line indicates the time of the main shock. Note the near identical velocity reduction in the 1-10 s and 1-3 s period bands and the lack of a velocity variation in the 3-10 s band. **(B)** RGF and daily GFs and time delays resulting from the cross-correlation of their coda filtered between 1-10 s: 5 days before and 15 days after the earthquake. The longer time period used after the earthquake was required to avoid mixing of post-seismic signals or aftershocks.

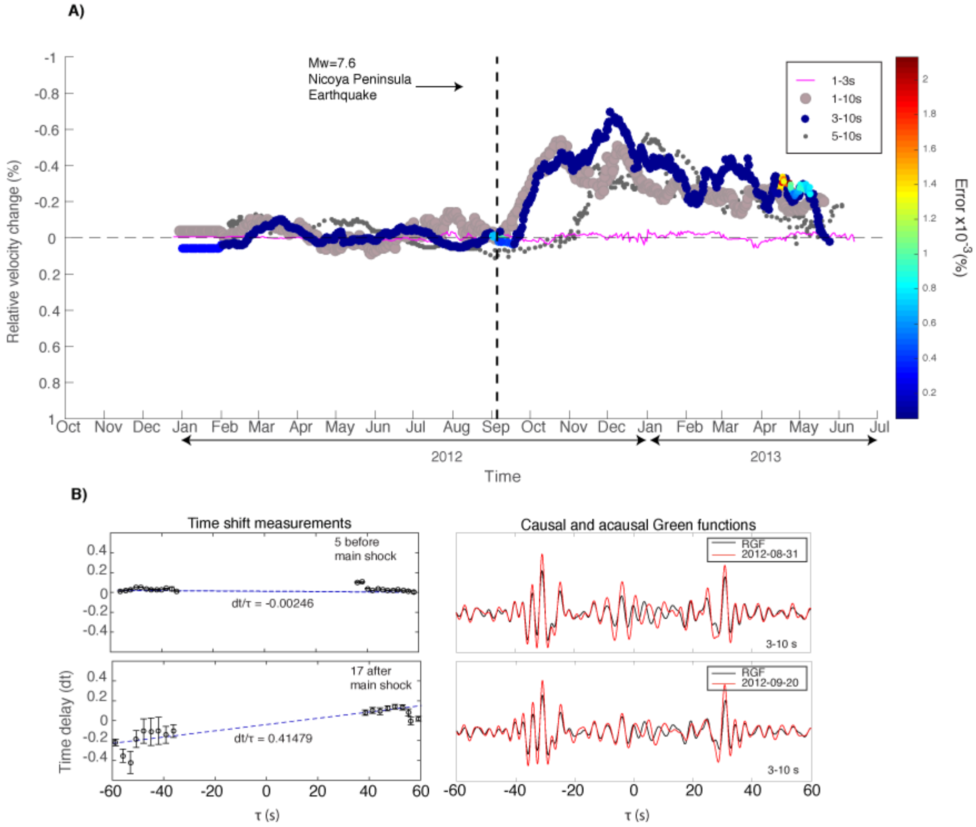

Figure 1.8. Green's Functions determined in the 3-10s period range. The figure shows the seismic velocity reductions, GFs and time delays associated with the 2012 Nicoya Peninsula earthquake for station pair INDI-LAFE in the 1-10 s, 1-3 s, 3-10 s and 5-10s period bands. **(A)** The pre-seismic, co-seismic and post-seismic velocity variations between February 2012 and June 2013. The dashed line indicates the time of the main shock. Note the similarity in the velocity reductions in the 1-10 s, 3-10 s, and 5-10s period bands confirming that the physical processes responsible are occurring at ~ 5-15 km depth. The delay in the velocity reduction apparent in the 5-10 s period band reflects the longer, 50 day stacks required to stabilize the analysis. **(B)** RGF and daily GFs and time delays resulting from the cross-correlation of their coda filtered between 3-10s: 5 days before and 15 days after the earthquake respectively.

CHAPTER 2 - AFTERSHOCKS OF THE 2012 (M_W 7.6) NICOYA, COSTA RICA EARTHQUAKE AND MECHANICS OF THE PLATE INTERFACE

Abstract. Subduction of the Cocos plate beneath the Nicoya Peninsula, Costa Rica, generates large underthrusting earthquakes with a recurrence interval of about 50 years. The most recent of these events occurred on 5 September 2012 (M_W 7.6). A vigorous sequence of more than 6400 aftershocks was recorded by a local seismic network within the first 4 months after the mainshock. We determine locations and focal mechanisms for as many aftershocks as possible with $M \geq 1.5$ occurring within the first 9 days of the mainshock, all aftershocks with $M \geq 3$ through the end of 2012, and all events with $M \geq 4$ through the end of 2015. We determine faulting geometries using regional full waveform moment tensor inversion for the largest events ($M \geq 4$) and P wave first-motion polarities for smaller events, producing a mechanism catalog with 347 earthquakes. Sixty percent of these events are identified as underthrusting and their locations are compared with spatial distributions of mainshock slip, afterslip, prior interplate seismicity, and slow slip phenomena to better understand the mechanical behavior of the plate interface. Most of the aftershocks on the megathrust occur up-dip of the coseismic slip, where afterslip is large, and between coseismic slip and shallow slow slip patches. The pattern of interplate seismicity during the interseismic period is similar to that for the aftershocks, but does not extend to as great of a depth. The coseismic slip extends even deeper than the interplate aftershocks, suggesting that the

mainshock ruptured a strongly locked patch driving downdip slip into the conditionally stable part of the deep plate interface that also hosts slow slip. About 80% of the aftershocks have one nodal plane oriented favorably to promote failure from static stress changes following the mainshock and early afterslip, while most others occur in regions of large afterslip.

2.1. INTRODUCTION

Aftershock studies of many large earthquakes indicate that most aftershocks occur outside of regions of large coseismic slip or at transitions from high to low slip (e.g., Hsu *et al*., 2006; Asano *et al*., 2011; Rietbrock *et al*., 2012). Many studies have tried to correlate aftershock occurrence with afterslip, with mixed results. However, few of these studies isolate the interplate aftershocks as needed to confidently evaluate the plate boundary behavior. For many recent megathrust events, detailed aftershock studies indicate that a significant fraction of the aftershocks occurred off the main thrust interface (e.g., Ito *et al*., 2011). Here we determine locations and focal mechanisms of aftershocks of the 5 September 2012, M_W 7.6 Nicoya Peninsula, Costa Rica earthquake and isolate those that occur on the plate interface. We then compare their locations to the distributions of mainshock slip, afterslip, slow slip events, and interseismic interplate seismicity patterns to better understand the mechanical properties of the plate interface.

The 2012 earthquake ruptured a well-identified mature seismic gap that had previously ruptured in 1950. With the Nicoya Peninsula extending seaward, well out over the plate boundary, seismic and GPS instrumentation was deployed in the gap several decades before the 2012 rupture. The late interseismic, co-seismic and postseismic phases of the earthquake cycle were thus all well-recorded by local GPS and seismic networks. These data have been used to construct models of the interseismic strain accumulation on the plate interface (Feng *et al*., 2012; Xue *et al*., 2015; Kyriakopoulos *et al*., 2016), the distributions of co-seismic slip (Yue *et al*., 2013; Protti *et al*., 2014; Liu *et al*., 2015; Kyriakopoulos *et al.,* 2016) and afterslip (Malservisi *et al*., 2015), the timing and location of slow slip and tremor events (Walter *et al*., 2009; Dixon *et al*., 2014), the foreshock behavior (Walter *et al*., 2015), and interseismic seismicity patterns (Newman *et al*., 2002; DeShon *et al*., 2006; Hansen *et al*., 2006).

Here, we generate a catalog of 347 focal mechanisms for well-located aftershocks and seek to better characterize the slip behavior of the plate interface in a region where past studies have documented strong lateral variations in thermal structure, pore fluids, earthquake activity and fault frictional behavior (Langseth and Silver*,* 1996; Pascal and Schwartz, 2013). We also perform Coulomb stress change calculations to compare all aftershock locations and mechanisms to static stress changes induced by the mainshock rupture.

2.2. TECTONIC SETTING

Costa Rica is part of the Central America volcanic front, formed by subduction of the oceanic Cocos plate beneath the continental Caribbean plate along the Middle America Trench (MAT) at a rate of ~85-90 mm/yr (DeMets *et al.*, 2010) (Fig. 2.1). This rapid convergence rate has generated magnitude 7+ earthquakes in 1853, 1900, 1950 and 2012 along the Nicoya Peninsula, the northwestern margin of the Costa Rica subduction zone. Due to the advantageous location of the Nicoya Peninsula extending seaward over the seismogenic zone, regional broadband seismic and continuous GPS stations have provided unusual instrumental coverage of the megathrust activity over the last decade. Several studies have shown that the seismogenic zone below the Nicoya Peninsula is characterized by strong lateral variations in thermal structure (Langseth and Silver, 1996), pore fluids (Audet and Schwartz, 2013; Chaves and Schwartz, 2016), and earthquake behavior (Newman *et al.*, 2002).

These variations are largely attributed to differences in genesis of the subducting lithosphere; the northwestern region was generated at the East Pacific Rise (EPR) and the southeastern region was formed at the Cocos-Nazca spreading center (CNS). The position of the EPR-CNS boundary is well defined by magnetic anomalies and high-resolution bathymetry data (Barckhausen *et al.*, 2001). It extends ~80 km from the morphological rough-smooth boundary in the older part of the Cocos plate to its orthogonal convergence with the MAT off the central Nicoya Peninsula (Fig. 2.1).

In addition to hosting large earthquakes every 50 to 60 years, seismic tremor activity and slow-slip events (SSEs) have been observed every ~ 21 ± 6 months near transitions between seismic and aseismic slip areas on the megathrust (Dixon *et al*., 2014). Geodetic observations prior to the 2012 Nicoya earthquake identified a region of slip deficit that tightly encompassed the subsequent rupture area of the event (e.g., Feng *et al*., 2012). Regions of the plate interface up and down-dip of this stick-slip zone accommodate relative plate motions aseismically, with numerous SSEs being well recorded since 2007. This pattern suggests a partitioning of the plate interface into regions of frictionally stable or unstable sliding behavior.

The extensive regional seismological and geodetic instrumentation available to monitor megathrust activity at close range provide valuable data for studying the partitioning of sliding behavior on the plate boundary below the Nicoya Peninsula through the earthquake cycle. Foreshock activity and a vigorous aftershock sequence were recorded by the local seismic network. The foreshock activity was studied by Walter *et al*. (2015) and found to initiate 9 days before the 2012 Nicoya mainshock, plausibly triggered by the regional occurrence of the 27 August 2012 M_W 7.3 El Salvador earthquake. This foreshock sequence culminated with a cluster of small-magnitude (< 2.2) earthquakes preceding the mainshock by about 35 min and locating within 15 km of its hypocenter (Walter *et al*., 2015). In this paper, we focus on the vigorous aftershock sequence and what it contributes to our understanding of the Nicoya megathrust behavior.

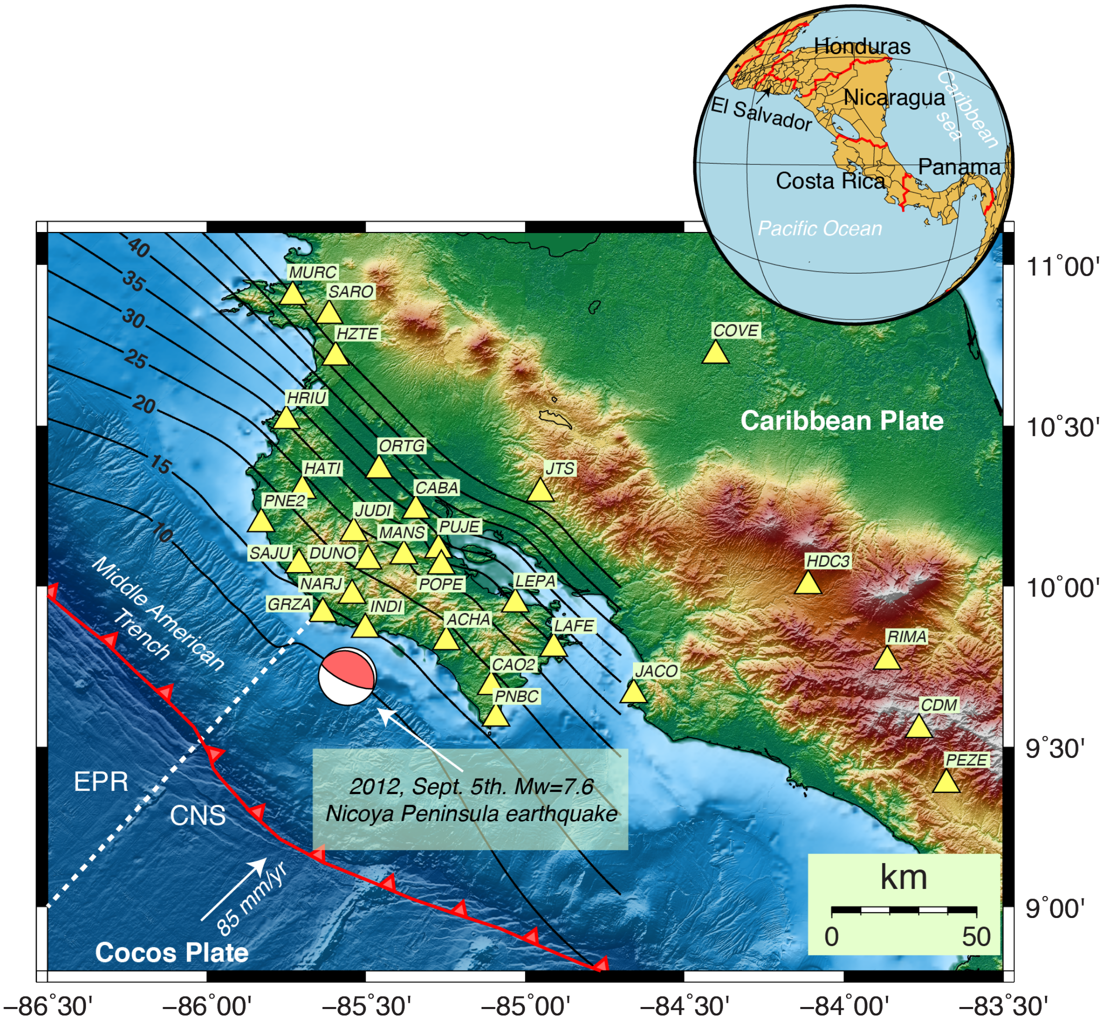

Figure 2.1. Tectonic setting and instrumentation. Map view showing the spatial distribution of the Nicoya Seismic Cycle Observatory and OVSICORI-UNA seismic stations used in this study. Contour lines (Deshon et al., 2006) indicate the depth to the top of the subducted slab. The dotted line represents the East Pacific Rise (EPR)-Cocos Nazca Spreading center (CNS) boundary (Barckhausen et al., 2001). The epicentral location and focal mechanism of the 5 September 2012, M_W =7.6 Nicoya Peninsula earthquake are also indicated.

2.3. DATA AND METHODS

2.3.1. HYPOCENTER LOCATIONS

Seismic data used in this study come from stations of the Volcanological and Seismological Observatory of Costa Rica (OVSICORI-UNA) network and the Nicoya Seismic Cycle Observatory (Figure 2.1), an international and multi-university network of GPS and seismic stations operating on the Nicoya Peninsula, Costa Rica (Dixon *et al.*, 2013). We start with an initial earthquake catalog for the period from the mainshock through the end of 2012 that was generated using the Antelope seismic database automatic earthquake detection and location tools. Subsequently, additional phase arrivals were analyst-picked and reviewed for all events within 9 days of the mainshock and for events with $M \geq 3$ through the end of 2012.

The phase information was then used to relocate the events within a local 3D velocity model (DeShon *et al.*, 2006) using the software SIMULPS (Evans *et al.*, 1994) which provides absolute hypocenter locations. Only those earthquakes with the best available locations were retained. We justify focusing our study of the complete aftershock sequence on the first ten days based on the similarity of the Gutenberg-Richter (GR) relationship for this time period versus the four-month period following the mainshock. Both time periods indicate catalog completeness down to $M_C = 2.2$ and b values between 0.80 and 0.85 (Fig. B-1). Due to the deficit in intermediate-to-large magnitude earthquakes that followed the mainshock in 2012, we also determined focal mechanisms for all events with magnitude $M \geq 4.0$ between 2013 and 2015. Initial hypocenter locations for these events were determined by the OVSICORI-UNA.

2.3.2. DETERMINATION OF EARTHQUAKE FOCAL MECHANISMS

We apply a regional moment tensor inversion (MT) methodology to determine focal mechanisms for all events in our catalog with magnitude above 4. Second rank general moment tensor inversion is routinely used to obtain source mechanisms of seismic events at teleseismic (e.g., Dziewonski *et al.*, 1981; Ekstöm *et al.*, 2005) and regional distances (Jost and Herrmann, 1989; Minson and Dreger, 2008). In this study, we adopt the time domain moment tensor inversion approach (Dreger and Helmberger, 1993), where the seismic source is simplified by considering a spatial and temporal point source, given by:

$$U_n(x,t) = M_{ij} \cdot G_{ni,j}(x,z,t) \tag{2.1}$$

Where U_n is the observed nth component of displacement, M_{ij} is the scalar seismic moment tensor and $G_{ni,j}$ is the nth component Green's function for specific force couple orientations. Equation (2.1) is solved using a least squares approach for a given source depth. We solve for the deviatoric seismic moment tensor M_{ij} which is decomposed into the scalar seismic moment, a double couple (DC) moment tensor (defined by the strike (ϕ), dip (δ) and rake (λ) angles of both nodal planes) and a compensated linear vector dipole (CLVD) moment tensor. The moment tensor decomposition is performed following Jost and Herrmann (1989) and is represented as percent DC and CLVD (Fig. 2.2 and Fig. B-2). For each station, three component waveform data are instrument corrected, integrated to displacement and band-pass filtered using a Butterworth filter with corners at 0.02 and 0.05 Hz for events with M ≥ 4.2, and corners at 0.02 and 0.1 Hz for smaller magnitude earthquakes that contain high signal-to-noise ratios. The horizontal traces are rotated to the great circle path to generate tangential and radial components. Green's functions are computed using a frequency-wave number integration algorithm (Saikia, 1994) for the 1D local velocity model (DeShon *et al.*, 2006), and filtered similarly to the data. In order to perform the MT inversion, we assume that epicenter locations represent the actual geographical coordinates of the centroid locations and the source depth is determined iteratively, finding the solution with the largest variance reduction (VR), defined by:

$$VR = \left[1 - \frac{\sum_i \sqrt{(data_i - synth_i)^2}}{\sqrt{{data_i}^2}}\right] \cdot 100 \qquad (2.2)$$

Where *data* and *synth* represent the data and the Green's function time series of the *ith* station, respectively. Figure 2.2 shows an example of the MT process for a particular aftershock (*M*W 5.5) in the catalog that occurred on 8 September 2012 at 20:29:29 UTC (EVID 107).

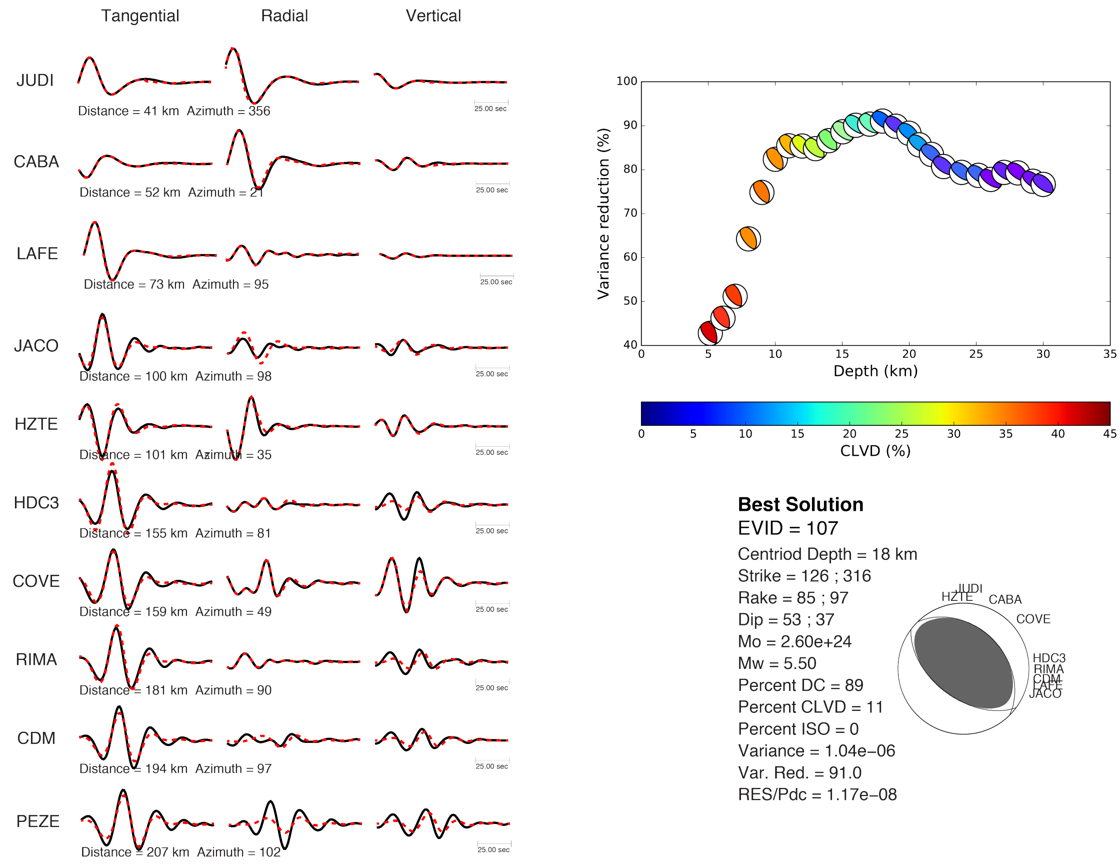

Figure. 2.2. Regional moment tensor inversion of a large aftershock, M_W = 5.50, performed using stations from the OVSICORI-UNA network and the Nicoya Seismic Cycle Observatory network. The figure shows the waveform fit between data (continuous lines) and synthetics (dashed lines), the moment tensor decomposition and source parameters. The variance reduction as a function of depth is presented as well. Focal mechanisms are color coded by CLVD (%).

Small events ($1 \leq M \leq 3.9$) represent the majority of the earthquakes in our catalog. Focal mechanisms for small events are commonly determined using P wave first motion polarities (Reasenberg and Oppenheimer, 1985). As an improvement on previous algorithms, Hardebeck and Shearer (2002) developed a method for determining first motion focal mechanisms (the so-called HASH method) that differs from previous techniques in that it accounts for errors in the assumed earthquake locations and seismic velocity model, as well as in the polarity observations. In this study, we use HASH with manually picked P wave polarities from the Antelope seismic database and our improved earthquake locations to determine focal mechanisms for hundreds of small events with magnitudes between 1.5-5.4.

The HASH method assumes a range in takeoff angles and implements a grid search over all possible focal geometries to identify the acceptable group of solutions for each earthquake. The root-mean square deviation between the acceptable nodal planes and the favored nodal plane is the nodal plane uncertainty (Hardebeck and Shearer, 2002; Sumy *et al.*, 2014). The mean of the nodal plane uncertainties represents the focal mechanism quality (e.g. Kilb and Hardebeck, 2006; Yang *et al.*, 2012).

However, the quality of the focal mechanism for a given event also depends on the number of observations and the azimuthal distribution of these observations over the focal sphere, or the azimuthal gap between stations. If the azimuthal coverage over the focal sphere is not adequate, determination of the focal geometries will be limited or biased, regardless of the number of stations used in the computation. Thus, we base the quality of the mechanisms (where A: best and D: worst, e.g. Hardebeck and Shearer, 2002) on the mean nodal plane uncertainty and the azimuthal station distribution. In total, we computed 583 earthquake focal mechanisms; 100 using MT inversion and 483 using HASH.

These events were relocated using hypoDD (Waldhauser and Ellsworth, 2000) and a recently developed algorithm called GrowClust (Trugman and Shearer, 2017). Both algorithms determine relative earthquake hypocenters using differential travel times obtained from waveform cross-correlation of pairs of events observed at a set of common stations (Fig. B-3). However, the latter takes an alternative approach to minimize the residuals between the observed and predicted differential travel times that requires no explicit matrix inversion, and optimizes the L1-norm (instead of L2-norm used by hypoDD) of the differential travel time residuals, improving its robustness to data outliers (Trugman and Shearer, 2017). GrowClust applies a hybrid hierarchical clustering algorithm that simultaneously groups events into clusters based on waveform similarity and relocates each event with respect to its cluster. Furthermore, it implements a non-parametric resampling approach to estimate location uncertainties, allowing an assessment of the relocation results.

Due to its robustness for assessing hypocenter relocations and relative location errors (we found relative horizontal and vertical errors on the order of hundreds of meters), we implement the GrowClust algorithm to produce a final catalog of 347 relative earthquake locations and focal mechanisms. We selected only those events with quality A and B focal mechanisms for this subset. This catalog is listed in Table B-1. A comparison of epicentral locations for these 347 events determined using both relocation methods is shown in Figure B-3 along with a close-up window exhibiting the clustering of events produced with the GrowClust algorithm. In general, both techniques result in very similar locations, with GrowClust providing superior error estimates.

HASH assumes uncertainties in earthquake location, velocity structure and first motion polarity assessment in its determination of the best focal mechanism. Therefore, the small differences in azimuth and take-off angle that result from relocation using HypoDD or GrowClust, do not require us to re-compute faulting geometries after earthquake relocation. A total of 21 of these re-located events are reported in the Global CMT catalog. Figure 2.3 compares the focal mechanism solutions and magnitudes obtained using the MT, HASH and Global CMT methods for the largest events in our catalog that have multiple solutions determined. In general, the agreement between faulting geometries and M_W is quite robust (although it is well known that the precision of moment magnitude estimates decreases for events with $M_W \leq 5.0$).

For events with multiple focal mechanism solutions, we use the MT solution. Since much of the following analysis relies on events located on the plate interface, we identify these events based on their location being near (within 8 km) the previously defined plate interface (DeShon *et al.*, 2006) and having nodal planes consistent with the mainshock (a total of 210 events). Depth estimates have uncertainties and since we view it as unlikely that there are many thrust events on shallower or deeper planes parallel to the megathrust, we consider mechanism information more reliable than depth in identifying events located on the plate interface. We therefore use a generous 8 km distance range from the megathrust together with focal mechanism constraints to define events occurring on the plate interface. The range of thrust faulting geometries we considered consistent with the mainshock is indicated in Table 2.1. In the following, we refer to these 210 events as interface thrust aftershocks.

Table 2.1. Focal mechanism orientation selection criteria for underthrusting events.

	Nodal Plane	**Strike (°)**	**Dip (°)**	**Rake (°)**
Mainshock	1 2	308 115	17 73	102 86
Selection Criteria	1 2	260-350 75-145	< 40 > 50	35-135 35-135

Figure. 2.3. Evaluation of focal mechanisms, magnitude and seismic moment for the 10 largest events in 2012. A) Focal mechanisms are computed using both methods: The *P*-wave first motion arrivals (*HASH* method) and the regional moment tensor inversion (*MT*) and compared with the solutions presented in the Global CMT (GCMT) catalog. Events are organized by id number (Table B-1) M_W is from MT and focal mechanisms are color coded by depth (km). Note that the solutions from GCMT and MT sometimes differ substantially from the HASH solution. B) Estimated M_W comparison between MT and Global CMT solutions for the largest underthrusting events on the Nicoya Peninsula between the occurrence of the 2012 earthquake and the end of 2015.

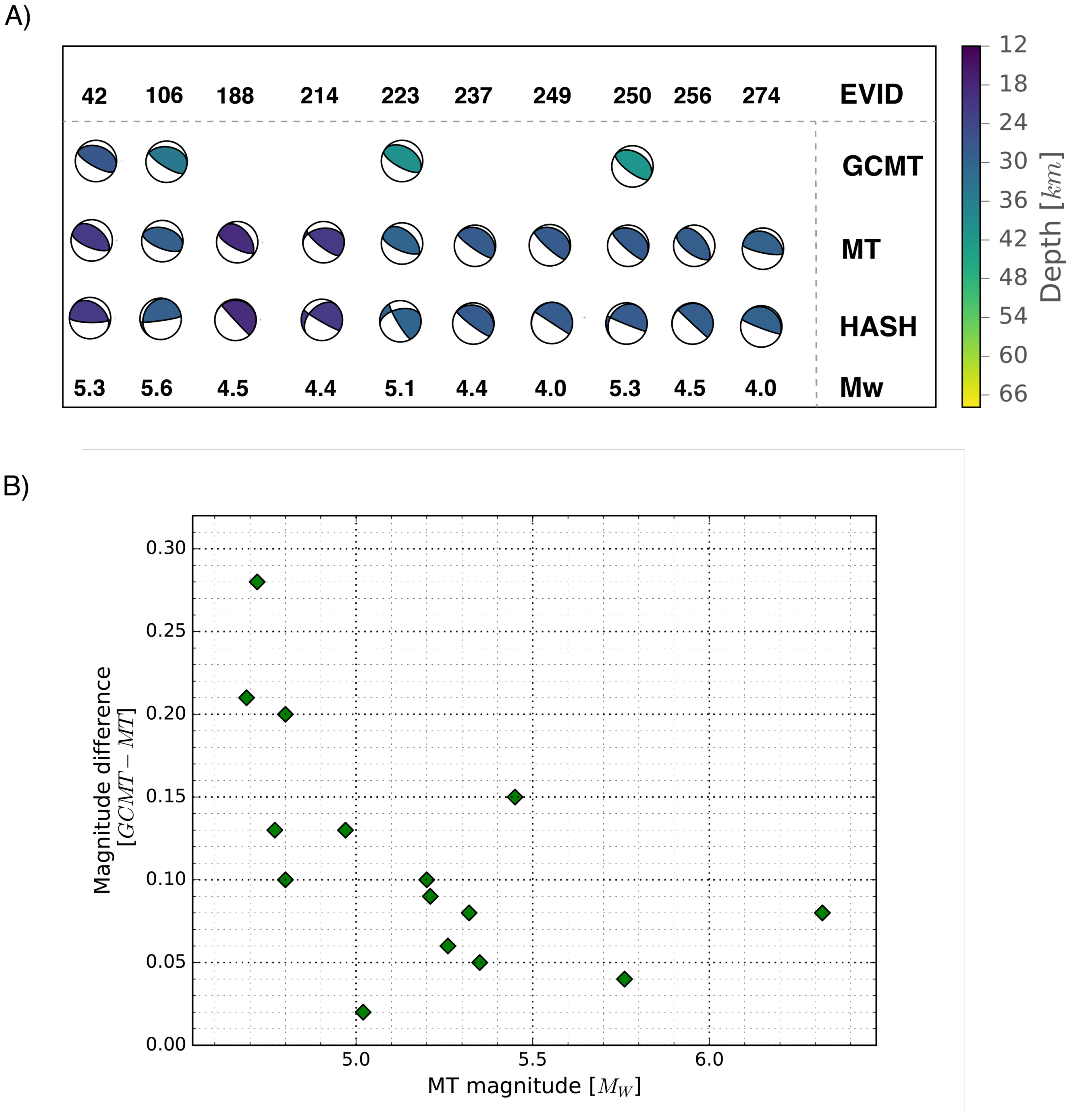
A)
42
106
188
214
223
237
249
250
256
274
EVID
GCMT
MT
HASH
5.3
5.6
4.5
4.4
5.1
4.4
4.0
5.3
4.5
4.0
Mw
12
18
24
30
36
42
48
54
60
66
Depth [km]
B)
Magnitude difference [$GCMT - MT$]
0.00
0.05
0.10
0.15
0.20
0.25
0.30
5.0
5.5
6.0
MT magnitude [M_W]

2.4. RESULTS AND DISCUSSION

The locations of 347 relocated earthquakes with computed focal mechanisms, ranging in magnitude between 1.5 and 6.4, are shown in Figure 2.4. Almost all of the events are located either within the downgoing slab or on the plate interface. Most of the events we interpret as occurring on the thrust interface locate up-dip of the peak co-seismic slip and at the southern margin of the Peninsula (Figure 2.5), where co-seismic rupture also reached more than 1 m of slip (Yue *et al*., 2013; Protti *et al*., 2014, Liu *et al*., 2015). Many of the events up-dip of the peak co-seismic slip occur in the offshore slip-deficit patch identified with GPS and Interferometric Synthetic Aperture Radar (InSAR) (Feng *et al*., 2012; Xue *et al*; 2015), that failed to slip during the mainshock (Protti *et al*., 2014).

Aftershock sequences observed for the 2005, M_W 8.7 Nias-Simeulue, Sumatra earthquake (Hsu *et al*., 2006), the 2010, M_W 8.8 Maule earthquake (Rietbrock *et al*., 2012) and the 2011 M_W 9.0 Tohoku-Oki megathrust (Asano *et al*., 2011) show a preponderance of events that rupture in areas surrounding the main co-seismic slip asperity, either at transitions from high to low slip or in low slip regions, with fewer and small magnitude events locating within the maximum co-seismic slip area. Similarly, Ito *et al*. (2004) showed that aftershocks of the 2003, M_W 8.0 Tokachi-Oki earthquake exhibited a spatial distribution that localized off the main co-seismic slip patch, northwest from the epicenter. For large megathrust earthquakes, it is widely accepted that the mainshock releases a large fraction of the strain accumulated during the interseismic cycle. Aftershock seismicity, especially the largest events, should therefore be predominantly located in areas of transition between high and low slip or on the margins of high-slip regions were the Coulomb static stresses have increased due to the sudden slip during the main event. Nicoya interplate aftershocks also appear to be sandwiched between regions of large co-seismic slip (down-dip) and slow slip (up-dip) in the northwest or between two patches of slow slip in the southeast (Fig. 2.5), confirming a previous suggestion that the Nicoya plate interface may have a sharp along dip transition in frictional properties from velocity weakening at depth to velocity strengthening or conditionally stable at shallow depth (Walter *et al.*, 2013).

The aftershocks with thrusting mechanisms occur in two dominant spatial clusters (clusters C1 and C2 in Fig. 2.4 and Fig. 2.5) while there is a third spatial cluster with predominantly strike-slip mechanisms located offshore to the northwest (cluster C3 in Fig. 2.4). The lack of activity between C1 and C2 might be due to the lack of co-seismic slip in this region or a possible change in the frictional properties of the plate interface. This gap in aftershock activity correlates with a shallowing of the plate interface in a recently proposed model (Kyriakopoulos *et al.*, 2015). If the plate interface experiences different physical conditions in this region because of its distorted geometry, it might also have a different mode of slip, with stable sliding rather than stick-slip motion.

This interpretation is supported by the work of Wang and Bilek (2011) who suggested that subducted topographic highs might result in stable sliding due to preferential release of fluid and a reduction in the effective normal stress.

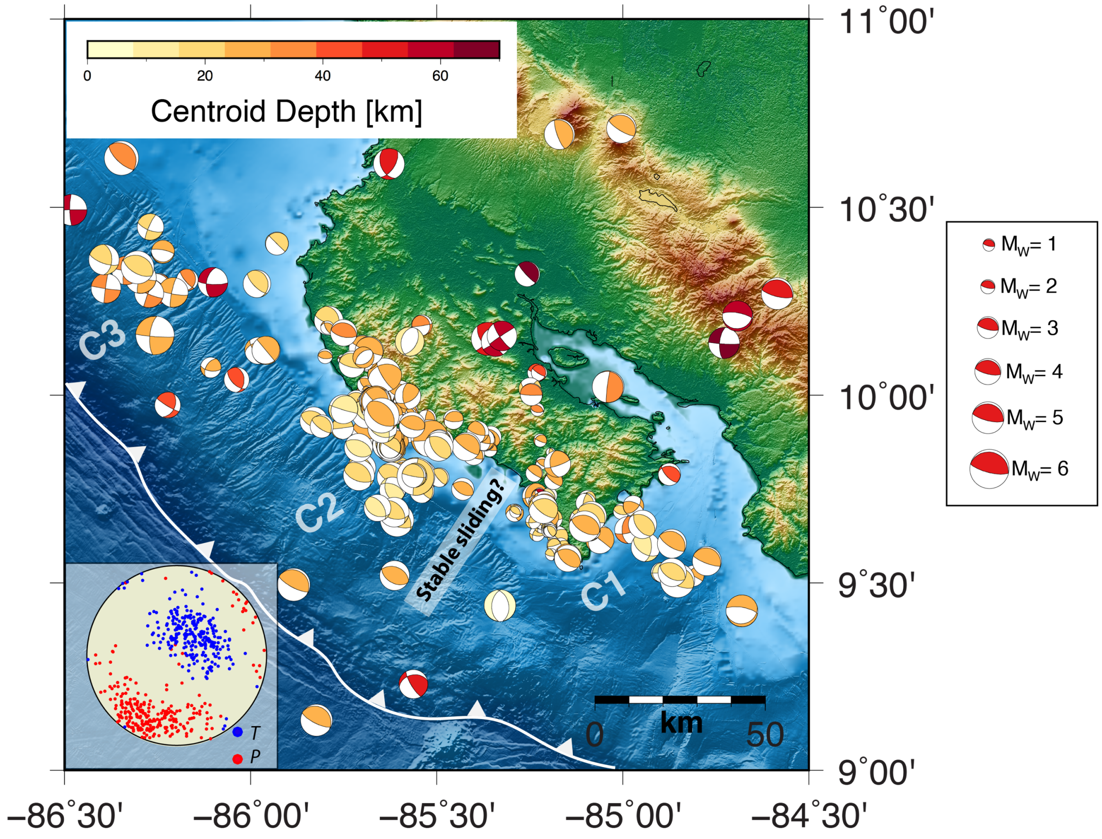

Figure 2.4. A. Map showing the spatial distribution of all well-located aftershocks with focal mechanisms computed for the 5 September 2012 Nicoya Peninsula Costa Rica earthquake sequence. The pressure (P) and tension axes (T) diagram is embedded within the figure. Focal mechanisms are color coded by centroid depth. The size of the mechanism corresponds with the magnitude of each event. Note the clustering (groups: C1, C2 and C3), and segmentation of the plate interface, as discussed in the text.

Figure 2.5. A) Spatial distribution of underthrusting events that followed the 5 September 2012, Nicoya Peninsula, Costa Rica earthquake. Underthrusting events are identified by their location relative to the plate interface and their focal mechanisms. The colored contours in the central and southern margins of the Peninsula represent the coseismic rupture area of the mainshock (slip increments of 0.5 m) Liu *et al*., (2015). The magenta contours updip and downdip highlight the regions of in accumulated slow slip between 2007 and 2012 (Dixon *et al*., 2014). Cross-section D-D' shows the distribution of events located north of the EPR-CNS boundary. Note the difference in depth extension along strike.

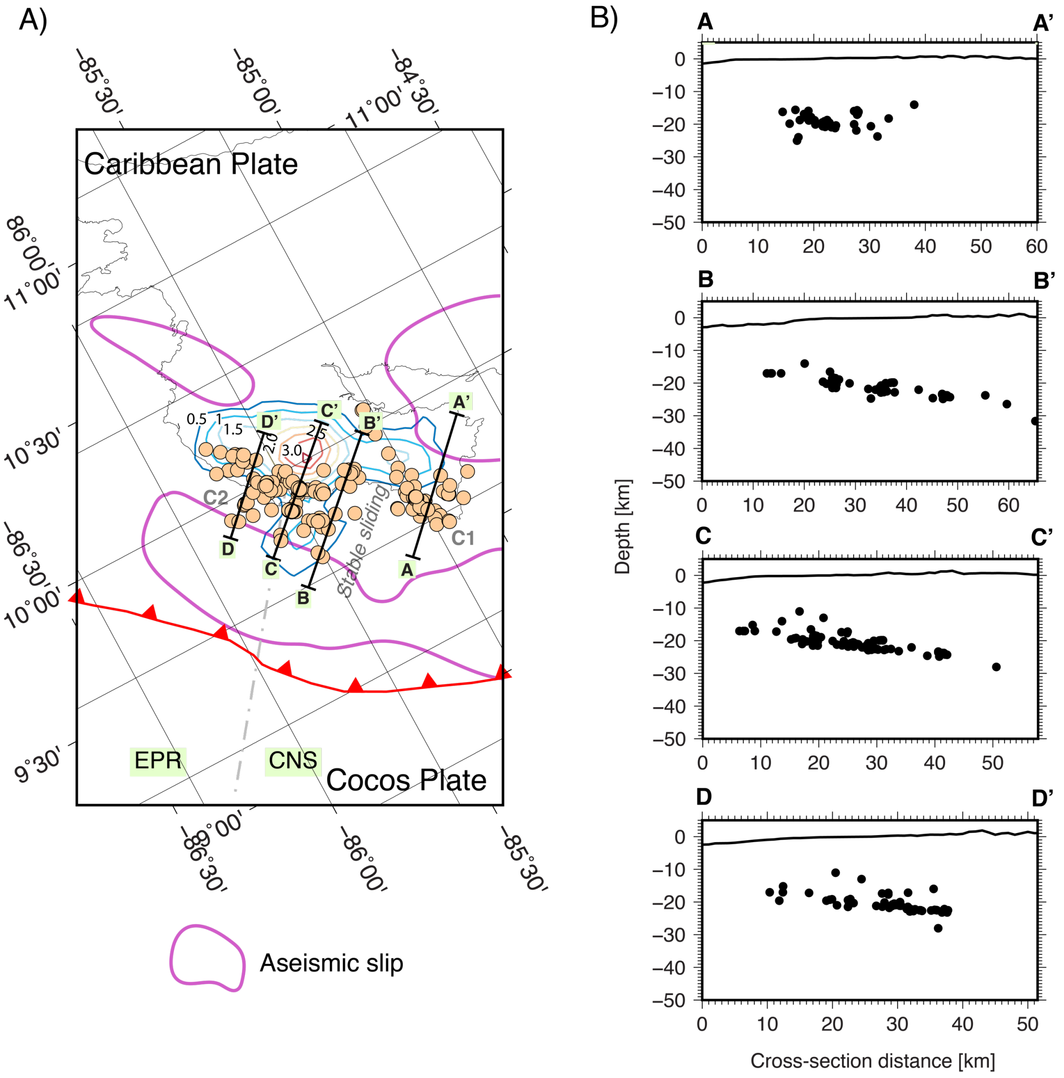
A)
B)
Caribbean Plate
Cocos Plate
EPR
CNS
Stable sliding
C1
C2
A
A'
B
B'
C
C'
D
D'
0.5
1
1.5
2.0
2.5
3.0
−85°30'
−85°00'
−84°30'
11°00'
10°30'
10°00'
9°30'
−86°30'
−86°00'
−85°30'
Aseismic slip
Depth [km]
Cross-section distance [km]
0
−10
−20
−30
−40
−50
10
20
30
40
50
60

Cross-sections of the low angle thrust faulting events within seismicity clusters C1 and C2 are consistent with previous observations that show a change in the depth of plate interface events across the EPR-CNS plate suture (Protti *et al*., 1994; Newman *et al*., 2002; Hansen *et al*., 2006). In the northern part of the Peninsula (cluster C2), most of the underthrusting events are in the depth range between 18 and 30 km depth. To the south (cluster C1 in Fig. 2.5), underthrusting events show a ~5 km reduction in depth with most events locating between 13 and 25 km in depth. This variability in the depth of interplate seismicity has been linked to the difference in the thermal structure of subducted lithosphere associated with different genesis; colder EPR (deeper seismicity) subducting to the north and warmer CNS (shallower seismcity) in the south (Langseth and Silver, 1996).

All Nicoya aftershock thrust events locate at depths between 10 to 32 km, with a peak in the kernel density estimation (KDE) function at 20 km (Fig. 2.6). Hypocenters determined using the same velocity model for underthrusting events that occurred before the mainshock have a similar distribution of depths (Deshon *et al*., 2006, Hansen *et al*., 2006), spanning from 10 to ~30 km, with a peak in the KDE at 18 km (Fig. 2.6). Co-seismic slip during the Nicoya Peninsula earthquake spanned a larger depth range of the plate interface, with slip distributed between ~5 to 35 km, but large slip concentrated below 20 km (Fig. 2.6). These depth profiles of earthquake behavior during the interseismic, co-seismic and post-seismic stages of the earthquake cycle suggest the following about the mechanical behavior of the plate interface: 1) the seismogenic zone, where earthquakes can nucleate, extends from ~10 to 32 km; 2) the lower few km of this region was completely locked during the late interseismic stage such that no underthrusting events occurred in this depth range prior to the mainshock but aftershocks did rupture this depth range; and 3) the mainshock rupture extended into conditionally stable parts of the plate interface both up and down-dip of the seismogenic zone (Fig. 2.6). Large slow slip events accompanied by tremor have occurred repeatedly at both shallow (0-10 km) and deep (30-50 km) depths in this region (Dixon *et al.*, 2014) and fit well with this depth-variation along the plate interface.

In addition to the interplate events, focal mechanisms were computed for a number of $M \geq 4$ aftershocks that locate at depth within the subducting lithosphere offshore the northwest margin of the Nicoya Peninsula between 20 and 35 km in depth (Cluster C3 in Fig. 2.4). The majority of the events in this cluster C3 have nearly pure strike-slip mechanisms with shallow-plunging northeast-southwest oriented pressure axes, consistent with the orientation of the regional maximum compressive stress direction.

Local seismicity catalogs created for specific periods of time in 1999, 2007, and 2009 also contain a large number of events at this same location, demonstrating that this activity is persistent and not simply related to the occurrence of the mainshock (e.g. clusters OC1 and OC2 in Fig. B-4). Because subduction of the oceanic lithosphere is at an oblique angle to the trench, internal deformation (contortions) of the downgoing plate during the subduction process could explain the occurrence of these events (e.g. Pacheco and Singh, 2010).

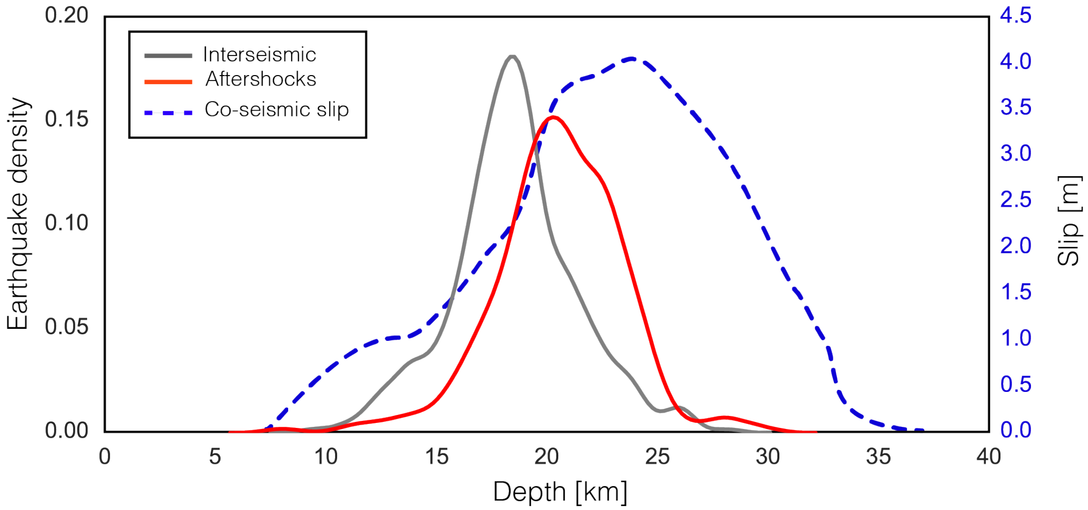

Figure 2.6. Kernel Density Estimate (KDE) functions for the depth distribution of underthrusting events during the interseismic period (Deshon *et al*., 2006) and the aftershock sequence of the 2012 Nicoya Peninsula earthquake (continuous line) plotted with the co-seismic slip (m) generated by the mainshock (dotted line).

Although the large majority of low angle thrust focal mechanisms observed in this study are consistent with the regional stress orientation given by the principal pressure (*P*) and tension (*T*) axes (here, we consider the average directions of the *P* and *T* axes to be indicators of the general orientations of the maximum compressive stress, σ_1, and the least compressive stress, σ_3), and the slip history on the megathrust (Yue *et* *al*., 2013; Protti *et al*., 2014, Liu *et al*., 2015), a diversity in fault geometries with respect to the mainshock focal mechanism is observed. These deviations are possibly linked to Coulomb static stress changes (earthquake interaction) imposed by the mainshock, earthquake afterslip (Malservisi *et al*., 2015), spatial heterogeneities along the plate interface (Fagereng and Sibson, 2010), or possibly a combination of all of these.

2.4.1. COULOMB STATIC STRESS CHANGES

It has been demonstrated that large earthquake ruptures permanently deform the surrounding medium, changing the stress conditions of nearby crustal materials as a function of their location, geometry and sense of slip (Toda *et al*., 2011a). Unlike dynamic stress (an oscillatory wave field that can trigger earthquakes both near to and far from the source), earthquake interaction through the static stress field can result in both an increase in seismicity in areas of co-seismic static stress increases and seismic quiescence in stress shadow areas (Harris and Simpson, 1996). The brittle failure of faults is thought to be a result of the combination of the effective normal and shear stress conditions, commonly quantified as the Coulomb failure criterion (e.g., King *et al*., 1994; Scholz, 2002), defined as:

$$\Delta CFS = \Delta\tau + \mu'(\Delta\sigma) \tag{2.3}$$

where τ is the shear stress on the fault plane (positive in the inferred direction of slip),

σ is the normal stress (positive for unclamping) and μ' is the apparent coefficient of friction. Failure is promoted if ΔCFS is positive and inhibited if negative. The location, geometry and slip distribution of the earthquake rupture as well as the friction coefficient, play an important role in the calculation of the ΔCFS produced by an earthquake. Previous work (e.g. King *et al.*, 1994; Hardebeck *et al.*, 1998; Stein, 1999) has demonstrated that an increase or decrease in the Coulomb static stresses off the causative fault of less than 1 bar (0.1 MPa), is sufficient to promote either earthquake failure or seismic quiescence, respectively. Due to its apparent role in triggering/halting of aftershocks and subsequent mainshocks on nearby faults (within a distance proportional to a few fault dimensions), Coulomb static stress changes have been proposed as a basis for evaluating short term earthquake hazards in multiple tectonic environments.

The Coulomb static stress change induced by the 2012 Nicoya earthquake was computed on the plate interface using the co-seismic slip model of Liu *et al*. (2015), combined with the contribution of the first 3-hr afterslip deformation (Malservisi *et al*., 2015) following the approach of Toda *et al*., (2011c). We assumed a homogeneous elastic half space and a common choice for the friction coefficient of 0.4 (It has been proven difficult to discriminate among possible values of friction coefficient in Coulomb static friction studies and a mid-value of 0.4 is commonly adopted. We consider a range from 0.2 to 0.8, and 0.4 actually optimizes the consistency of predicted Coulomb stress changes and aftershock occurrence for our data, but it does not necessarily reflect the strength of the megathrust).

The overall spatial distribution of most of the larger underthrusting events up-dip of the area of maximum co-seismic slip and at the southeastern margin of the Peninsula (clusters C1 and C2 in Fig. 2.4 and Fig. 2.5), is well explained by regions of static stress increase on the megathrust plane induced by the mainshock (Fig. 2.7). Little aftershock activity occurs down-dip, suggesting that the deep coseismic slip released almost all of the accumulated elastic strain in the deeper part of the seismogenic zone, leaving none sufficient to result in brittle failure. Nonetheless, about 20% of smaller magnitude underthrusting events are located in areas of transitions between positive and negative static stress changes or in region of reduced driving stress, suggesting that other mechanisms, such as dynamic perturbation of fluid conditions or post-seismic creep of the fault (Malservisi *et al.*, 2015) may be responsible for triggering some of the interplate earthquakes.

Figure. 2.7. Map view of the Coulomb Failure Stress (CFS) on the plate interface induced by the 2012, $M_w = 7.6$ Nicoya Peninsula, Costa Rica earthquake. The CFS was computed using the slip model of Liu *et al*. (2015) and the 3-hr afterslip model of Malservisi *et al*. (2015), assuming an optimal receiver fault with geometry (strike: 308; dip 17; slip vector 102). The hypocenter of the mainshock (green star) is located at 13 km depth. Circles locate underthrusting events identified by the selection criteria discussed in the text.

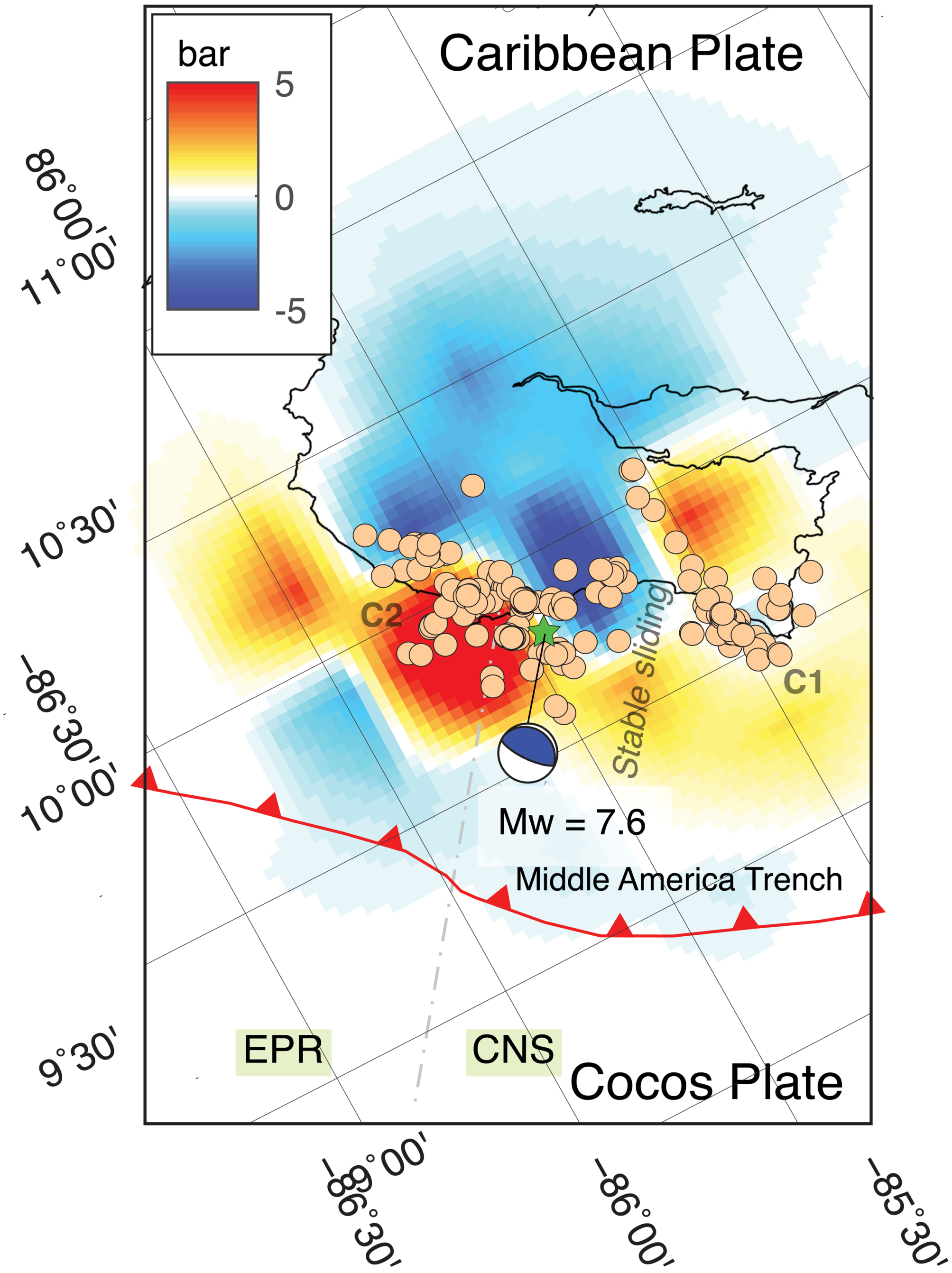
bar
5
0
-5
Caribbean Plate
86°00′
11°00′
10°30′
−86°30′
10°00′
9°30′
C2
C1
Stable sliding
Mw = 7.6
Middle America Trench
EPR
CNS
Cocos Plate
−86°30′
−86°00′
−86°00′
−85°30′

While it is not unexpected for a large percentage of aftershocks on the mainshock fault plane to locate in regions of calculated Coulomb stress increase (e.g., King *et al*., 1994), a more stringent test of the Coulomb stress triggering hypothesis is whether the fault planes of all aftershocks throughout the source region are suitably oriented for failure to have been promoted by the mainshock slip (consistent with the ΔCFS hypothesis). Resolving the Coulomb stress change on the nodal planes (rake directions) of aftershock sequences requires no assumptions about the regional stress field, but does depend on the mainshock source rupture model and the assumed coefficient of friction (King *et al*., 1994; Toda *et al*; 2011a, b). While shear stresses are similar for both nodal planes, the normal stress is different (Hardebeck *et al*., 1998), and thus, ΔCFS varies for the orthogonal planes.

We tested the Coulomb static stress triggering hypothesis on just the interface-aligned nodal plane for the catalog of underthrusting aftershock focal mechanisms (Table B-1) and on both nodal planes for the remaining events (Fig. 2.8). We examined the effect of the friction coefficient using four values (0.2, 0.4, 0.6 and 0.8), and found that 0.4 is the value that produces the greatest number of events with positive Coulomb static stress change, as has been observed in previous studies (Toda *et al*., 2011a). Figure 2.8B shows the distribution of events with positive and negative ΔCFS as a function of friction coefficient. For a friction coefficient of 0.4 we found that 80% of the aftershocks experience positive Coulomb stress change that would promote its failure and 20% of the aftershocks show negative Coulomb stress change that would inhibit their failure. In some regions, variable mechanisms with both positive and negative Coulomb stress changes are spatially intermingled. Similar analyses (Hardebeck *et al*., 1998; Sato *et al*., 2013; Sumy *et al*., 2014; Zhu and Miao, 2015) have shown that focal mechanisms with both, positive and negative Coulomb static stress changes are spatially intermingled even though nearby aftershocks may have quite similar fault geometries. Thus, while many of the focal mechanisms exhibit similar geometry to that of the mainshock, small rotations in the receiver fault geometry and/or uncertainties in the co-seismic and after-slip models can significantly affect the Coulomb stress calculation.

Figure 2.9 shows the location of underthrusting aftershocks with positive and negative Coulomb stress changes together with the 70 day afterslip distribution (Malservisi *et al*., 2015). Most of the aftershocks occur in regions of enhanced afterslip (at least 0.3 m). Therefore, the distribution of underthrusting aftershocks can be explained by either the static stress change induced by the mainshock or by accelerated fault creep during afterslip, or both. Of course, there are many uncertainties in the mainshock slip distribution, the precise megathrust geometry, the faulting mechanisms of the aftershocks, the locations of the aftershocks, and no specific knowledge of pre-stress in the region prior to the mainshock (Feng *et al*., 2012), so we do not want to overinterpret the 80% consistency found here other than as a compatibility result for reasonable elastic stress transfer effects.

Figure. 2.8. A) The Coulomb static stress change computed on the nodal planes of the entire catalog of aftershocks analyzed in this study. Positive circles (80%) are events with mechanisms where one or both nodal planes correspond positively with the Coulomb static stress hypothesis. Negative circles (20%) represent seismicity that is not triggered by the Coulomb static stress change induced by the mainshock (neither nodal plane is favored for failure). B) Histograms showing the distribution of positive and negative CFS on the nodal plane of the aftershocks as a function of friction coefficient.

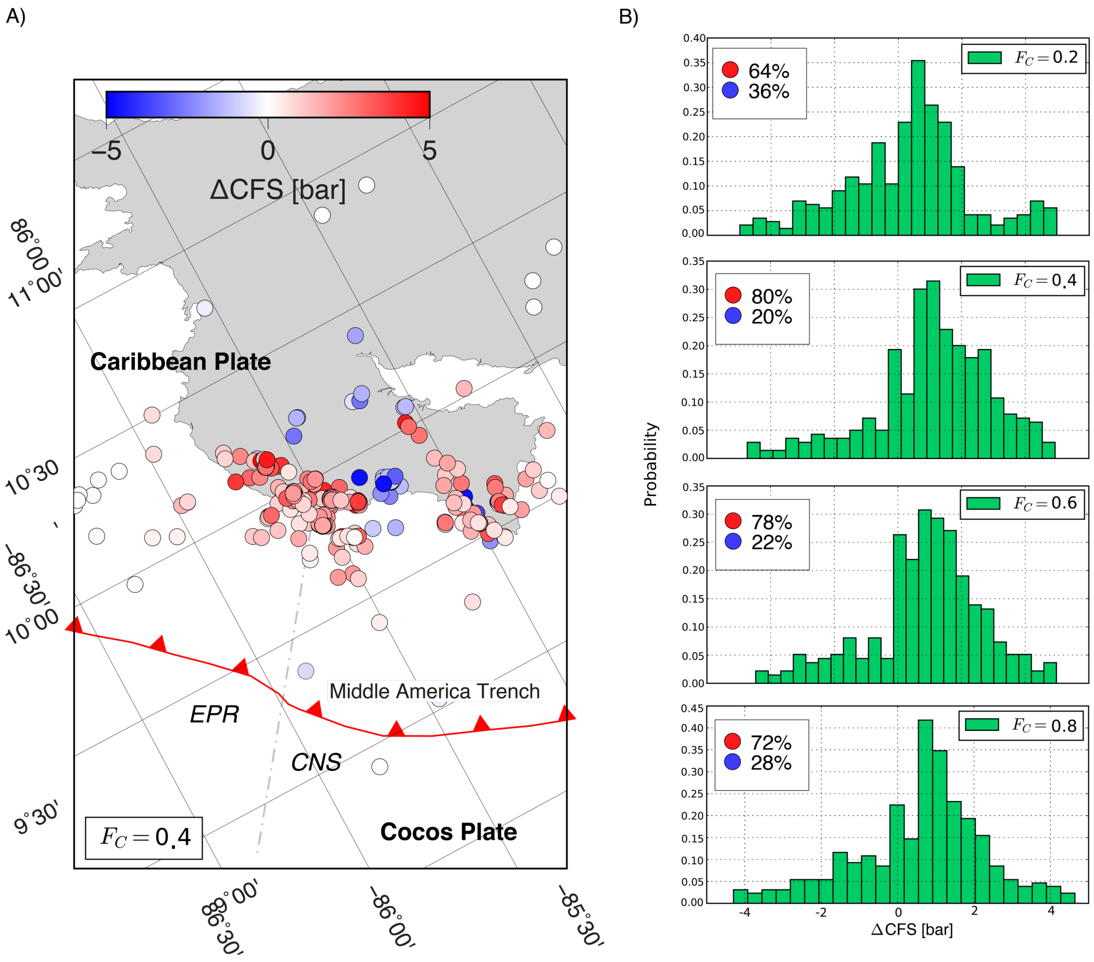
A)
B)
−5
0
5
ΔCFS [bar]
86°00'
11°00'
10°30'
−86°30'
10°00'
9°30'
86°30'
86°00'
−86°00'
−85°30'
Caribbean Plate
Middle America Trench
EPR
CNS
Cocos Plate
$F_C = 0.4$
Probability
64%
36%
$F_C = 0.2$
80%
20%
$F_C = 0.4$
78%
22%
$F_C = 0.6$
72%
28%
$F_C = 0.8$
ΔCFS [bar]
-4
-2
0
2
4

Most of the observations bearing on the mechanical behavior of the plate interface are summarized in Fig. 2.9. We infer that the region accumulating strain prior to the Nicoya mainshock (dark contour) spanned the entire seismogenic zone (~10-32 km in depth) and experienced the maximum co-seismic slip or afterslip, in the down-dip and up-dip parts of the locked patch, respectively. The large majority of the underthrusting aftershocks (circles) occurred up-dip of maximum co-seismic slip in regions of large afterslip. Portions of the plate interface that failed in slow slip locate both up and down-dip of the seismogenic zone. While no aftershocks occur in the slow slip regions, some mainshock slip likely extended into these zones.

2.5. CONCLUSIONS

We examine the aftershock sequence of the 5 September 2012 M_W 7.6 Nicoya Peninsula, Costa Rica earthquake in terms of hypocenter locations and fault geometries. Focal mechanisms for the larger magnitude events are generated using full waveform moment tensor inversions. We use *P*-wave first motion polarities to determine the faulting geometries of the smaller magnitude earthquakes. Coulomb static stress changes on the plate interface and on the nodal planes of the aftershocks induced by the mainshock slip and first three days of afterslip are computed and compared with the spatial distribution of afterslip.

We find that underthrusting aftershocks span the depth range 12 to 32 km but are concentrated up dip, adjacent to the main co-seismic slip and at the southernmost edge of the Nicoya Peninsula, defining two discrete patches that are separated by a conspicuous gap in aftershock activity. This gap might be due to the lack of coseismic slip in this region or represent an along strike variation in the frictional behavior of the plate interface that relates to the morphology of the subducted slab. Interface seismicity during the interseismic cycle is constrained to shallower depths on the plate interface (12-25 km). The co-seismic slip extends several kilometers up and down-dip of the interplate aftershocks into regions of the plate interface that exhibit slow slip.

This pattern suggests that the mainshock ruptured a strongly locked patch driving downdip slip into a normally velocity strengthening part of the deep plate interface that hosts slow slip events. Our observations suggest that large earthquakes can rupture into areas that may normally be aseismic, indicating conditionally stable frictional behavior. A total of ~20% of the underthrusting aftershocks are located in regions that are unsuitable for failure induced by the mainshock slip and the 3-hr afterslip (correlate negatively with the Coulomb static stress triggering hypothesis). The locations of these events do agree well with the 70-day afterslip pattern, indicating that the aftershock distribution can be explained by a combination of afterslip and static stress changes following the mainshock. It is likely that these are related with afterslip being the response of the plate interface away from the main stick-slip asperity to the increased static stress resulting from co-seismic slip with aftershocks being local responses to this afterslip.

Figure. 2.9. Map showing afterslip associated with the intermediate relaxation time (70 days) documented in Malservisi *et al.* (2015). Light contours represents the coseismic slip area of the 2012, M_W 7.6 Nicoya mainshock from Liu *et al.* (2015), the dark contour outlines the region of strain accumulation from Feng *et al.*, (2012). The cumulative slip of 1 m from SSEs is represented by the up-dip and down-dip magenta curves (Dixon *et al.*, 2014). Circles represent aftershocks located along the plate interface. 80% of the underthrusting events correspond positively with the Coulomb static stress change induced by the occurrence of the Nicoya Peninsula earthquake, assuming the interplate fault plane choice. These events all locate within regions of intermediate to high afterslip.

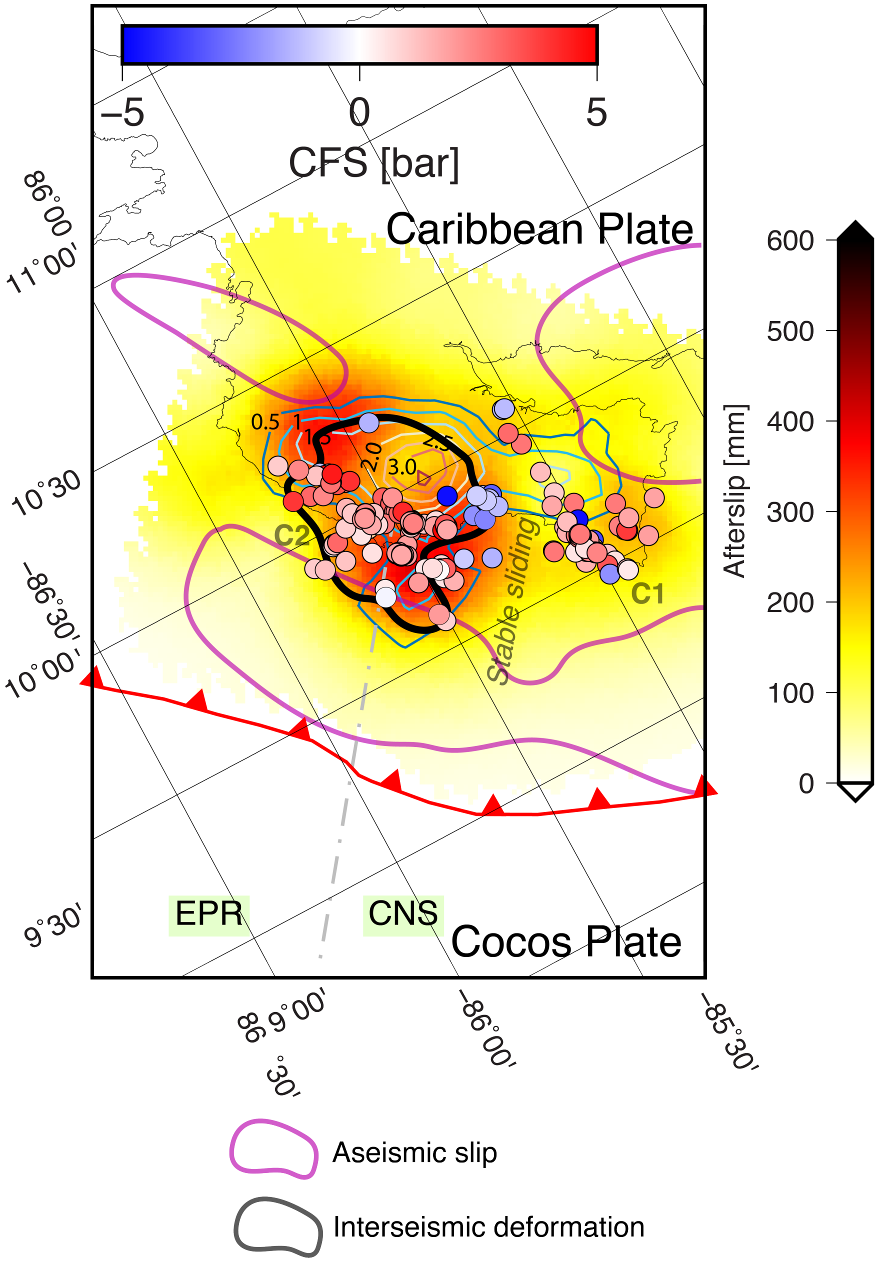

−5
0
5
CFS [bar]
Caribbean Plate
Cocos Plate
EPR
CNS
C1
C2
Stable sliding
0.5
1
1.5
2.0
2.5
3.0
86°00′
11°00′
10°30
−86°30′
10°00′
9°30′
9°00′
−86°30′
−86°00′
−85°30′
Afterslip [mm]
600
500
400
300
200
100
0
Aseismic slip
Interseismic deformation

CHAPTER 3 - FAULT STRENGTH VARIABILITY DURING THE EARTHQUAKE CYCLE ALONG THE NICOYA PENINSULA MEGATHRUST

Abstract. The recurrence interval and rupture characteristics of earthquakes, including stress drop, are controlled by the frictional strength and mechanical properties of the fault. Evaluating fault strength variability during the earthquake cycle is critical for understanding earthquake processes and the physics of fault zones. Using repeating earthquakes, events with similar waveforms and locations, we provide unique observations of a reduction in yield strength on repeating earthquake fault patches after the 5 September 2012, M7.6 Nicoya Peninsula Costa Rica megathrust earthquake, followed by fault strength recovery. We analyze the temporal evolution of earthquake source spectra, and derived stress drop, for 5 repeating earthquake families with magnitudes between M2.5 and M3.3 that reoccur from 2-6 times between 2007 and 2017. Each of the 17 individual repeating events occur as the largest earthquake in a temporally clustered group of events possessing identical waveforms but varying magnitudes (from 1.5 and 3.3) and recurrence intervals (from hours to weeks). We refer to these groups as repeating earthquake clusters (REC) and the largest event within each cluster as a target event. Source spectra for target events are obtained using the empirical Green's function (EGF) approach, taking advantage of the numerous EGFs in a cluster that are available for each target event. Our results indicate that repeating target events are magnitude invariant but experience a reduction in stress drop after the

Nicoya earthquake followed by a systematic increase through 2016, when all repeaters cease. The recurrence interval of all but 1 of the repeating families decreases following the Nicoya mainshock. We ascribe the observed reduction in stress drop to frictional weakening of the megathrust (reduction of the static coefficient of friction) caused by fault zone damage. A lowered yield strength allows repeaters driven by steady aseismic creep to occur more frequently. Fluid release during the earthquake, increasing pore fluid pressure and decreasing the effective normal stress, might also contribute to frictional weakening. Time-dependent re-strengthening of fault patches suggests that the plate interface heals within ~1.5 years after the large event, a time scale that is consistent with previous observations of hydrologic property and seismic velocity changes in postseismic fault zones.

3.1. INTRODUCTION

Earthquake stress drop, strong ground shaking, recurrence interval and the rupture characteristics of large and great earthquakes are controlled by fault strength (the fault resistance to shear stress before it slips) and the frictional properties of the plate interface [e.g. Marone, 1998; Zielke et al., 2017]. Monitoring the fault strength and its variability (e.g. fault weakening and fault re-strengthening or frictional healing) during the earthquake cycle is critical for earthquake hazard assessment. The increasing quantity and resolution of seismological and geodetic data has provided an incredible opportunity for monitoring and understanding earthquake processes along faults. Subduction zones in particular produce the largest and potentially most catastrophic earthquakes and tsunami around the world. Multiple studies have been conducted in this environment to better understand how these events propagate and affect the adjacent off-fault areas, as well as to characterize the mechanical properties (e.g. crustal rheology, roughness, frictional behavior, etc.) of the asperities where these events nucleate [Lay, 2012].

Recent observations have demonstrated the heterogeneous frictional slip behaviors of faults along convergent margins, showing them to host a diverse range of events that include small and intermediate magnitude earthquakes ($M \leq 6.5$), megathrust and tsunami earthquakes ($M \geq 7.0$), low-frequency earthquakes (LFEs), very low-frequency earthquakes (VLFEs), tectonic tremor and slow slip events (SSEs) [e.g. Schwartz and Rokosky, 2007]. 3D images of megathrust regions also provide an unprecedented look into the geometrical complexity exhibited along these margins, where topographic corrugations and seamount subduction play a key role in promoting or/and halting seismic and aseismic activity and affecting fault strength [Edwards et al., 2018]. Studying source parameters (e.g. stress drop, $\Delta\sigma$) of small magnitude earthquakes enables a better understanding of fault physics (e.g. the long term evolution and dynamic rupture propagation) and the variability of the frictional properties of the plate interface during the earthquake cycle.

Because of the advantageous location of the Nicoya Peninsula, northern Costa Rica, extending seaward over the seismogenic zone and the existence of a regional seismic and continuous Global Positioning System (GPS) network that has recorded megathrust activity with outstanding detail over the last decade, it is an ideal locality to study earthquake source processes (Figure 3.1). The relatively rapid subduction (~85 mm/yr) of the Cocos plate underneath the Caribbean Plate along the Nicoya Peninsula [DeMets et al., 2010], has generated M7+ earthquakes every 50 years, with the last one of these events, a moment magnitude (Mw) 7.6 earthquake, occurring on 5 September 2012 [Protti et al., 2013]. Tectonic tremor and SSEs have been recorded every ~ 2 years or less since 2003, with both located along the up-dip and down-dip edges of the seismically active plate interface [Walter et al., 2011; Dixon et al., 2014; Voss et al., 2017].

In this study we use repeating earthquakes, recurring events with similar waveforms and locations, to track the temporal evolution of earthquake source spectra, and derived stress drop at the same locations through the earthquake cycle. We find a reduction in the stress drop of several repeating earthquake clusters after the 2012 Nicoya earthquake that recover within 2 years of the mainshock. We interpret this as frictional weakening of the megathrust caused by fault zone damage followed by fault healing.

Figure 3.1. Tectonic setting and the spatial distribution of the Nicoya Seismic Cycle Observatory and Volcanological and Seismological Observatory of Costa Rica (OVSICORI-UNA) seismic stations used in this study (Orange triangles). The color contours illustrate the co-seismic slip area of the 5 September 2012, M_W=7.6, Nicoya Peninsula earthquake (slip increments of 0.5 m; Liu et al., 2015). The yellow regions up-dip and down-dip of the plate interface highlight the accumulated slow slip (in millimeters) between 2007 and 2017 (Dixon et al., 2014; Voss et al., 2017). The dashed black line represents the East Pacific Rise (EPR)–Cocos Nazca Spreading center (CNS) boundary (Barckhausen et al., 2001). Stars show the epicentral location of the repeating earthquake clusters analyzed in this study color coded by cluster id. Focal mechanism corresponds with the fault geometry and epicentral location of the Nicoya Peninsula earthquake.

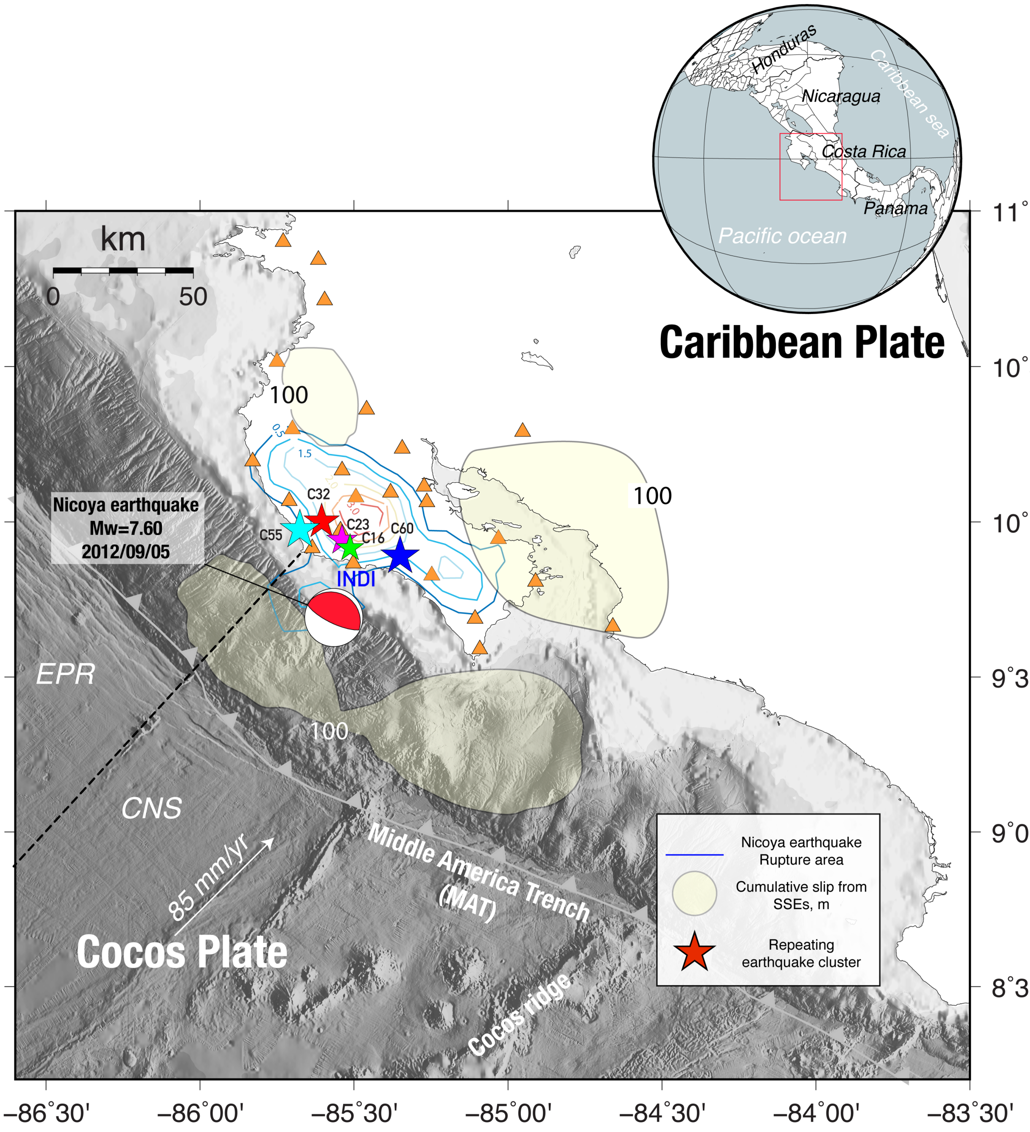
Honduras
Nicaragua
Caribbean sea
Costa Rica
Panama
Pacific ocean
Caribbean Plate
km
0
50
100
100
100
Nicoya earthquake
Mw=7.60
2012/09/05
C32
C55
C23
C16
C60
INDI
EPR
CNS
85 mm/yr
Cocos Plate
Middle America Trench
(MAT)
Cocos ridge
Nicoya earthquake Rupture area
Cumulative slip from SSEs, m
Repeating earthquake cluster
11˚00'
10˚30'
10˚00'
9˚30'
9˚00'
8˚30'
−86˚30'
−86˚00'
−85˚30'
−85˚00'
−84˚30'
−84˚00'
−83˚30'

3.2. REPEATING EARTHQUAKES

Repeating earthquakes with nearly identical waveforms, magnitudes and locations, have been observed at plate boundaries and thought to represent the rupture of the same fault asperity at a relatively constant repeat interval due to continuous loading by surrounding aseismic slip [Nadeau and Johnson, 1998; Igarashi et al., 2003]. Repeating earthquakes recurring frequently over a short period of time, with brief and irregular recurrence intervals have been identified in aftershock sequences of large earthquakes [Igarashi et al, 2003; Kimura et al., 2006] and inferred to be caused by accelerated aseismic slip following mainshocks (afterslip) driving asperity failure. Because these events repeatedly rupture the same fault patch as a function of time, they are ideal to investigate temporal variations in source parameters through the earthquake cycle.

Small magnitude repeating events have been previously recognized and studied in the laboratory [e.g. Chen and Lapusta, 2009; Chen et al., 2010] and in natural fault systems along the San Andreas fault in California [e.g. Marone et al., 1995; Peng et al., 2005; Allman and Shearer, 2007; Dreger et al., 2007; Abercrombie, 2014], Japan [e.g. Igarashi et al., 2003; Uchida et al., 2007; Uchida et al., 2012; Hatakeyama et al., 2017] and Mexico [Dominguez et al., 2016], and used to estimate the spatiotemporal distribution of aseismic slip during slow slip and/or afterslip episodes as well as to study earthquake interactions [e.g. Vidale et al., 1994; Nadeau and Johnson, 1998; Lui and Lapusta, 2016]. However, few studies have shown clear variations in source properties, in particular static stress drop of small repeating earthquakes that may help to elucidate natural fault strength variability before and after large crustal earthquakes [e.g. Marone et al., 1995; Marone et al., 1998, Abercrombie, 2014]. Previous work based on variations in the seismic moment of repeating earthquakes indicates that $\Delta\sigma$ generally increases by a few megapascals per decade increase in recurrence interval [e.g. Marone, 1998; Marone and Saffer, 2015], however such observations are complex, since variability in failure strength depends on coupled effects between loading rate (or strain rate), frictional state, and the asperity-effective area of contact or elastic coupling.

Yao et al. (2017) used waveform matching to increase the number of events in the foreshock/aftershock catalog of the 5 September, 2012 Mw 7.6 Nicoya earthquake. They found 53 repeating earthquake clusters between July and December 2012 that mostly locate in areas of modeled afterslip. We selected repeating earthquakes from their catalog supplemented by additional aftershocks [Chaves et al, 2017] and used a similar waveform matching technique to greatly extend the time period of repeating earthquakes from 2007 through 2018. We identified 5 repeating earthquake families that each consist of: large or target events (magnitudes between M2.5-M3.3) that repeat with a nearly constant magnitude between 2 to 6 times during the twelve years analyzed, and several smaller events (at least one order of magnitude smaller than the largest event) with nearly identical waveforms to the large event that cluster around it in time. Figures 3.1 and 3.2 show the spatial and temporal distribution of these families labeled C60, C55, C32 C23 and C16, maintaining the nomenclature from Yao et al. [2017].

All repeating earthquake families locate along the up-dip margin of the rupture zone of the 2012 Nicoya Peninsula earthquake, at the frictional transition between unstable sliding (seismic) downdip, to conditionally stable sliding (hosting slow slip), up-dip (Figure 3.1). This region also experienced maximum early post-seismic slip (Figure 3.2f) [Malservisi et al., 2015] and positive Coulomb static stress changes [Chaves et al., 2017] following the Nicoya mainshock. Three of the five earthquake families (C32, C23, and C16) had no activity for at least 5 years prior to the 2012 mainshock followed by target events that repeated 2-3 times in the subsequent 3 years. (Figure 3.2). One repeating family occurred once about 4 years before the mainshock and twice in the following 4 years. Assuming that the interseismic recurrence interval for families C32, C23 and C16 is longer than five years (the time span of pre-mainshock data), the repeat time of the target events in these families decreases following the Nicoya mainshock. We observe no change in the recurrence interval of the target event for the most active family, C60.

Figure 3.2. Temporal distribution of the repeating earthquake families analyzed in this study and shown in Figure 1. Panels (a)-(e) show the magnitude distribution with respect to the time of occurrence of the 5 September 2012, M7.6, Nicoya Peninsula earthquake (red dashed line). Repeating Earthquake Clusters (RECs) for each family are formed by a target event (stars) and several smaller magnitude events or EGFs (circles). The white star shown in panel a) identifies an event with complex spectra (VR < 85%) that was removed from further analysis. Panel f) shows the spatial distribution of the REC with respect to the short term afterslip, indicated by the white contour lines [Malservisi et al., 2015] and the long term afterslip of the Nicoya earthquake [Hobbs et al., 2017], indicated by the colored map. The amount of slip for both the short and long term afterslip is indicated in meters. Note the spatial decorrelation between the areas of maximum long-term afterlslip and the location of the repeating families.

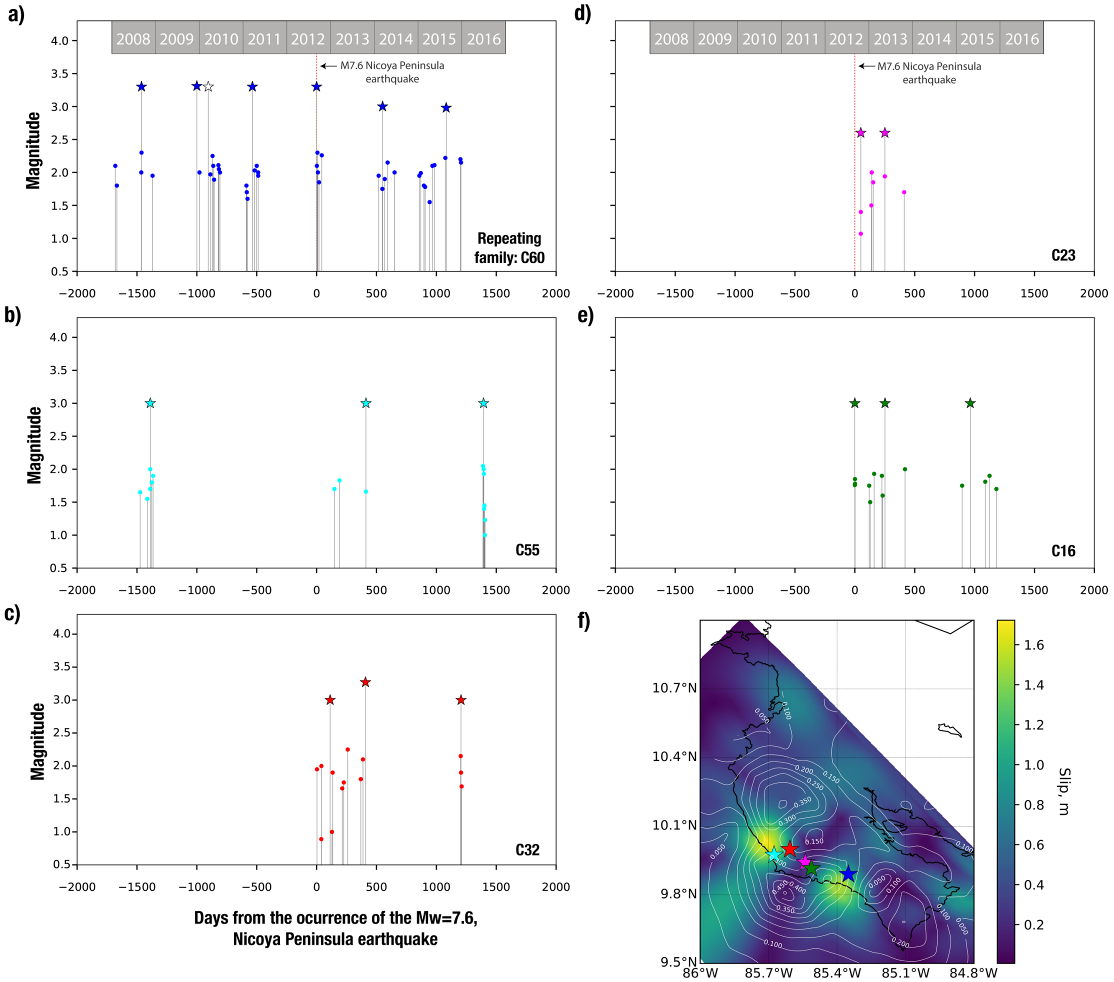a)
b)
c)
d)
e)
f)
2008 2009 2010 2011 2012 2013 2014 2015 2016
M7.6 Nicoya Peninsula earthquake
Magnitude
Repeating family: C60
C55
C32
C23
C16
Days from the ocurrence of the Mw=7.6, Nicoya Peninsula earthquake
4.0
3.5
3.0
2.5
2.0
1.5
1.0
0.5
−2000 −1500 −1000 −500 0 500 1000 1500 2000
10.7°N
10.4°N
10.1°N
9.8°N
9.5°N
86°W 85.7°W 85.4°W 85.1°W 84.8°W
Slip, m
1.6
1.4
1.2
1.0
0.8
0.6
0.4
0.2

3.3. STRESS DROP VARIABILITY

We analyze the temporal evolution of earthquake source spectra, and derived stress drop from the corner frequency and seismic moment of the target event in each recurring earthquake cluster (REC) for the five families. Given the waveform similarity across the seismic network, indicative of identical focal mechanism and hypocenter location, as well as their magnitude distribution with respect to the corresponding target event (at least one order of magnitude smaller than the largest event), we considered all small magnitude repeating events in a REC as empirical Green's functions, or EGFs (circles in figure 2a-e). Source spectra for target events are obtained using the empirical Green's function approach, taking advantage of the numerous EGFs in a cluster that are available for each target event. An example of the waveform deconvolution procedure is shown in the supplementary figure C-1 and described in the methods section.

It is important to note that we avoid using EGFs that occur more than a few months before or after the target events to isolate temporal changes in the physical properties of the recurrent fault patches and the evolution of the yield strength of the fault zone without introducing possible time variations in propagation properties of the medium. We evaluate the complexity of the spectral ratio based on its fit to a Boatwright source model. Contrary to most previous work, where complexity of the spectral ratio for small magnitude earthquakes is ignored, we eliminate complex events from further analysis. We find that only one target event in 2009 which is part of cluster C60, exhibits complexity (variance reduction < 85%) that cannot be accounted for using simple rupture models (white star in Figure 3.2a) requiring elimination from further consideration.

Measurements of $\Delta\sigma$ as a function of time from only the “simple spectra” for each of the REC are shown in Figure 3.3. Our results indicate that target events experience a reduction in stress drop after the Nicoya earthquake followed by a systematic increase through 2016 when all repeaters cease. Although target event magnitudes remain invariant throughout the time period of this study, we observe a significant increase in high frequency content with recurrence interval in the spectral ratios of the target events. Figure 3.4 compares the earthquake source spectra and time function between the megathrust-affected target event (color blue) in 2012 and the healed target event (color green) in 2015 for three of the repeating families (C16, C60 and C32), demonstrating that the latter is enhanced in high frequencies. Healed repeating events present more power than the megathrust-affected events at frequencies between 6-18 Hz, with a significant increase (almost double) in earthquake corner frequency, indicated with circles for both events. Similar differences can also be observed in the spectral content of the raw P-wave records of both target events (Figure C-2).

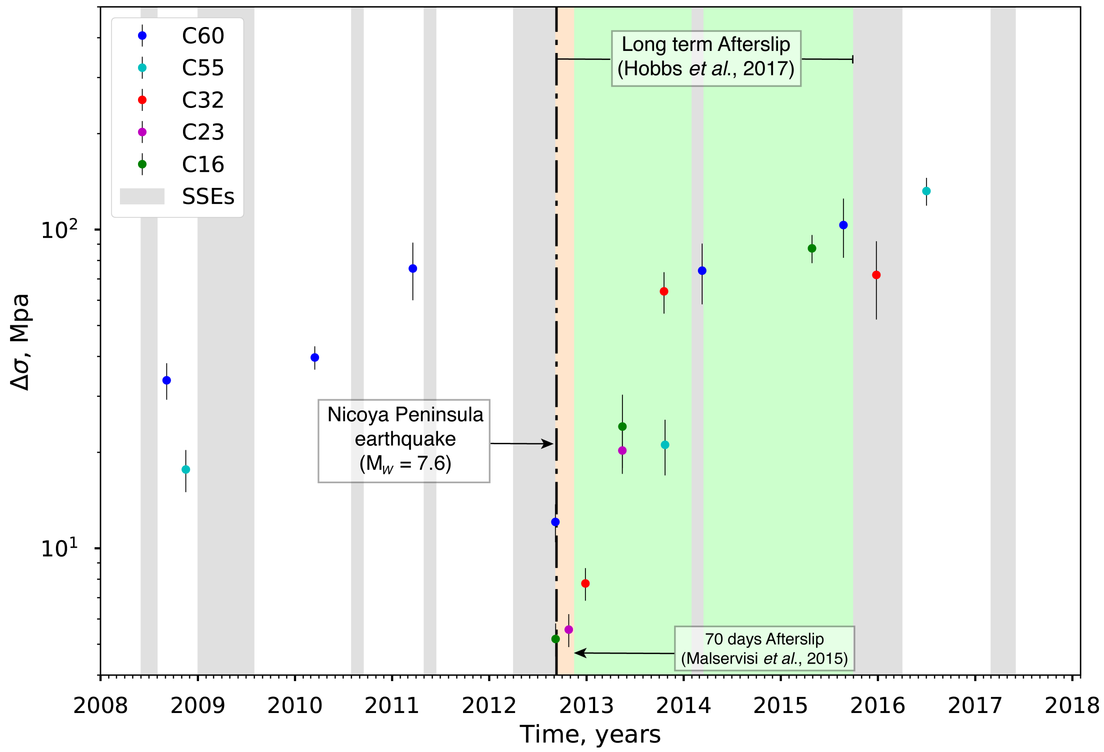

Figure 3.3. Static stress drop variability as a function of time with respect to the occurrence of the 5 September 2012, Mw=7.6, Nicoya Peninsula earthquake (black dashed line). Circles represent the repeating earthquakes clusters color coded by cluster id (see supplement information for calculation of error bars). The grey bars mark periods of slow slip events from 2008 through 2017 (Dixon et al., 2014; Voss et al., 2017) and the orange and green regions indicate the duration of the short term and long term Nicoya earthquake afterslip (Malservisi et al., 2015; Hobbs et al., 2017). Note that no repeaters were identified after 2016.

3.4 METHODS

3.4.1. REPEATING EARTHQUAKES

Using EQcorrscan [Chamberlain et al., 2018], a template-matching detection algorithm in Python, we extended the July through December 2012 catalog of repeating earthquake clusters generated for the aftershock sequence of the 5 September 2012, $M_W = 7.6$, Nicoya Peninsula earthquake [Yao et al., 2017] to cover a period of about 11 years. Starting with 53 well-located repeating clusters in this catalog, we selected those that contained events with at least one order of magnitude difference in earthquake size, reducing the catalog to 26 clusters. For each repeating cluster, we selected the largest magnitude event (M2.2 – M3.30, termed target event) as a template to scan through continuous seismic data from 2007 until March 2018 to find matches.

For computing the waveform cross-correlation, we used the vertical component of all the stations from the Nicoya Seismic Cycle Observatory (Figure. 1) available during each year. We applied a 1-15 Hz Butterworth bandpass filter to the data and used 0.5 s before and 4.5 s after (a total of 5.0 s window) the manually picked P-wave arrival. All events with a network averaged cross-correlation coefficient, $CC \geq 0.93$ were considered repeaters, $CC \geq 0.85$ were considered near repeaters. In total, we identified five earthquake clusters whose target events repeat at least twice between 2008 and 2016. Figures 1 and 2 show the spatial and temporal distribution of the earthquake clusters C60, C55, C32 C23 and C16. Each of these clusters is formed by a target event (represented by stars in Figure 2) whose magnitude is constant or nearly constant with time and a minimum of 3 smaller events (at least one order of magnitude smaller than the largest event) that obey our definition of repeating or near-repeating events.

3.4.2. CORNER FREQUENCY DETERMINATION

We analyzed temporal changes in the corner frequency and stress drop of all target events in these repeating earthquake clusters. We compute corner frequencies using the empirical Green's function, eGF, spectral ratio approach [Abercrombie, 2013, 2014, 2015 and 2017], summarized here. We classified the largest event of each repeating sequence as the target or main event and the smaller magnitude earthquakes within that REC as empirical Green's functions. Each eGF-target waveform pair is windowed using an empirical magnitude-dependent duration, that is of the order of 10 times the expected pulse duration of the target earthquake, assuming a constant stress drop scaling [Abercrombie et al., 2017].

Where M_O is the seismic moment of the main earthquake. Local magnitudes previously determined for the aftershock sequence of the Nicoya Peninsula earthquake [Yao et al., 2017] are used for computing the M_O for events that occurred in 2012. We used the Singular Value Decomposition (SVD) approach [Rubinstein and Ellsworth, 2010], to compute relative moments for all the repeating events that occur in other years. This method takes advantage of the highly coherent waveforms of repeating earthquakes and yields more precise and accurate descriptions of earthquake size than standard catalog techniques. For the SVD analysis we used the vertical component of all the seismic stations available for a given year that recorded the events. We low-pass filter seismograms with a Butterworth filter with a corner of 10 Hz to enhance the SNR. Signals are aligned using a cross-correlation on the P-wave. Due to the proximity of the stations to the earthquake source, we use a total window length of 4.5 s that begins 0.5 s before the P-wave arrival.

We calculate spectra and spectral ratios using a multitaper approach [Prieto et al., 2009] that uses complex division, enabling the calculation of the mainshock source time function (STF). Deconvolution of a clear source pulse confirms the eGF assumption, since the approximation is good enough to work in both, phase and amplitude. Time domain source functions or STFs are also useful for discriminating complex earthquakes that cannot be fully described by a simple source model (Figure C-1). We fit each individual spectral ratio to calculate corner frequencies using the spectral source model [Brune, 1970; Boatwright, 1980]:

$$\frac{\dot{M}_1(f)}{\dot{M}_2(f)} = \frac{M_{01}}{M_{02}}\left[\frac{1 + (f/f_{c2})^{\gamma n}}{1 + (f/f_{c1})^{\gamma n}}\right]^{\frac{1}{\gamma}} \tag{3.1}$$

Where f is frequency, f_{c1} and f_{c2} are the corner frequencies of the target and the EGF, respectively, n is the frequency fall off (here, we assume $n = 2$), and γ is a constant controlling the shape of the corner. M_{01} and M_{02} correspond with the seismic moment of the target and the eGF respectively. We try fitting the observed spectral ratio to the original Brune model ($\gamma = 1$) and a sharper corner or Boatwright model ($\gamma = 2$) and observed that overall the shaper corner provided better fit to the majority of the spectral ratios analyzed. Before fitting, we log-sample the individual spectral ratios resulting from the deconvolution of each EGF-target earthquake pair for each station in the frequency domain to reduce the weighting towards the higher frequency part of the spectra.

We use a $log_{10}(\Delta f)$ sample rate of 0.05 and finally select the frequency range where the signal, defined by the P-wave train, with length *nsec (1)*, is at least 3 times the noise, defined by the pre P-wave arrival with the same length of the signal. We average the resulting individual spectral ratios and STFs to obtain the mainshock spectrum and STF. Averaging across multiple azimuths improve stability and resolution of the corner frequencies and reduces the possibility of underestimating or overestimating the mainshock source duration ($1/f_{c1}$) due to possible finiteness effects of the source (e.g. earthquake directivity). We fit the average source spectrum using the Levenberg-Marquardt algoritm in LMFIT (https://lmfit.github.io/lmfit-py/) a Python, open source, library for non-linear curve fitting, and perform a gridsearch around the resulting value of f_{c1}, to determine the range of f_{c1} and f_{c2} in which the fit between the data and the model given by the variance reduction (VR) is at least 85%:

$$VR = \left[1 - \frac{\sqrt{(data - model)^2}}{\sqrt{(data)^2}}\right] \times 100 \tag{3.2}$$

The gridsearch limits around the f_{c1} are defined as $2 \times F$, where F (F-test) represents the confidence interval (uncertainty) and it is defined as:

$$F(P_{fix}, N - P) = \left(\frac{\chi_f^2}{\chi_0^2} - 1\right) \times \frac{N - P}{P_{fix}} \tag{3.3}$$

Where χ_0 is the null model (which is the best fit we have found), χ_f is an alternate model where one of the parameters is fixed to an specific value, N is the number of data points, P is the number of parameters of the null model and P_{fix} is the number of fixed parameters. To limit the effects of complexities in the source spectra we use only measurements where the difference in amplitude of the high and low frequency levels in the fit is greater than 2. We do not use estimates of f_{c2} since for some cases, they are typically out of the available bandwidth.

3.4.3. STRESS DROP DETERMINATION

To calculate stress drop ($\Delta\sigma$) from the previously determined seismic moment and corner frequency measurements, we assume a simple circular model [Eshelby, 1957]:

$$\Delta\sigma = \frac{7}{16}\frac{M_o\, f_c^3}{k^3\, \beta^3} \tag{3.4}$$

Where M_O is the seismic moment, β is the shear wave velocity (β = ~3.5 km/s) and k is a constant equal to 0.32 for P-waves [Madariaga, 1976].

3.5. RESULTS AND DISCUSSION

A physical interpretation of stress drop is given by:

$$\Delta\sigma = (f_s - f_k) \cdot \sigma_n^{eff} \tag{3.5}$$

Where f_s and f_k correspond to the static and dynamic coefficients of friction respectively and σ_n^{eff} is the effective normal stress. Laboratory measurements and numerical simulations of earthquakes have demonstrated that the frictional strength and thus $\Delta\sigma$ of faults, respond to changes in slip rate. At low interseismic slip rates, rock friction experiments show minor variations in the static coefficient of friction and thus frictional strength. In contrast, strong frictional weakening (a reduction in f_s) is observed after faster slip rates, such as those during an earthquake-generated fault rupture [e.g. Marone, 1998; Marone et al., 2015].

Furthermore, because earthquakes promote fractures in a damage zone around the fault, it is expected that after large events fault permeability will vary transiently [e.g. Xue et al., 2013; Yoshida et al., 2017]. Strong seismic velocity reductions (~0.6%) were observed following the 2012 Nicoya Peninsula earthquake at depths between 5-15 km, in regions were a previous receiver function study found extremely high forearch V_p/V_s ratios that were interpreted as pore fluid overpressures [Audet and Schwartz, 2013]. The seismic velocity change that followed this large earthquake was attributed to an increase in fracture density caused by overpressured fluids reducing the effective stress and weakening the crust, making it more susceptible to damage from dynamic stresses [Chaves and Schwartz, 2016]. The breaking of low permeability seals during the mainshock rupture can increase both fracture density and fault zone permeability in particular locations, resulting in fluid migration and an increase in pore fluid pressure and decreasing σ_n^{eff} in adjacent regions. This suggests that coseismic fluid release and migration may have important effects on the frictional strength of the plate interface.

Although multiple weakening mechanisms may operate on the fault zone, recent seismological observations have shown that the reduction of σ_n^{eff}, by thermal pressurization of pore fluids due to shear heating of fault gauge and the reduction of the coefficient of static friction, f_s, by localized flash heating of asperity contacts in the gouge, are among the most likely to be ubiquitous across multiple earthquake sizes and tectonic environments [Rice, 2006; Raehee, et al., 2007; Di Toro et al., 2011; Viesca and Garagash, 2015]. We ascribe the observed reduction in stress drop of the RECs to frictional weakening of the megathrust region (reduction of the static coefficient of friction, f_s) caused by fault zone damage. Fluid release during the earthquake, increasing pore fluid pressure and decreasing the effective normal stress, might also contribute to frictional weakening of the plate interface.

Our interpretation of a reduction in the static coefficient of friction or the yield strength of the fault following the Nicoya mainshock is consistent with the concurrent reduction in recurrence interval (Figure 3.2). A weakened fault allows repeaters driven by surrounding steady aseismic creep to occur more frequently, since less accrued stress is required before seismic failure. Similar observations were reported in Parkfield, California after the 2004, M6 Parkfield earthquake [Dreger et al., 2007; Abercrombie, 2014] and off Kamaishi, Japan, following the 2011, M9.2 Tohoku-Oki earthquake [e.g. Uchida et al., 2007; Uchida et al., 2015], demonstrating that repeating sequences rupture more frequently after large crustal events. In these studies, the first events occurring after the mainshock exhibit a significant increase in seismic magnitude (~1 magnitude unit increase), or M_o, and return to their lower pre-earthquake values with time.

Since M_o scales with rupture area and average slip on the fault, an observed increase in magnitude must be caused by either an increase in the rupture area or the amount of slip, or a combination of both processes. Although the physics behind the observations is not well understood, it has been proposed that this seismic moment variability is plausibly linked to transient embrittlement, an aseismic-to-seismic transition in frictional properties of the fault region, controlled by high strain rates during the post-seismic slip that occurs after the mainshock [Peng et al., 2005; Uchida et al., 2015]. After the 2011 Tohoku, Japan earthquake, never before observed M6 repeating earthquakes emerged and eventually disappeared adjacent to the region of coseismic slip [Hatakeyama et al., 2017]. This observation supports the interpretation that the increased loading rate of afterslip caused a transition from velocity strengthening to velocity weakening frictional behavior, increasing the rupture area of small fault patches. As afterslip decayed, these small repeating earthquakes disappeared and the region returned to its previous aseismic behavior.

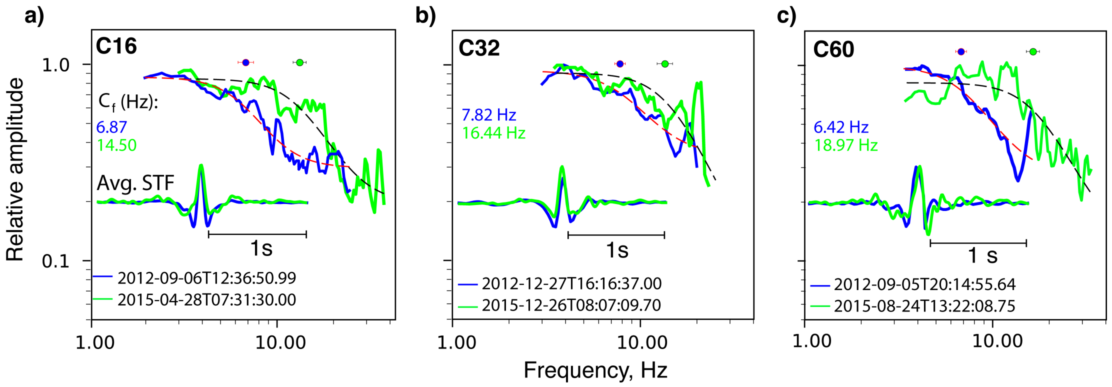

Figure 3.4. Earthquake source spectra and time function for three of the repeating earthquake families: a) C16, b) C32 and c) C60 obtained through the deconvolution procedure (Figure C-1). Each panel shows the comparison between the megathrust-affected target event (color blue) in 2012 and the healed target event (color green) in 2015. The red and black dashed line indicates the best-fit Boatwright model for each event and the circles correspond to the corner frequency for each event. Note that for the three families the healed (color green) event shows more power at frequencies between 6-18 Hz and its corner frequency is more than twice the corner frequency of the 2012 event.

In contrast to most of the previous observations in nature, our results indicate that repeating target events are magnitude invariant. Recent observations using continuous GPS stations along the Nicoya Peninsula, have shown that the up-dip regions of the plate interface that experienced the maximum long-term after slip following the 2012 Nicoya mainshock are spatially anticorrelated with the REC [Hobbs et al., 2017] (Figure. 3.2f), suggesting that transient strain rate variations caused by the long-term afterslip episode may have little to no effect on the repeating target events studied here. Furthermore, invariant seismic moment with recurrence interval after the

Nicoya Peninsula earthquake for all the RECs may indicate a reduction in the amount of slip during the repeated failure of the fault patches, possibly accompanied by increments in the effective area of contact during the frictional re-strengthening of the plate interface.

Further evidence that target event reduction in stress drop followed by recovery is due to changing properties on the plate interface (fault strength reduction) and not complex earthquake dynamics comes from comparison of EGF spectral properties. We observe the same temporal shifts in corner frequency in the small EGFs as we described for the spectral ratios of target events (Figure 3.4), confirming co-seismic fault damage as the most consistent explanation. We selected similar magnitude EGFs that occurred immediately after the Nicoya megathrust earthquake in 2012, and 3 years after this event to compare their waveforms and spectra. Figure 3.5 shows the time-frequency comparison between the mainshock-affected EGF (blue color) and the healed EGF that occurred in 2015 (green color) for clusters C16 and C32. Our results show that healed events present more power at higher frequencies (9-18 Hz), with a significant shift in the apparent corner frequency, indicated with triangles for both events. Our results are consistent with previous observations that used decorrelation of repeating events for constraining fault zone rheology changes after large crustal earthquakes [Taka'aki et al., 2008].

Albeit much progress has been made in developing friction constitutive laws to describe variations in frictional strength of faults with slip rate, time of contact, effective normal stress, temperature, etc., and its link to potential unstable sliding, frictional healing has received relatively less attention. Our results show that $\Delta\sigma$ increases logarithmically with recurrence interval after the 2012 Nicoya earthquake, suggestive of a renewal process in the fault zone of the RECs (Figure 3.3). We interpret this increase in $\Delta\sigma$ with time as the frictional healing of the repeatedly ruptured patches. Very few observations in nature have shown clearly how $\Delta\sigma$ or fault yield strength of repeating fault patches varies before and after a large slip instability. Following a very similar methodology to that used in this work, Abercrombie (2014) found that repeating earthquake clusters along the San Andreas fault in California, experienced a reduction in $\Delta\sigma$ right after the occurrence of the 2004 M6 Parkfield earthquake, followed by a more scattered $\Delta\sigma$ increase in the years following this event.

Laboratory experiments provide an insight into the physical evolution of fault strength during the earthquake cycle. Existing work has shown that the static coefficient of friction increases logarithmically with time of stationary contact and effective normal stress. Frictional healing is the mechanism that has been associated with fault re-strengthening following earthquake failure [e.g. Marone, 1998]. Recent experiments have shown that increased healing generates large amounts of high-frequency radiation, as displayed in figure 3.4 and 3.5, possibly explained by an increase in the heterogeneity of the spatially distributed points of contact along the plate interface, encouraging perturbations in slip velocity or rupture propagation [McLaskey et al., 2012]. At the macroscale, fault healing has been related to a combination of processes that include fracture closure, sealing, precipitation and pressure solution, but the mechanism responsible for re-strengthening is not well understood [Scholz, 1986; Scuderi et al., 2014].

Furthermore, laboratory analysis has shown that ageing at the nanoscale is much larger than at the macroscale, suggesting that frictional strengthening may be length-scale dependent. At the nanometer scale and at relatively low contact stresses, frictional ageing cannot be explained by increases in area of contact, rather, it has been proposed that the formation and/or strengthening of interfacial chemical bounds is the mechanism responsible for such re-strengthening [Li et al., 2011]. The time-dependent re-strengthening of the unstable fault patches observed in Figure 3.3 suggests that the plate interface heals within ~1.5 years after the 5 September 2012, Nicoya Peninsula earthquake, a time scale that is consistent with previous observations of hydrologic property and seismic velocity changes in postseismic fault zones [e.g. Xue et al., 2013; Brenguier et al., 2008].

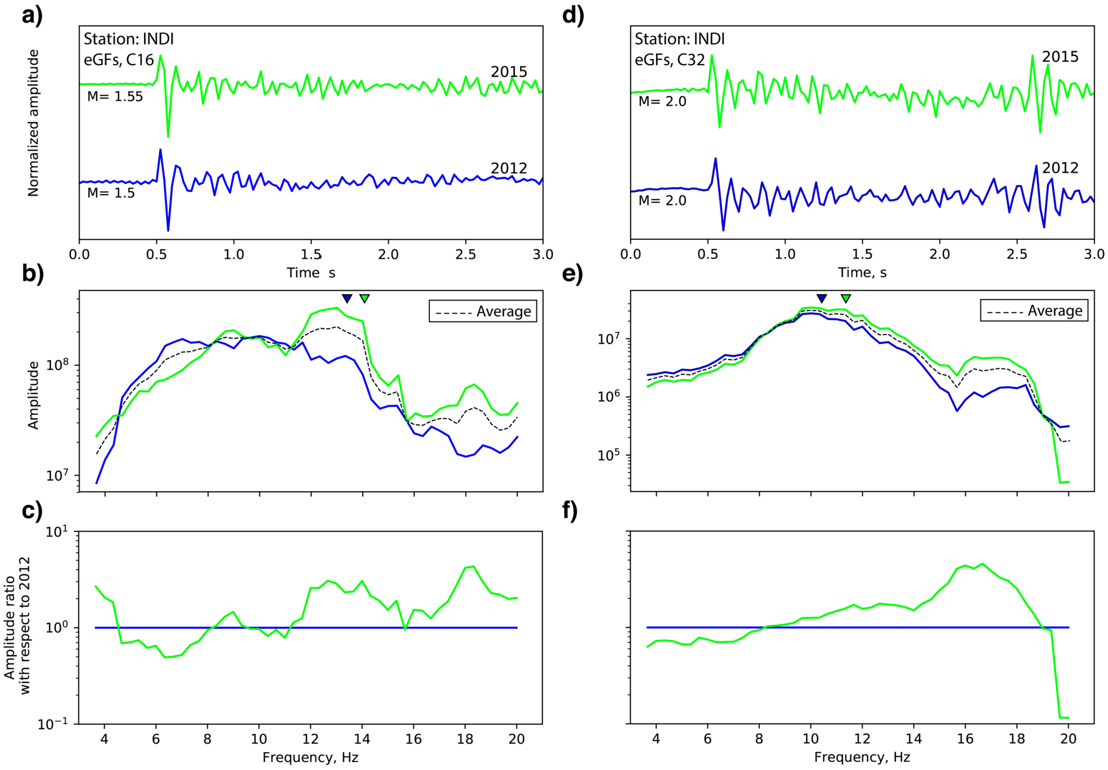

Figure 3.5. Time-frequency comparison of the raw seismograms (P-wave), between EGFs for clusters C16 and C32 recorded at station INDI. Panels (a) and (d) show the mainshock-affected EGF (color blue) and the healed EGF that occurred in 2015 (color green). The spectra for both, the affected and healed events are displayed in panels (b) and (e), color coded the same as the superior panel. The black dashed line corresponds with the average spectrum. Bottom panels (c) and (f) show the amplitude ratio for each event with respect to the mainshock-affected event. Note that healed-repeating event in 2015 presents more power at higher frequencies (9-18 Hz) with respect to the mainshock-affected EGF in 2012.

APPENDICES

APPENDIX A – SUPPLEMENTAL INFORMATION FOR CHAPTER 1

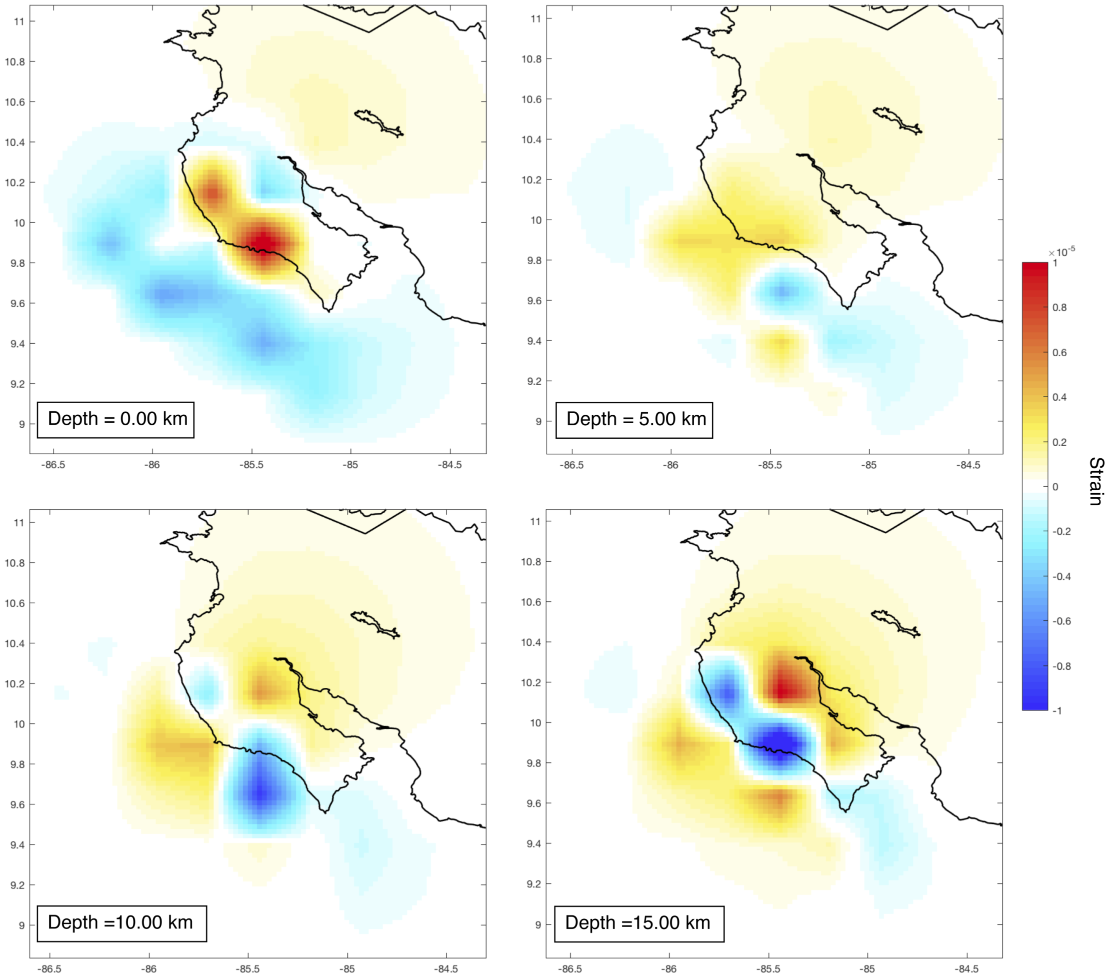

Figure. A-1. Volumetric strain changes generated by the Mw 7.6 2012 Nicoya Peninsula earthquake at depths of **A**) 0 km, **B**) 5 km, **C**) 10 km and **D**) 15 km calculated using the finite fault model provided by the USGS (http://comcat.cr.usgs.gov/earthquakes/eventpage/pde20120905144207800_35#summary) and Coulomb 3 software (*31*). Green triangles locate the seismic stations LAFE, INDI and SAJU.

APPENDIX B – SUPPLEMENTAL INFORMATION FOR CHAPTER 2

Figure B-1. Figure showing the Gutenberg-Richter distribution computed using the maximum likelihood method for: (a) and (b) the aftershock sequence during the four months subsequent to the main event and: (c) and (d) the first nine days of the earthquake sequence. The magnitude of completeness shown in panels (a) and (c) was generated using a Kolmogorov-Smirnov inversion approach.

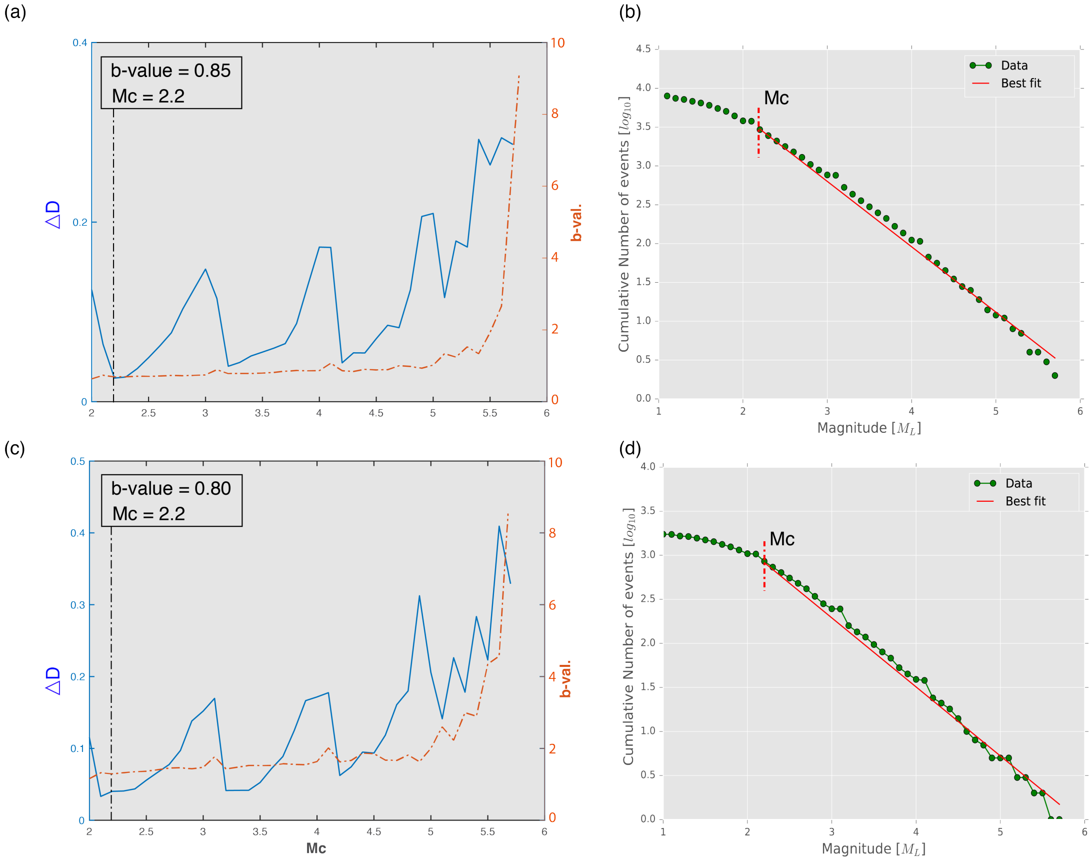
(a)
b-value = 0.85
Mc = 2.2
△D
b-val.
(b)
Mc
Data
Best fit
Cumulative Number of events [log_{10}]
Magnitude [M_L]
(c)
b-value = 0.80
Mc = 2.2
△D
b-val.
Mc
(d)
Mc
Data
Best fit
Cumulative Number of events [log_{10}]
Magnitude [M_L]

Figure B-2. Regional moment tensor inversion for a M_w 4 event performed using the local and regional seismic network. The figure shows the waveform fit between data (black lines) and synthetics (red lines), the moment tensor decomposition and source parameters. The Variance reduction as a function of depth is presented as well. Focal mechanisms are color coded by CLVD (%).

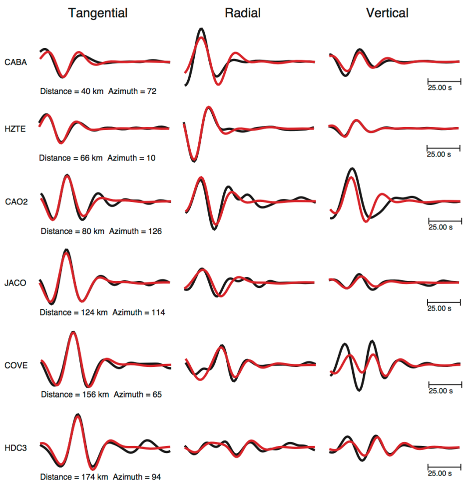

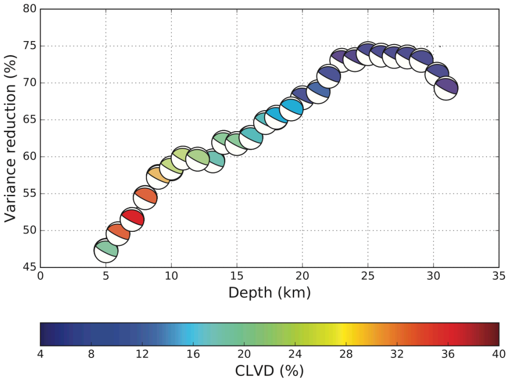

Best solution

EVID = 246
Centriod Depth = 25 km
Strike = 117 ; 276
Rake = 97 ; 69
Dip = 73 ; 18
Mo = 1.10e+22
Mw = 3.96
Percent DC = 94
Percent CLVD = 6
Percent ISO = 0
Variance = 1.29e−10
Var. Red. = 73.8
RES/Pdc = 1.37e−12

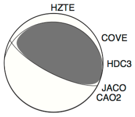

Figure B-3. Earthquake relocation. Relative hypocenter location of the aftershock sequence of the Nicoya Peninsula earthquake computed using GrowClust (a) and HypoDD (b). (c) Close-up window comparing the clustering of events between GrowClust (top panel) and HypoDD (bottom panel). The relative location errors from GrowClust are on the order of hundreds of meters.

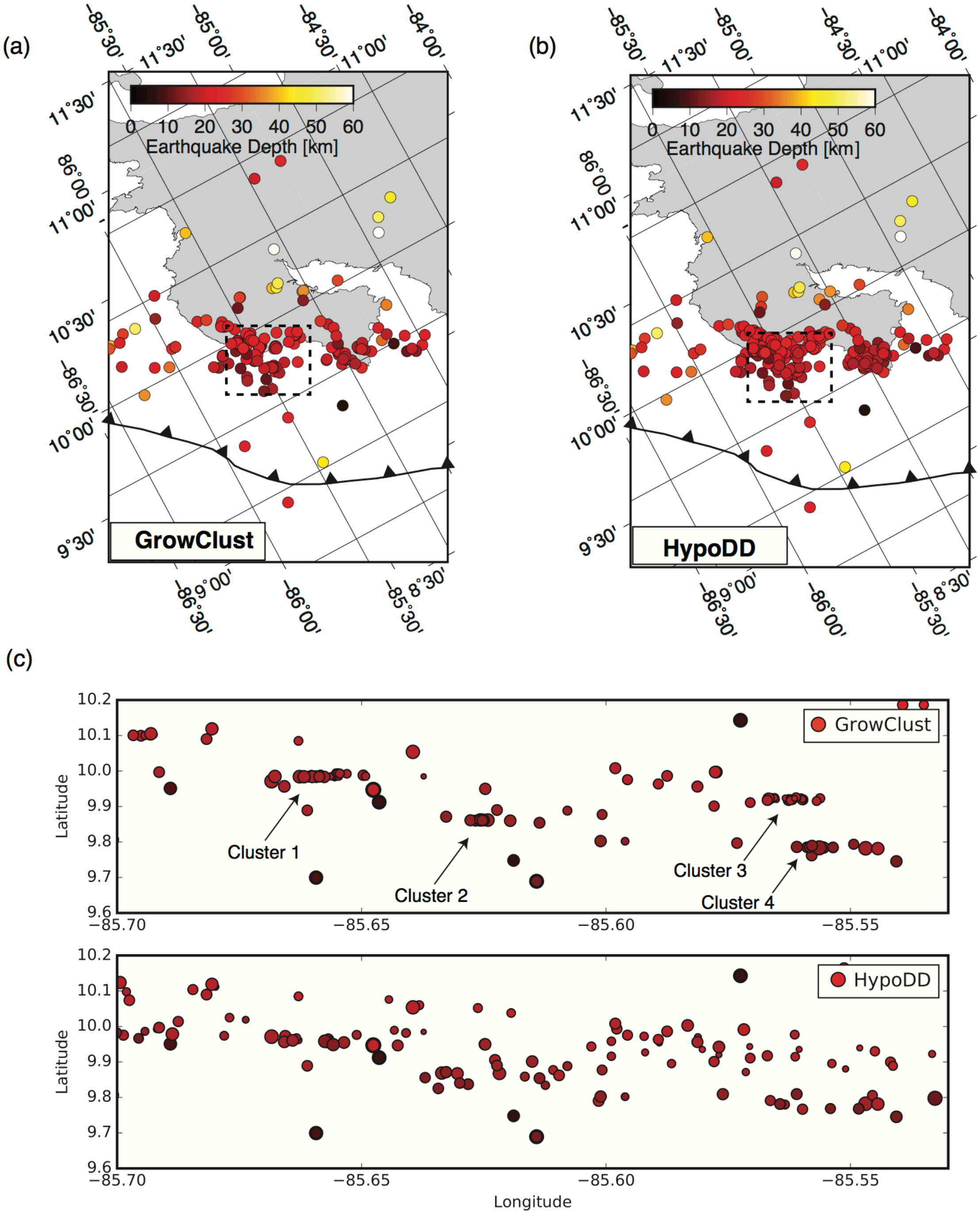
(a)
(b)
0 10 20 30 40 50 60
Earthquake Depth [km]
GrowClust
HypoDD
-85°30'
-85°00'
-84°30'
-84°00'
11°30'
11°00'
10°30'
10°00'
9°30'
-86°00'
-86°30'
-85°30'
9°00'
8°30'
(c)
Latitude
Longitude
10.2
10.1
10.0
9.9
9.8
9.7
9.6
−85.70
−85.65
−85.60
−85.55
GrowClust
HypoDD
Cluster 1
Cluster 2
Cluster 3
Cluster 4

Figure B-4. (a) Spatial distribution of in-slab seismicity that is well recorded by the local and regional seismic networks in the same area offshore the Nicoya Peninsula since 1999. Circles are color coded by year. (b) and (c) Cross-sections through seismic clusters OC1 and OC2. Cluster OC2 corresponds with cluster C3 in figure 4.

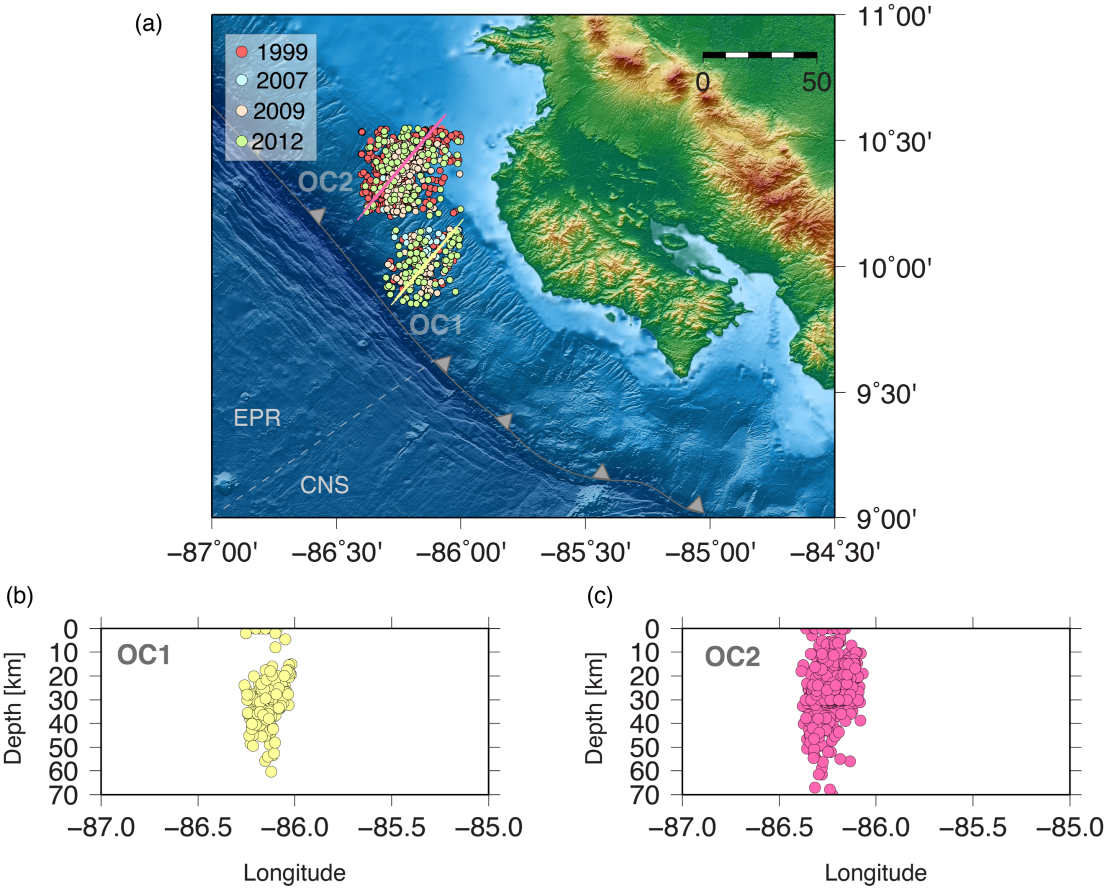
(a)
1999
2007
2009
2012
0
50
OC2
OC1
EPR
CNS
11˚00'
10˚30'
10˚00'
9˚30'
9˚00'
–87˚00'
–86˚30'
–86˚00'
–85˚30'
–85˚00'
–84˚30'
(b)
OC1
Depth [km]
0
10
20
30
40
50
60
70
–87.0
–86.5
–86.0
–85.5
–85.0
Longitude
(c)
OC2
Depth [km]
0
10
20
30
40
50
60
70
–87.0
–86.5
–86.0
–85.5
–85.0
Longitude

Table B-1. Earthquake relocations and focal geometries. Hypocenter locations and focal mechanisms for all of events analyzed in this study. Relative error estimates equal to -1 correspond with those events that were not relocated by the GrowClust algorithm.

APPENDIX C – SUPPLEMENTAL INFORMATION FOR CHAPTER 3

Figure C-1. Example of the deconvolution method for a M3.30 event in C60, that occurred on 5 September 2012 at 20:14:55.64 UTC time. Panel (a) Earthquake STF (thick black line) obtained after averaging the relative STFs computed at different stations using multiple EGFs. Each station is color coded by azimuth. (b) The mainshock source spectra (thick black line) is obtained by averaging the spectrum from all the individual stations. The red dashed line and star represents the initial fit to a Boatwright model and the corresponding initial corner frequency, f_{c1}. Panels (c) and (d) show the grid search around the resulting value of f_{c1}, to determine the range of f_{c1} and f_{c2} in which the fit between the data and the model given by the variance reduction (VR) is at least 85%. (e) Observed residual spectra computed by dividing the mainshock spectrum by the best-fit synthetic spectrum resulting from the gridsearch illustrated in panels (c) and (d).

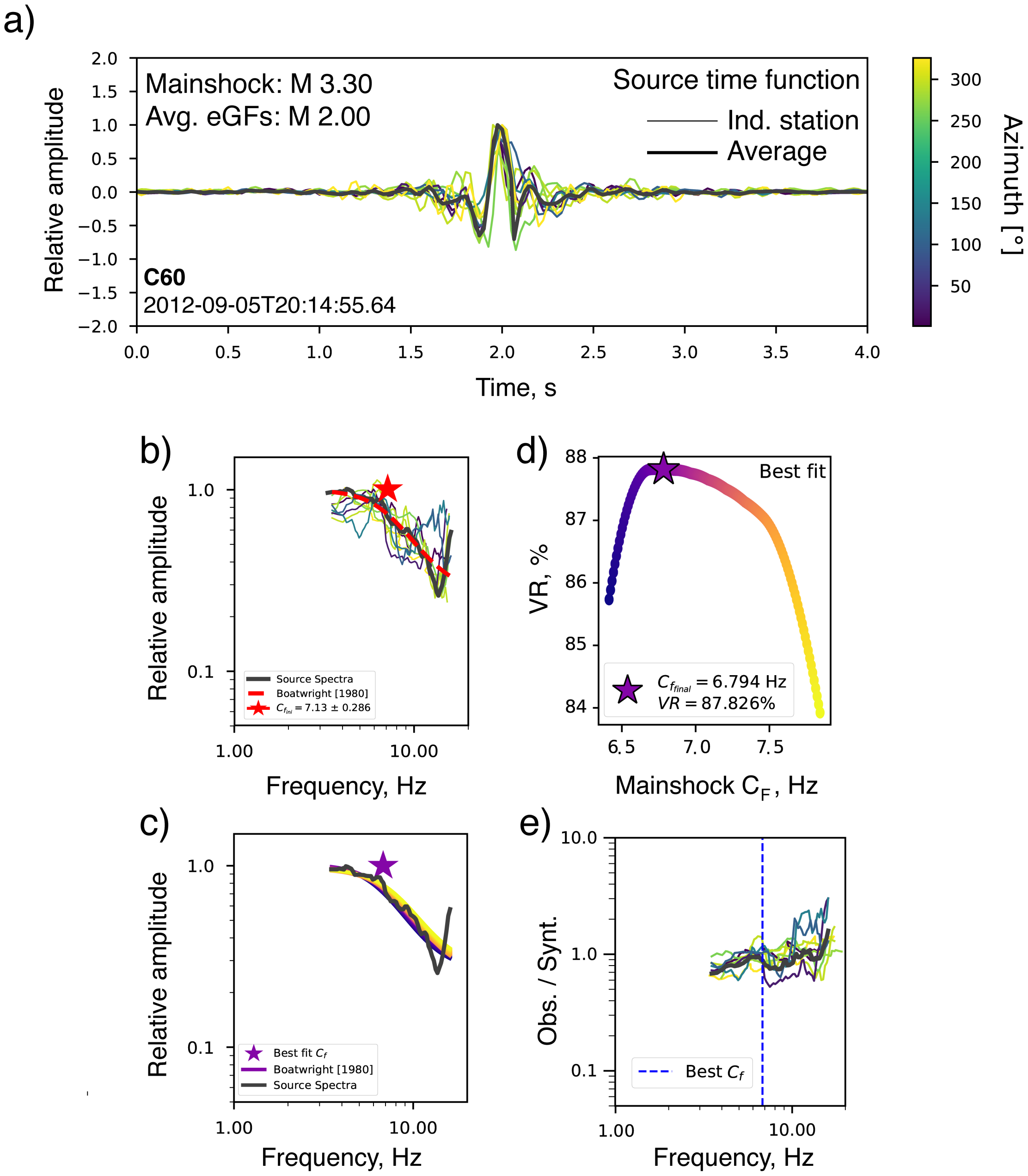
a)
Mainshock: M 3.30
Avg. eGFs: M 2.00
Source time function
Ind. station
Average
C60
2012-09-05T20:14:55.64
Relative amplitude
Time, s
Azimuth [°]
2.0
1.5
1.0
0.5
0.0
−0.5
−1.0
−1.5
−2.0
0.0
0.5
1.0
1.5
2.0
2.5
3.0
3.5
4.0
300
250
200
150
100
50
b)
Relative amplitude
Frequency, Hz
1.0
0.1
1.00
10.00
Source Spectra
Boatwright [1980]
$C_{f_{fin}} = 7.13 \pm 0.286$
c)
Relative amplitude
Frequency, Hz
1.0
0.1
1.00
10.00
Best fit C_f
Boatwright [1980]
Source Spectra
d)
VR, %
Mainshock C_F, Hz
Best fit
88
87
86
85
84
6.5
7.0
7.5
$C_{f_{final}} = 6.794$ Hz
$VR = 87.826\%$
e)
Obs. / Synt.
Frequency, Hz
10.0
1.0
0.1
1.00
10.00
Best C_f

Figure C-2. Time-frequency comparison of the raw seismograms (P-wave train), between target events for clusters C60, C32 and C16. Top panels show the vertical component of the mainshock-affected event (blue seismogram) directly after the occurrence of the 5 September 2012, M7.6 Nicoya earthquake and the pre-mainsshock or healed event (green seismogram) in a) 2011, (d) and (g) 2015. Middle panels: b), e) and h) show the seismic spectra for the mainshock-affected event and healed event. The black line indicates the average spectrum. Bottom panels: c), f) and i) display the ratio between the mainshock-affected event and pre-mainshock or healed event with respect to the average spectrum. Note the significant increase in high frequency radiation of the pre-earthquake and healed events in green with respect to the mainshock-affected event in blue at frequencies between 6 and 18 Hz.

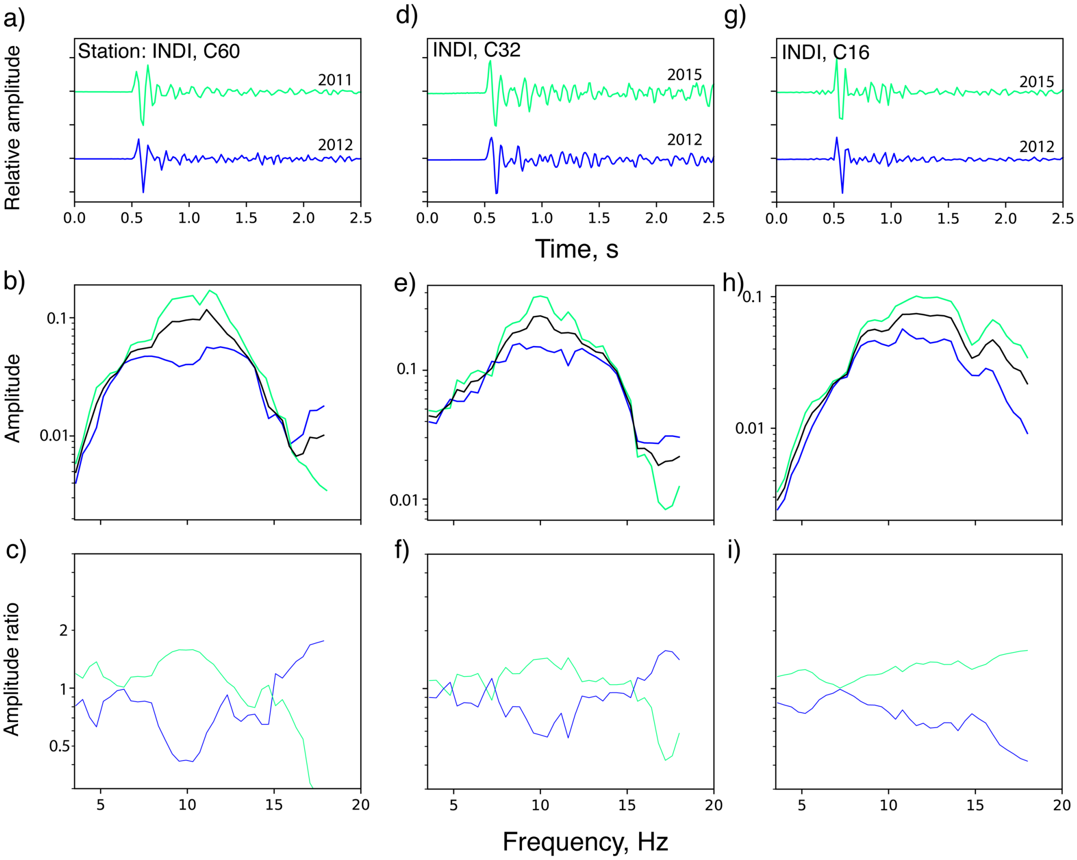
a)
Station: INDI, C60
2011
2012
d)
INDI, C32
2015
2012
g)
INDI, C16
2015
2012
Relative amplitude
0.0
0.5
1.0
1.5
2.0
2.5
Time, s
b)
e)
h)
Amplitude
0.1
0.01
c)
f)
i)
Amplitude ratio
2
1
0.5
5
10
15
20
Frequency, Hz

REFERENCES

Abercrombie, R. E. Comparison of direct and code wave stress drop measurements for the Wells, Nevada, earthquake sequence. *J. Geophys. Res.* **118**, 1458–1470 (2013).

Abercrombie, R. E. Stress drops of repeating earthquakes on the San Andreas Fault at Parkfield. *Geophys. Res. Lett.* **41**, 8784–8791 (2014).

Abercrombie, R. E. Investigating uncertainties in empirical Green's function analysis earthquake source parameters. *J. Geophys. Res.* **120**, 4263–4277 (2015).

Abercrombie, R. E., Bannister, S. C., Ristau, J., & Doser, D. Variability of earthquake stress drop in a subduction setting, the Hikurangi Margin, New Zealand. *Geophys. J. Int.* **208**(1), 306–320 (2017).

Allmann, B. & Shearer, P. Spatial and temporal stress drop variations in small earthquakes near Parkfield, California. *Journal of Geophysical Research: Solid Earth* **112,** (2007).

Asano, Y., T. Saito, Y. Ito, K. Shiomi, H. Hirose, T. Matsumoto, S. Aoi, S. Hori, and S. Sekiguchi (2011), Spatial distribution and focal mechanisms of aftershocks of the 2011 off the Pacific coast of Tohoku Earthquake, *Earth Planets Space*, *63*(7), 669–673, doi:10.5047/eps.2011.06.016.

Audet, P., & Schwartz, S. Y. (2013). Hydrologic control of forearc strength and seismicity in the Costa Rican subduction zone. *Nature Geoscience*, 6(10), 852–855, doi:10.1038/ngeo1927

Barckhausen, U., Ranero, C. R., von Huene, R., Cande, S. C. and Roeser, H. A. Revised tectonic boundaries in the Cocos Plate off Costa Rica: Implications for the segmentation of the convergent margin and for plate tectonic models. J. Geophys. Res. 106, 19207–19220. (2001).

Beroza, G. C., and S. Ide (2011), Slow earthquakes and nonvolcanic tremor, Annu. Rev. Earth Planet. Sci., 39, 271–296, doi:10.1146/ annurev-earth-040809-152531.

Beyreuther, M., R. Barsch, L. Krischer, T. Megies, Y. Behr, and J. Wassermann (2010), ObsPy: A Python Toolbox for Seismology, *Seismological Research Letters*, *81*(3), 530–533, doi:10.1785/gssrl.81.3.530.

Boatwright, J. A spectral theory for circular seismic sources: simple estimates of source dimension, dynamic stress drop and radiated seismic energy. *Bull. Seism. Soc. Am*. **70**, 1-28 (1980).

Brenguier *et al.* Mapping pressurized volcanic fluids from induced crustal seismic velocity drops. *Science* **345,** 80–82 (2014).

Brenguier *et al.* Postseismic Relaxation Along the San Andreas Fault at Parkfield from Continuous Seismological Observations.*Science* **321,** 1478–1481 (2008).

Brown, J. R., G. C. Beroza, S. Ide, K. Ohta, D. R. Shelly, S. Y. Schwartz, W. Rabbel, M. Thorwart, and H. Kao (2009), Deep low-frequency earthquakes in tremor localize to the plate interface in multiple subduction zones, *Geophysical Research Letters*, *36*(19), L19306, doi:10.1029/2009GL040027.

Brune, J. Tectonic stress and the spectra of seismic shear waves from earthquakes. *J. Geophys. Res*. **75**, 4997-5009 (1970).

Campillo, M. Phase and Correlation in `Random' Seismic Fields and the Reconstruction of the Green Function. *Pure and Applied Geophysics* **163,** 475–502 (2006).

Chaves, E. & Schwartz, S. Monitoring transient changes within overpressured regions of subduction zones using ambient seismic noise. *Science Advances* **2,** e1501289 (2016).

Chaves, E., Duboeuf, L., Schwartz, S., Lay, T. and Kintner, J. Aftershocks of the 2012 Mw 7.6 Nicoya, Costa Rica, Earthquake and Mechanics of the Plate InterfaceAftershocks of the 2012 Mw 7.6 Nicoya, Costa Rica, Earthquake and Mechanics of the Plate Interface. *Bulletin of the Seismological Society of America* **107,** 1227–1239 (2017).

Chamberlain, C. J., Hopp, C. J., Boese, C. M., Warren-Smith, E. Chambers, D., Chu, S. X., Michailos, K., Townend, J. EQcorrscan: Repeating and Near-Repeating

Earthquake Detection and Analysis in Python. ***Seism. Res. Lett.*** **89** (1), 173–181 (2017).

Cheng, X., Niu, F. & Wang, B. Coseismic Velocity Change in the Rupture Zone of the 2008 Mw 7.9 Wenchuan Earthquake Observed from Ambient Seismic Noise Coseismic Velocity Change in the Rupture Zone of the 2008 Mw 7.9 Wenchuan Earthquake. *Bull. Seismo.l Soc. Am.* **100,** 2539–2550 (2010).

Choy, G. L., and S. H. Kirby (2004), Apparent stress, fault maturity and seismic hazard for normal-fault earthquakes at subduction zones, *Geophysical Journal International*, doi:10.1111/j.1365-246X.2004.02449.

Clarke, D, Zaccarelli, L, Shapiro, NM & Brenguier, F. Assessment of resolution and accuracy of the Moving Window Cross Spectral technique for monitoring crustal temporal variations using ambient seismic noise. *Geophysical Journal International* **186,** 867–882.

DeMets. C., Gordon. R. G., Argus. D. F. Geologically current plate motions. *Geophys. J. Int.* 181, 1–80 (2010).

DeShon, H. R., S. Y. Schwartz, A. V. Newman, V. Gonzalez, M. Protti, L. M. Dorman, T. H. Dixon, D. E. Sampson, and E. R. Flueh (2006), Seismogenic zone structure beneath the Nicoya Peninsula, Costa Rica, from three-dimensional local earthquake P- and S-wave tomography, *Geophysical Journal International*, *164*(1), 109–124, doi:10.1111/j.1365-246X.2005.02809.

Di Toro, G., Han, R., Hirose, T., De Paola, N., Nielsen, S., Mizoguchi, K., Ferri, F., Cocco, M., and Shimamoto, T. Fault lubrication during earthquakes. *Nature* **471,**494 (2011).

Dixon, T. *et al.* Earthquake and tsunami forecasts: Relation of slow slip events to subsequent earthquake rupture. *Proc National Acad Sci* **111,** 17039–17044 (2014).

Dominguez, L., Taira, T. & Santoyo, M. Spatiotemporal variations of characteristic repeating earthquake sequences along the Middle America Trench in Mexico. *Journal of Geophysical Research: Solid Earth* **121,** 8855–8870 (2016).

Dreger, D. S., and D. V. Helmberger (1993), Determination of source parameters at regional distances with three-component sparse network data, *Journal of Geophysical Research: Solid Earth*, *98*(B5), 8107–8125, doi:10.1029/93JB00023.

Dreger, D., Nadeau, R. and Chung, A. Repeating earthquake finite source models: Strong asperities revealed on the San Andreas Fault. *Geophysical Research Letters* **34.** (2007).

Ekström, G., A. M. Dziewonski, and N. N. Maternovskaya (2005), Global seismicity of 2003: centroid–moment-tensor solutions for 1087 earthquakes, *Physics of the Earth and Planetary Interiors*, doi:10.1016/j.pepi.2004.09.006.

Eshelby, J. D. The determination of the elastic field on an ellipsoidal inclusion and related problems. *Proc. Roy. Soc. Lond., A*. 241, 376-396. (1957).

Edwards, J., Kluesner, J. W., Silver, E. A., Brodsky, E. E., Brothers, D. S., Bangs, N. L., Kirkpatrick, J. D., Wood, R. and Okamoto, K. Corrugated megathrust revealed offshore from Costa Rica. *Nat. Geosci.* 1–6 (2018). doi:10.1038/s41561-018-0061-4

Evans, J. R., D. Eberhart-Phillips, and C. H. Thurber (1994), User's manual for SIMULPS12 for imaging Vp and Vp/Vs: a derivative of the Thurber tomographic inversion SIMUL3 for local earthquakes and explosions. U. S. Geol. Surv. Open-File Report 94-431, U. S. Government Printing Office.

Fagereng, A., and R. H. Sibson (2010), Melange rheology and seismic style, *Geology*, *38*(8), 751–754, doi:10.1130/G30868.1.

Feng, L., A. V. Newman, M. Protti, V. Gonzalez, Y. Jiang, and T. H. Dixon (2012), Active deformation near the Nicoya Peninsula, northwestern Costa Rica, between 1996 and 2010: Interseismic megathrust coupling, *Journal of Geophysical Research: Solid Earth*, *117*(B6), doi:10.1029/2012JB009230.

Fulton *et al.* Low Coseismic Friction on the Tohoku-Oki Fault Determined from Temperature Measurements. *Science* **342,** 1214–1217 (2013).

Hansen, S. E. (2006), Earthquake relocation and focal mechanism determination using waveform cross correlation, Nicoya Peninsula, Costa Rica, *Bulletin of the Seismological Society of America*, *96*(3), 1003–1011, doi:10.1785/0120050129.

Hardebeck, J. L., J. J. Nazareth, and E. Hauksson (1998), The static stress change triggering model: Constraints from two southern California aftershock sequences, *Journal of Geophysical Research: Solid Earth*, *103*(B10), 24427–24437, doi:10.1029/98JB00573.

Hardebeck, J. L., and P. M. Shearer (2002), A new method for determining first-motion focal mechanisms, *Bulletin of the Seismological Society of America,* doi:10.1785/0120010200.

Harris, R. A., and R. W. Simpson (1996). In the shadow of 1857 - the effect of the Great Ft. Tejon Earthquake on subsequent earthquakes in southern California, *Geophysical Research Letters, 23*(3), 229-232, doi: 10.1029/96GL0015.

Hatakeyama, N., Uchida, N., Matsuzawa, T. & Nakamura, W. Emergence and disappearance of interplate repeating earthquakes following the 2011 M9.0 Tohoku-oki earthquake: Slip behavior transition between seismic and aseismic depending on the loading rate. *Journal of Geophysical Research: Solid Earth* **122,** 5160–5180 (2017).

Hobbs, Kyriakopoulos, Newman, Protti & Yao. Large and primarily updip afterslip following the 2012 Mw 7.6 Nicoya, Costa Rica, earthquake. *J Geophys. Res. Solid Earth.* **122,** 5712–5728 (2017).

Hobiger, M., U. Wegler, K. Shiomi, and H. Nakahara (2012), Coseismic and postseismic elastic wave velocity variations caused by the 2008 Iwate-Miyagi Nairiku earthquake, Japan, J. Geophys. Res., 117, B09313, doi:10.1029/2012JB009402.

Hsu, Y. J., M. Simons, J. P. Avouac, and J. Galetzka (2006), Frictional afterslip following the 2005 Nias-Simeulue earthquake, Sumatra, *Science*, 312, 1921, doi:10.1126/science.1126960.

Igarashi, T., Matsuzawa, T. & Hasegawa, A. Repeating earthquakes and interplate aseismic slip in the northeastern Japan subduction zone. *Journal of Geophysical Research: Solid Earth (1978–2012)* **108,** (2003).

Ito, Y., H. Matsubayashi, H. Kimura, T. Matsumoto, Y. Asano, and S. Sekiguchi (2004), Spatial distribution for moment tensor solutions of the 2003 Tokachi-oki earthquake (MJMA = 8.0) and aftershocks, *Earth Planets Space*, *56*(3), 301–306, doi:10.1186/BF03353055.

Jost, M. L., and R. B. Herrmann (1989), A student's guide to and review of moment tensors, *Seismological Research Letters*, *60*(2), 37–57, doi:10.1785/gssrl.60.2.37.

Kilb, D., and J. L. Hardebeck (2006), Fault parameter constraints using relocated earthquakes: A validation of first-motion focal-mechanism data, *Bulletin of the Seismological Society of America*, *96*(3), 1140–1158, doi:10.1785/0120040239.

Kimura, H., Kasahara, K., Igarashi, T. and Hirata, N. Repeating earthquake activities associated with the Philippine Sea plate subduction in the Kanto district, central Japan: A new plate configuration revealed by interplate aseismic slips. *Tectonophysics*. **417**, 101-118. 2006.

King, G. C. P., R. S. Stein, and J. LIN (1994), Static stress changes and the triggering of earthquakes, *Bulletin of the Seismological Society of America*, *84*(3), 935–953.

Kodaira, S. *et al.* High Pore Fluid Pressure May Cause Silent Slip in the Nankai Trough. *Science* **304,** 1295–1298 (2004).

Kyriakopoulos, C. A.V. Newman, A.M. Thomas, M. Moore-Driskell, and G.T. Farmer (2015), A new seismically constrained subduction interface model for Central America, J. *Geophys. Res.*, 120, doi:10.1002/2014JB011859.

Langseth, M. G., and E. A. Silver (1996), The Nicoya convergent margin - A region of exceptionally low heat flow, *Geophys. Res. Lett.*, *23*(8), 891–894.

Lay, T., Kanamori, H., Ammon, C. J., Koper, K. D., Hutko, A. R., Ye, L., Yue, H. and Rushing, T. M. Depth-varying rupture properties of subduction zone megathrust faults. *J. Geophys. Res. Solid. Earth. 2012.* **117.** (2012).

Lecocq, T., C. Caudron, and F. Brenguier (2014), MSNoise: a Python package for monitoring seismic velocity changes using ambient seismic noise, Seismol. Res. Lett., 85(3), 715–726, doi:10.1785/0220130073.

Li, Q., Tullis, T., Goldsby, D. & Carpick, R. Frictional ageing from interfacial bonding and the origins of rate and state friction. *Nature* **480,** 233 (2011).

Lui, S. and Lapusta, N. Repeating microearthquake sequences interact predominantly through postseismic slip. *Nature Communications* **7,** ncomms 13020 (2016).

Liu, C., Y. Zheng, X. Xiong, R. Wang, A. López, and J. Li (2015), Rupture processes of the 2012 September 5 M_W7.6 Nicoya, Costa Rica earthquake constrained by improved geodetic and seismological observations, *Geophysical Journal International, 203*(1), 175–183. http://doi.org/10.1093/gji/ggv295.

Liu, Z., Huang, J., Peng, Z. & Su, J. Seismic velocity changes in the epicentral region of the 2008 Wenchuan earthquake measured from three-component ambient noise correlation techniques.*Geophysical Research Letters* **41,** 37–42 (2014).

Madariaga, R. Dynamics of an Expanding Circular Fault. *Bull. Seis. Soc. Am.*, 66. 639-666. (1976).

Marone, C., Vidale, J. E. and Ellsworth, W. L. Fault healing inferred from time dependent variations in source properties of repeating earthquakes. *Geophys. Res. Let.* **22,** 3095–3098. (1995).

Marone, C. The effect of loading rate on static friction and the rate of fault healing during the earthquake cycle. *Nature.,* **391,** (1998).

Marone, C. and Saffer, D. M. The Mechanics of Frictional Healing and Slip Instability During the Seismic Cycle. *Treatise on Geophysics*., 111-138 (2015)

Malservisi, R., Schwartz, S. Y., Voss, N., Protti, M., Gonzales, V., Dixon, T. H., Jiang, Y., Newman, A., Richardson, J., Walter, J. I. and Voyenko, D. Multiscale postseismic behavior on a megathrust: The 2012 Nicoya earthquake, Costa Rica.*Geochemistry, Geophysics, Geosystems* **16,** 1848–1864 (2015).

McLaskey, G., Thomas, A., Glaser, S. and Nadeau, R. Fault healing promotes high-frequency earthquakes in laboratory experiments and on natural faults. *Nature* **491,** 101 (2012).

Minson, S. E., and D. S. Dreger (2008), Stable inversions for complete moment tensors, *Geophysical Journal International*, *174*(2), 585-592, doi:10.1111/j.1365-246X.2008.03797

Minato, S., T. Tsuji, S. Ohmi, and T. Matsuoka (2012), Monitoring seismic velocity change caused by the 2011 Tohoku-oki earthquake using ambient noise records, *Geophys. Res. Lett.*, 39, L09309, doi:10.1029/ 2012GL051405.

Nadeau, R. M. and Johnson, L. R. Seismological Studies at Parkfield VI: Moment Release Rates and Estimates of Source Parameters for Small Repeating Earthquakes. *Bulletin of the Seismological Society of America* **88,** 790–814 (1998).

Nakata, Snieder & Behm. Body-wave interferometry using regional earthquakes with multidimensional deconvolution after wavefield decomposition at free surface. *Geophysical Journal International* **199,** 1125–1137 (2014).

Pacheco, J. F., and S. K. Singh (2010), Seismicity and state of stress in Guerrero segment of the Mexican subduction zone, *J. Geophys. Res.*, *115*(B1), B01303–14, doi:10.1029/2009JB006453.

Peng, Z., Vidale, J., Marone, C. and Rubin, A. Systematic variations in recurrence interval and moment of repeating aftershocks. *Geophys. Res. Lett.,* **32,** (2005).

Peng, Z. & Ben-Zion, Y. Temporal Changes of Shallow Seismic Velocity Around the Karadere-Düzce Branch of the North Anatolian Fault and Strong Ground Motion. *pure and applied geophysics* **163,** 567–600.

Prieto, G. A., Parker, R.L. and Vernon. F. L. A Fortran 90 library for multitaper spectrum analysis. *Computers & Geosciences* **35***, 1701-1710.* (2009).

Protti, M. *et al.* Nicoya earthquake rupture anticipated by geodetic measurement of the locked plate interface. *Nature Geoscience* **7,**117–121 (2013).

Poupinet, Ellsworth & Frechet. Monitoring velocity variations in the crust using earthquake doublets: An application to the Calaveras Fault, California. *Journal of Geophysical Research: Solid Earth (1978–2012)* **89,** 5719–5731 (1984).

Raehaee, H., Shimamoto, T., Hirose, T., Ree, J., Ando, J. Utralow Friction of Carbonate Faults Caused by Thermal Decomposition. *Science* **316**, 878-881 (2007)

Rice, J. R. Heating and weakening of faults during earthquake slip. *Journal of Geophysical Research: Solid Earth* **111,** (2006).

Rietbrock, A., I. Ryder, G. Hayes, C. Haberland, D. Comte, S. Roecker, and H. Lyon-Caen (2012), Aftershock seismicity of the 2010 Maule M_W=8.8, Chile, earthquake:

Correlation between co-seismic slip models and aftershock distribution? *Geophysical Research Letters*, *39*(8), doi:10.1029/2012GL051308.

Rivet, D. *et al.* Seismic evidence of nonlinear crustal deformation during a large slow slip event in Mexico. *Geophysical Research Letters***38,** (2011).

Rivet, D. *et al.* Seismic velocity changes, strain rate and non-volcanic tremors during the 2009–2010 slow slip event in Guerrero, Mexico. *Geophysical Journal International* **196,** 447–460 (2014).

Rubinstein, J. & Ellsworth, W. Precise Estimation of Repeating Earthquake Moment: Example from Parkfield, California. *Bulletin of the Seism. Soc. Am.* **100,** 1952–1961 (2010).

Saffer, D. & Wallace, L. The frictional, hydrologic, metamorphic and thermal habitat of shallow slow earthquakes. *Nature Geoscience***8,** 594–600 (2015).

Saikia, C. K. (1994), Modified frequency-wavenumber algorithm for regional seismograms using Filon's quadrature: modelling of Lg waves in eastern North America, *Geophysical Journal International*, *118*(1), 142–158, doi:10.1111/j.1365-246X.1994.tb04680.

Sato, T., S. Hiratsuka, and J. Mori (2013), Coulomb stress change for the normal-fault aftershocks triggered near the Japan Trench by the 2011 M_W 9.0 Tohoku-Oki earthquake, *Earth Planets Space*, *64*(12), 1239–1243, doi:10.5047/eps.2012.04.003.

Scuderi, M., Carpenter, B. & Marone, C. Physicochemical processes of frictional healing: Effects of water on stick-slip stress drop and friction of granular fault gouge. *J. Geophys. Res. Solid Earth* **119,** 4090–4105 (2014).

Scholz, C. H., Aviles, CA & Wesnousky, S. G. Scaling differences between large interplate and intraplate earthquakes. *Bulletin of the Seis. Soc. Am.* **76,** 65–70 (1986).

Scholz, C. (2002). The Mechanics of Earthquakes and Faulting, Cambridge University Press, Cambridge, United Kingdom, 471 pp.

Schwartz, S. and Rokosky, J. Slow slip events and seismic tremor at circum Pacific subduction zones. *Reviews of Geophysics* **45.** (2007).

Shapiro & Campillo. Emergence of broadband Rayleigh waves from correlations of the ambient seismic noise. *Geophysical Research Letters* **31.** (2004).

Stein, R. S. (1999), The role of stress transfer in earthquake occurrence, *Nature*, doi:10.1038/45144.

Sumy, D. F., E. S. Cochran, and K. M. Keranen (2014), Observations of static Coulomb stress triggering of the November 2011 *M*5.7 Oklahoma earthquake sequence, *Journal of Geophysical Research*, doi:10.1002/(ISSN)2169-9356.

Toda, S., J. LIN, and R. S. Stein (2011a), Using the 2011 M_W 9.0 off the Pacific coast of Tohoku Earthquake to test the Coulomb stress triggering hypothesis and to calculate faults brought closer to failure, *Earth Planets Space*, *63*(7), 725–730, doi:10.5047/eps.2011.05.010.

Toda, S., R. S. Stein, and J. LIN (2011b), Widespread seismicity excitation throughout central Japan following the 2011 *M*=9.0 Tohoku earthquake and its interpretation by Coulomb stress transfer, *Geophysical Research Letters*, *38*(7), doi:10.1029/2011GL047834.

Toda, S., R. S. Stein, J. Lin, and V. Sevilgen., *U.S. Geol. Surv. Open-File Rep.*, (2011c).

Trugman, D. T., and P. M. Shearer (2017), GrowClust: A hierarchical clustering algorithm for relative earthquake relocation, with application to the Spanish Springs and Sheldon, Nevada, earthquake sequences, *Seismological Research Letters, 88*(2), doi: 10.1785/0220160188.

Uchida, N, Matsuzawa, T., Ellsworth, W. L., Imanishi, K., Okada, T. and Hasegawa, A. Source parameters of a M4.8 and its accompanying repeating earthquakes off Kamaishi, NE Japan: Implications for the hierarchical structure of asperities and earthquake cycle. *Geophysical research letters* **34,** (2007).

Uchida, N., Matsuzawa, T., Ellsworth, W. L., Imanishi, K., Shimamura, K., Hasegawa, A. Source parameters of microearthquakes on an interplate asperity off Kamaishi, NE Japan over two earthquake cycles. *Geophysical Journal International* **189,** 999–1014 (2012).

Uchida, N., Shimamura, K., Matsuzawa, T. & Okada, T. Postseismic response of repeating earthquakes around the 2011 Tohoku oki earthquake: Moment increases due to the fast loading rate. *Journal of Geophysical Research: Solid Earth* **120,** 259–274 (2015).

Vidale, J. E., Ellsworth, W. L. , Cole, A. and Marone, C. Variations in Rupture Process with Recurrence Interval in a Repeated Small Earthquake. *Nature* **368,**624–626.

Viesca, R. C. and Garagash D. I. Ubiquitous weakening of faults due to thermal pressurization. Nature Geoscience, **8**, 875-879 (2015).

Voss, N., Malservisi, R., Dixon, T. & Protti, M. Slow slip events in the early part of the earthquake cycle. *J Geophys Res Solid Earth* **122,** 6773–6786 (2017).

Walter, J., Schwartz, S., Protti, M. & Gonzalez, V. Persistent tremor within the northern Costa Rica seismogenic zone.*Geophysical Research Letters* **38.** (2011).

Walter, J. I., S. Y. Schwartz, M. Protti, and V. Gonzalez (2013), The synchronous occurrence of shallow tremor and very low frequency earthquakes offshore of the Nicoya Peninsula, Costa Rica, *Geophysical Research Letters, 40*(8), 1517–1522, doi:10.1002/grl.50213.

Walter, J. I., X. Meng, Z. Peng, S. Y. Schwartz, A. V. Newman, and M. Protti (2015), Far-field triggering of foreshocks near the nucleation zone of the 5 September 2012 (M_W 7.6) Nicoya Peninsula, Costa Rica earthquake, *Earth and Planetary Science Letters*, *431*(C), 75–86, doi:10.1016/j.epsl.2015.09.017.

Wang, K., and S. L. Bilek (2011), Do subducting seamounts generate or stop large earthquakes? *Geology*, *39*(9), 819–822, doi:10.1130/G31856.1.

Worzewski, T., Jegen, M., Kopp, H., Brasse, H. & Castillo, W. Magnetotelluric image of the fluid cycle in the Costa Rican subduction zone. *Nature Geoscience* **4,** 108–111 (2010).

Xue, L., S. Y. Schwartz, Z. Liu, and L. Feng (2015), Interseismic megathrust coupling beneath the Nicoya Peninsula, Costa Rica, from the joint inversion of InSAR and GPS data, *Journal of Geophysical Research: Solid Earth*, *120*(5), 3707–3722, doi:10.1002/2014JB011844.

Yao, D. *et al.* Detailed spatiotemporal evolution of microseismicity and repeating earthquakes following the 2012 Mw 7.6 Nicoya earthquake. *J Geophys Res Solid Earth* **122,** 524–542 (2017).

Yue, H., T. Lay, S. Y. Schwartz, L. Rivera, M. Protti, T. H. Dixon, S. Owen, and A. V. Newman (2013), The 5 September 2012 Nicoya, Costa Rica M_W 7.6 earthquake rupture process from joint inversion of high-rate GPS, strong-motion, and teleseismic P wave data and its relationship to adjacent plate boundary interface properties, *Journal of Geophysical Research: Solid Earth*, *118*(10), 5453–5466, doi:10.1002/jgrb.50379.

Zaccarelli, Shapiro, Faenza, Soldati & Michelini. Variations of crustal elastic properties during the 2009 L'Aquila earthquake inferred from cross-correlations of ambient seismic noise.*Geophysical Research Letters* **38,** (2011).

Zielke, O., Galis, M., Mai, P. M. Fault roughness and strength heterogeneity control earthquake size and stress drop. *Geophys. Res. Lett.*, **44**, 777-783 (2017).

Zhu, S., and M. Miao (2015), How Did the 2013 Lushan Earthquake (M_S = 7.0) Trigger its Aftershocks? Insights from Static Coulomb Stress Change Calculations, *Pure appl. geophys.*, *172*(10), 2481–2494, doi:10.1007/s00024-015-1064-3.